



저작자표시-비영리-변경금지 2.0 대한민국

이용자는 아래의 조건을 따르는 경우에 한하여 자유롭게

- 이 저작물을 복제, 배포, 전송, 전시, 공연 및 방송할 수 있습니다.

다음과 같은 조건을 따라야 합니다:



저작자표시. 귀하는 원저작자를 표시하여야 합니다.



비영리. 귀하는 이 저작물을 영리 목적으로 이용할 수 없습니다.



변경금지. 귀하는 이 저작물을 개작, 변형 또는 가공할 수 없습니다.

- 귀하는, 이 저작물의 재이용이나 배포의 경우, 이 저작물에 적용된 이용허락조건을 명확하게 나타내어야 합니다.
- 저작권자로부터 별도의 허가를 받으면 이러한 조건들은 적용되지 않습니다.

저작권법에 따른 이용자의 권리는 위의 내용에 의하여 영향을 받지 않습니다.

이것은 [이용허락규약\(Legal Code\)](#)을 이해하기 쉽게 요약한 것입니다.

[Disclaimer](#)

공학박사 학위논문

**Study on plasmonic nanoparticle array
fabrication for optical hydrogen
sensing**

광학적 수소 검출을 위한 플라즈모닉 나노 입자
배열 제작에 관한 연구

2022 년 8 월

서울대학교 대학원
재료공학부
김 태 룡

Study on plasmonic nanoparticle array fabrication for optical hydrogen sensing

지도교수 장 호 원

이 논문을 공학박사 학위논문으로 제출함

2022 년 7 월

서울대학교 대학원
재료공학부
김 태 룡

김태룡의 공학박사 학위논문을 인준함

2022 년 8 월

Chair 김 진 영 (Seal)

Vice Chair 장 호 원 (Seal)

Examiner 장 혜 진 (Seal)

Examiner 윤 의 준 (Seal)

Examiner 박 용 조 (Seal)

Abstract

Study on plasmonic nanoparticle array fabrication for optical hydrogen sensing

Taeryong Kim

Department of Materials and Science and Engineering

College of Engineering

Seoul National University

The need for carbon neutrality is growing in the face of the global crisis of climate change. Hydrogen is in the spotlight as a resource for realizing carbon neutrality. In addition, hydrogen has a high energy density, making it valuable as an energy resource. However, because hydrogen has a wide flammable range, low ignition energy and high flame speed, hydrogen leakage can lead to large-scale explosions. Therefore, it is essential to have a sensor that can quickly detect hydrogen leaks for commercialization of hydrogen.

Palladium is the most popular hydrogen sensing material due to its sensitivity and selectivity to hydrogen. However, palladium has

disadvantages in that the hydrogen measurement range is limited due to hysteresis, and mechanical stability is lowered due to embrittlement effect when the hydrogen content of palladium is increased. Various studies have been conducted to solve these shortcomings, and alloying with other metals is one of them.

Among the hydrogen measurement methods using palladium, two representative methods are an electrical measurement method and an optical measurement method. The electrical measurement method has the advantage of being easy to manufacture as a general measurement method but has disadvantages such as the effect of electromagnetic interference (EMI) and the potential for explosion due to sparks. On the other hand, the optical measurement method has advantages in that it is not affected by electromagnetic interference (EMI), there is no possibility of explosion in the measurement method. In addition, since it can operate as a sensor in a very small area, it is possible to make a sensor with a very small size.

The hydrogen sensor using localized surface plasmon resonance is a high-performance hydrogen sensor that has been in the spotlight for its high sensitivity and fast response time among optical hydrogen sensors. Using localized surface plasmon resonance requires fabricating nanoparticle arrays. Electron beam lithography and nanosphere lithography are used as methods for fabricating the array of nanoparticles. Electron beam lithography is a

manufacturing method that is difficult to apply due to high process cost and high process difficulty. Nanosphere lithography has been most used due to its low process cost and easy fabrication, but it has poor reproducibility and has limitations in producing patterned nanoparticle arrays.

In this study, a method of efficiently fabricating a nanoparticle array for a hydrogen sensor based on local surface plasmon resonance and the optical and hydrogen measurement characteristics of the nanoparticle array were studied. First, a method for fabricating nanoparticles with a hexagonal structure using nanoimprint lithography was demonstrated. It was shown that an array of 160 nm diameter nanoparticles with a 200 nm pitch hexagonal structure was effectively fabricated through an optimized process. To identify the palladium-gold composition suitable for a localized surface plasmon resonance-based hydrogen sensor using nanoimprint lithography, palladium-gold nanoparticle arrays of various compositions were fabricated, and their crystallographic properties and surface composition were analyzed. In the alloying process by heat treatment, it was observed that the surface composition of the palladium-gold nanoparticles was changed according to the heat treatment temperature, and it was found that the heat treatment temperature at 600 °C was the optimal annealing temperature.

However, nanoimprint lithography has two disadvantages: the need to change the nanoimprint mold to change the diameter or pattern of

nanoparticles, and the difficulty and cost of the manufacturing mold are greatly increased to produce nanoparticle arrays with the diameter of 100 nm or less. To overcome these disadvantages, nanotip indentation lithography has been proposed to fabricate nanoparticle arrays. Nanoparticle fabrication through nanotip indentation lithography has been used very limitedly, such as nanoparticle fabrication for SERS. However, since this study shows that nanoparticle arrays can be formed over a wide area with a width of 60 μm and a length of 60 μm , its application is expected to be diversified. In this study, three factors influencing the nano-particle diameter in the nano-tip indentation lithography process were investigated in detail. Considering these factors, it was shown that the diameter of nanoparticles was efficiently controlled from 56 nm to 132 nm by controlling the particles at intervals of several nanometers. In addition, the optimized process conditions for each particle size are included in the dissertation.

Finally, the optical properties and hydrogen measurement performance of palladium-gold nanoparticle arrays fabricated through nanoimprint lithography and nanotip indentation lithography were investigated. The shift of the local surface plasmon resonance peak of the palladium-gold nanoparticle array under various conditions was measured and the cause was explained. The hydrogen measurement characteristics of various palladium-gold compositions were analyzed, and the Pd₇Au₃ composition was confirmed to be the most suitable composition, and the cause of the

improvement of the hydrogen measurement characteristics when alloyed at 600° C was analyzed and described.

Through this study, it is expected that the nanoparticle manufacturing method using nanotip indentation lithography will be used in various fields. And also, it is expected that a better hydrogen sensor than the current hydrogen sensor will be developed through a method of improving the hydrogen measurement characteristics by controlling the surface composition of nanoparticles.

Kew Words:

Nanoimprint lithography, Nanotip indentation lithography,
Localized surface plasmon resonance-based hydrogen sensor,
Surface segregation effect, Palladium-gold (PdAu) alloy

Student Number: 2014-21490

Contents

| | |
|------------------------------|--------------|
| Abstract | i |
| Contents | vi |
| List of Figures | x |
| List of Tables | xviii |

Chapter 1. Plasmonic hydrogen sensor: Principle and major material.....1

| | |
|--|----|
| 1.1. Introduction | 1 |
| 1.2. History of LSPR based optical hydrogen sensor..... | 7 |
| 1.3. Principle of LSPR based optical hydrogen sensor | 9 |
| 1.4. Major materials for LSPR based optical hydrogen sensor..... | 12 |
| 1.5. Fabrication methods for LSPR based optical hydrogen sensor..... | 14 |
| 1.6. Purpose and organization of this thesis..... | 17 |
| 1.7. Bibliography..... | 19 |

Chapter 2. Fabrication of PdAu nanoparticle arrays using nanoimprint lithography.....27

| | |
|-----------------------------------|----|
| 2.1. Introduction..... | 27 |
| 2.2. Experimental procedures..... | 29 |

| | |
|---|----|
| 2.2.1. Nanoparticle array fabrication procedures using nanoimprint lithography | 29 |
| 2.2.2. Material characterization..... | 30 |
| 2.3. Results and discussions | 33 |
| 2.2.1. Fabrication results of PdAu NP arrays | 33 |
| 2.3.2. Characterization of PdAu Nanoparticle Arrays by Composition | 40 |
| 2.3.3. Characterization of Pd ₇ Au ₃ nanoparticle arrays according to various annealing temperatures..... | 44 |
| 2.4. Summary | 55 |
| 2.5. Bibliography..... | 56 |

Chapter 3. Study on the fabrication of plasmonic nanoparticle arrays using nanotip indentation lithography61

| | |
|---|----|
| 3.1. Introduction..... | 61 |
| 3.2. Experimental details..... | 63 |
| 3.2.1. Nanoparticle array fabrication process using nanotip indentation lithography | 63 |
| 3.2.2. Process optimization of nanoparticle fabrication using nanotip indentation lithography | 65 |
| 3.3. Results and discussions | 69 |
| 3.3.1. Control parameters and controlled results of each nano indentation lithography process | 69 |

| | |
|---|----|
| 3.3.2. Factors determining the diameter of nanoparticles in nanotip indentation lithography | 76 |
| 3.3.3. Fabrication results of nanoparticle arrays using nanotip indentation lithography | 86 |
| 3.4. Summary | 94 |
| 3.5 Bibliography..... | 95 |

Chapter 4. Study on optical hydrogen measurement of PdAu alloy nanoparticle arrays99

| | |
|---|-----|
| 4.1. Introduction..... | 99 |
| 4.2. Experimental details..... | 100 |
| 4.2.1. FDTD simulation of Pd nanodisk..... | 100 |
| 4.2.2. Evaluation of optical properties and hydrogen sensing properties of PdAu nanoparticle arrays..... | 103 |
| 4.3. Results and discussions | 106 |
| 4.3.1. Comparison of transmittance change between random and hexagonal structures..... | 106 |
| 4.3.2. FDTD simulation results of the LSPR peak shift for Pd nanoparticle arrays of various diameter | 109 |
| 4.3.3. The optical properties of nanoimprinted PdAu nanoparticle arrays | 111 |
| 4.3.4. The optical properties of PdAu nanoparticle arrays fabricated by nanotip indentation lithography | 121 |

| | |
|--|------------|
| 4.3.5. The evaluation of optical hydrogen sensing properties for various condition of PdAu nanoparticle array..... | 125 |
| 4.4. Summary | 139 |
| 4.5 Bibliography..... | 140 |
| Chapter 5. Conclusion..... | 144 |
| 국문 초록 | 147 |

List of Figures

| | |
|--|----|
| Figure 1.1 Schematic diagram of hydrogen production, storage, distribution, and use..... | 4 |
| Figure 1.2 Advantages of optical hydrogen sensors compared to electrical hydrogen sensors. | 6 |
| Figure 1.3 Measurement system and operation principle of LSPR-based hydrogen sensor, (a) LSPR-based sensor measurement system, (b) Pristine palladium nanoparticle, (c) Palladium nanoparticle with hydrogen, (d) Changes in the LSPR spectrum due to hydrogen absorption, (e) Measuring the time-dependent change of the LSPR spectrum. | 11 |
| Figure 2.1 Process flow of nanoimprint lithography..... | 31 |
| Figure 2.2 Annealing conditions for PdAu alloys, a) Schematic diagram of alloy formation through annealing of multi-layer thin film[12], b) Schematic diagram of annealing process..... | 32 |
| Figure 2.3 Thickness analysis result of two polymer layer fabricated by spin coating, a) 3D AFM image of the step height for two polymer layers, b) Height profiles for two polymer layers. | 35 |
| Figure 2.4 SEM image of nanoimprint mold a) top-view b) bird eye view.. | 36 |
| Figure 2.5 Depth profiles for nanoimprinted polymer surface a) 3D AFM image and b) depth profile result of patterned polymer layer after nanoimprint process. | 37 |

| | |
|---|----|
| Figure 2.6 Nanoparticle arrays fabricated by nanoimprint lithography, a) SEM images with magnification x50,000, b) SEM image with magnification x10,000..... | 38 |
| Figure 2.7 SEM images of various PdAu compositions annealed at 600 °C. | 42 |
| Figure 2.8 XRD results of various PdAu composition, a) 2theta results from 20° to 90°, b) 111 plane peaks of various PdAu composition, c) Table summarizing the measured 111 peak, the calculated 111 d-spacing and the calculated lattice parameter..... | 43 |
| Figure 2. 9 SEM and AFM images of annealed Pd7Au3 samples at various annealing temperatures..... | 46 |
| Figure 2.10 XRD results of various annealing temperature, a) 2theta results from 20° to 90°, b) XRD peaks of PdAu 111 plane, c) Rocking curve of PdAu 111 plane, d) FWHM of 2-theta and rocking curve of PdAu 111 plane | 47 |
| Figure 2.11 High-resolution XPS spectra for various annealing temperatures of PdAu nanoparticle arrays, a) Au 4f and b) Pd 3d spectra annealed at 400 °C, c) Au 4f and d) Pd 3d spectra annealed at 500 °C, e) Au 4f and f) Pd 3d spectra annealed at 600 °C and g) Au 4f and h) Pd 3d spectra annealed at 700 °C..... | 50 |
| Figure 2.12 TEM analysis of annealed Pd7Au3 samples, a) TEM images of annealed Pd7Au3 samples, b) high-resolution TEM image of annealed | |

| | |
|---|----|
| Pd7Au3 sample, c) SAED pattern of annealed Pd7Au3 sample, d) EDX annealed Pd7Au3 sample | 54 |
| Figure 3.1 Schematic diagram of indentation process | 67 |
| Figure 3.2 Process flow of nanotip indentation lithography | 68 |
| Figure 3.3 Polymer thickness measurement result according to spin coating material and RPM, a) PMGI SF3 for 1st polymer layer and b) MR-I 8010r and 8020r for 2nd polymer layer..... | 70 |
| Figure 3.4 AFM measurement results of etch depth, etch rate, and surface roughness according to etching time and RF power of reactive ion etching, a) Etch depth measurement results according to RF power and etching time, b) Surface roughness measurement results according to etch depth, c) 3D AFM images of the MR-I 8020r surface for various etch depths..... | 72 |
| Figure 3.5 Dark field optical microscopy images at various wet etch times. | 75 |
| Figure 3.6 AD-40-AS AFM tip used for nanotip indentation lithography, a) SEM images, b) Depth profile of two different tips measured by AFM..... | 78 |
| Figure 3.7 AFM analysis results of indentation hole pattern, a) 3D AFM image of single hole pattern, b) Change of depth profile according to indentation depth, c) Indentation depth analysis results according to various polymer thicknesses and applied forces | 79 |
| Figure 3.8 Analysis results for the change in opening size of nanohole pattern before and after reactive ion etching using atomic force microscope, a) opening size measurement result before etching, b) opening size | |

measurement result after etching and, c) Analysis result of increase in opening size according to etching depth81

Figure 3.9 Analysis results for the change in opening size of nanohole pattern before and after wet etching using atomic force microscope, a) opening size measurement result before wet etching, b) opening size measurement result after wet etching and, c) Analysis result of increase in opening size according to wet etching time83

Figure 3.10 Measurement result of a) indentation depth and b) diameter according to indentation force for various thicknesses of the 2nd polymer...85

Figure 3.11 SEM images of nanoparticles of various diameters fabricated with the optimized process recipes.....90

Figure 3.12 Nanoparticle fabrication map for nanotip indentation lithography91

Figure 3.13 Large-area nanoparticle array made by nanotip indentation lithography for measurement of optical properties, a) array of PdAu nanoparticles with a diameter of 188.6 nm and a pitch of 300 nm, Array of PdAu nanoparticles with a diameter of 118.8 nm and a pitch of 300 nm, c) Array of PdAu nanoparticles with a diameter of 82.2 nm and a pitch of 150 nm.....92

Figure 3.14 XRD measurement result of large-area nanoparticle array, a) 2Theta-theta scan results from 20° to 90°, b) Detailed analysis of 111 plane peak, c) Result of composition analysis according to the position of the 111-plane peak, d) Schematic diagram of geometric considerations93

| | |
|---|-----|
| Figure 4.1 Schematic diagram of nanoparticle arrays for FDTD simulations, a) the structure of nanoparticles, b) randomly structured nanoparticle array, c) hexagonal structured nanoparticle arrays | 102 |
| Figure 4.2 Hydrogen sensing properties measurement, a) Schematic diagram illustrating response time and recovery time, b) Schematic diagram explaining sensitivity and limit of detection | 105 |
| Figure 4.3 Comparison of sensitivity between random and hexagonal structures, a) Transmittance simulation results of Pd and PdHx in an array of 140 nm diameter nanoparticles with random and hexagonal structures, b) Simulation results of transmittance change according to nanoparticle diameter change..... | 108 |
| Figure 4.4 FDTD simulation results for Pd nanoparticle arrays of various diameter, a) transmittance spectra, b) extinction spectra | 110 |
| Figure 4.5 Measured extinction spectra and simulated results, a) nanoimprinted Pd nanoparticle array, b) nanoimprinted Au nanoparticle array | 114 |
| Figure 4.6 Measured extinction spectra of nanoimprinted PdAu nanoparticle arrays, a) Pd9Au1, b) Pd8Au2, c) Pd7Au3, d) Pd6Au4, e) Pd5Au5, f) Pd4Au6, g) Pd3Au7, h) Pd2Au8, i) Pd1Au9 | 115 |
| Figure 4.7 a) Change of LSPR peak according to Au composition of PdAu alloys, b) Summary of diameter, ratio, pitch, LSPR peak for various PdAu composition | 116 |

Figure 4.8 Measured extinction and transmission spectra of Pd7Au3 nanoparticle arrays for various annealing temperatures, a) extinction and e) transmittance of the sample annealed at 400 °C, b) extinction and f) transmittance of the sample annealed at 500 °C, c) extinction and g) transmittance of the sample annealed at 600 °C, d) extinction and h) transmittance of the sample annealed at 700 °C.....119

Figure 4.9 a) Change of LSPR peak according to annealing temperature, b) Summary of diameter, ratio, pitch, LSPR peak of Pd7Au3 composition for various annealing temperature, c) FDTD simulation results with and without Au 5 nm added to the surface.....120

Figure 4.10 Measured extinction and transmission spectra of PdAu nanoparticle arrays fabricated by nanotip indentation lithography, a) extinction and b) transmittance of the nanoparticle array with a diameter of 182 nm and a pitch of 300 nm, c) extinction and d) transmittance of the nanoparticle array with a diameter of 118.2 nm and a pitch of 300 nm. e) extinction and f) transmittance of the nanoparticle array with a diameter of 82.2 nm and a pitch of 150 nm.....123

Figure 4.11 a) LSPR peak change according to the change in the diameter of nanoparticles, b) Summary of diameter, pitch, measured LSPR peak and simulated LSPR peak124

Figure 4.12 Optical hydrogen measurement results according to various hydrogen contents, a) Nanoimprinted Pd7Au3 nanoparticle array annealed at 400 °C, b) Nanoimprinted Pd7Au3 nanoparticle array annealed at 500 °C, c)

Nanoimprinted Pd7Au3 nanoparticle array annealed at 600 °C, d)
 Nanoimprinted Pd7Au3 nanoparticle array annealed at 700 °C.128

Figure 4.13 Analysis result of response change according to hydrogen partial pressure, a) Nanoimprinted Pd7Au3 nanoparticle array annealed at 400 °C, b)
 Nanoimprinted Pd7Au3 nanoparticle array annealed at 500 °C, c)
 Nanoimprinted Pd7Au3 nanoparticle array annealed at 600 °C, d)
 Nanoimprinted Pd7Au3 nanoparticle array annealed at 700 °C.129

Figure 4.14 Analysis result of response time and recovery time according to hydrogen pressure, a) Nanoimprinted Pd7Au3 nanoparticle array annealed at 400 °C, b) Nanoimprinted Pd7Au3 nanoparticle array annealed at 500 °C, c)
 Nanoimprinted Pd7Au3 nanoparticle array annealed at 600 °C, d)
 Nanoimprinted Pd7Au3 nanoparticle array annealed at 700 °C.130

Figure 4.15 Optical hydrogen measurement results according to various hydrogen contents, a) Nanoimprinted Pd nanoparticle array, b)
 Nanoimprinted Pd9Au1 nanoparticle array, c) Nanoimprinted Pd8Au2 nanoparticle array, d) Nanoimprinted Pd7Au3 nanoparticle array, e)
 Nanoimprinted Pd6Au4 nanoparticle array.....134

Figure 4.16 Analysis result of response change according to hydrogen partial pressure, a) Nanoimprinted Pd nanoparticle array, b) Nanoimprinted Pd9Au1 nanoparticle array, c) Nanoimprinted Pd8Au2 nanoparticle array, d)
 Nanoimprinted Pd7Au3 nanoparticle array.....135

| | |
|---|-----|
| Figure 4.17 Analysis result of response time and recovery time according to hydrogen pressure, a) Nanoimprinted Pd nanoparticle array and b) Nanoimprinted Pd ₇ Au ₃ nanoparticle array..... | 136 |
| Figure 4.18 LoD measurement results for Pd ₇ Au ₃ Nanoparticle Arrays ... | 137 |

List of Tables

| | |
|--|-----|
| Table 1.1 Comparative properties of hydrogen, methane, and gasoline (Energy density and combustion) [2,3]. | 5 |
| Table 2.1 Calculated deposition thickness for PdAu Compositions of various weight ratio..... | 39 |
| Table 2.2 Binding energy, atomic percentage (at%) and oxide ratio of PdAu nanoparticle arrays analyzed by XPS results | 51 |
| Table 3.1 The optimized process recipes for nanotip indentation lithography | 89 |
| Table 4.1 Comparison of hydrogen sensing properties for Pd nanoparticle array and Pd ₇ Au ₃ nanoparticle array..... | 138 |

Chapter 1. Plasmonic hydrogen sensor:

Principle and major material

1.1. Introduction

In the face of the global crisis of climate change, the international community is focusing on carbon neutrality. Hydrogen is a resource that is attracting attention as an alternative to fossil fuels to reduce carbon emissions [1]. As an energy storage medium, hydrogen can be used to store energy by using surplus energy such as solar, wind, thermal, and nuclear power. Hydrogen can be produced by electrolysis of water using surplus electrical energy [2,3]. The produced hydrogen is stored, transported, distributed and used again as an energy source [4,5]. Currently, hydrogen is used the most as a raw material, but it is expected to gradually increase for hydrogen vehicles and hydrogen power generation [6].

As an energy resource, hydrogen has excellent properties. The energy density of hydrogen is 142 kJ/g, which is 3 times that of gasoline and 2.6 times that of LNG [7]. However, hydrogen has a very wide flammability range of 4 to 75%, a very small minimum ignition energy of 0.02 mJ, and a very high flame speed, making it vulnerable to explosion [2,3]. Therefore, for

the hydrogen economy to become a reality, a hydrogen sensor that can quickly detect a hydrogen leak is essential.

As an ideal hydrogen sensor, various specifications are required [4].

- (1) Hydrogen measurement range 0.01 - 10 vol% for safety or 1-100 vol% for fuel cell.
- (2) Operating environment:
 - Temperature ($-30-80\text{ }^{\circ}\text{C}$ (safety), $70-150\text{ }^{\circ}\text{C}$ (fuel cells))
 - Pressure (80–110 kPa)
 - Relative humidity (10–98%)
- (3) Reliable accuracy and sensitivity (Uncertainty within 5%)
- (4) Selectivity for hydrogen gas in reducing gases (CO, NO, H₂S)
- (5) Fast response time and recovery time ($< 1\text{ s}$)
- (6) Low noise and stable signal
- (7) Sufficient lifetime (>5 years)
- (8) Low cost and power consumption
- (9) Small size and simple system

Currently, major commercial hydrogen sensors are mainly electrical sensors such as catalytic sensors, thermal conductivity sensors, electrochemical sensors, and resistive sensors. Optical hydrogen sensors are competitive candidates for a wide range of applications because of their inherent immunity to EMI and their non-explosiveness. Metal hydride-based optical hydrogen sensors have been continuously studied because of their fast

response speed, high sensitivity, and wide measurement range [8]. However, the commonly used thin film-based metal hydride sensor has been limited in its use due to its low durability and short lifetime.

When the thin-film metal becomes a metal hydride, internal stress occurs because volume expansion is limited by the clamping effect of the substrate [9]. The low durability of the thin film type hydrogen sensor is because fatigue failure is induced by the stress generated by volume expansion [10]. To overcome this, a hydrogen sensor using nanoparticles instead of a thin film has been proposed. Since the optical properties of metal nanoparticles can be explained by localized surface plasmon resonance (LSPR), the nanoparticle-based optical hydrogen sensor is called an LSPR-based hydrogen sensor [11-13].

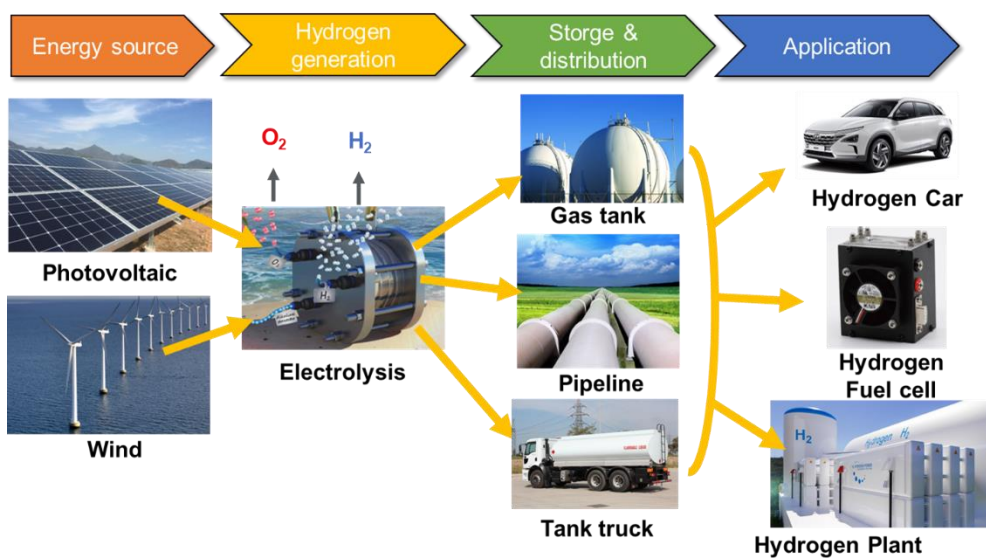


Figure 1.1 Schematic diagram of hydrogen production, storage, distribution, and use.

Table 1.1 Comparative properties of hydrogen, methane, and gasoline (Energy density and combustion) [2,3].

| Property | Hydrogen | Methane | Gasoline |
|--------------------------------|----------|------------|-------------|
| Density (Kg/m ³) | 0.082 | 0.717 | 5.11 |
| Higher heating value (MJ/kg) | 141.7 | 52.68 | 48.29 |
| Lower heating value (MJ/kg) | 119.7 | 46.72 | 44.29 |
| combustion properties | | | |
| Flammability limits (volume %) | 4 - 75 | 5.3 - 15.0 | 1.2 - 6.0 |
| Minimum ignition energy (mJ) | 0.02 | 0.28 | 0.25 |
| Laminar flame speed (m/s) | 1.90 | 0.38 | 0.37 - 0.43 |
| Autoignition temperature (°C) | 585 | 540 | 227 - 477 |

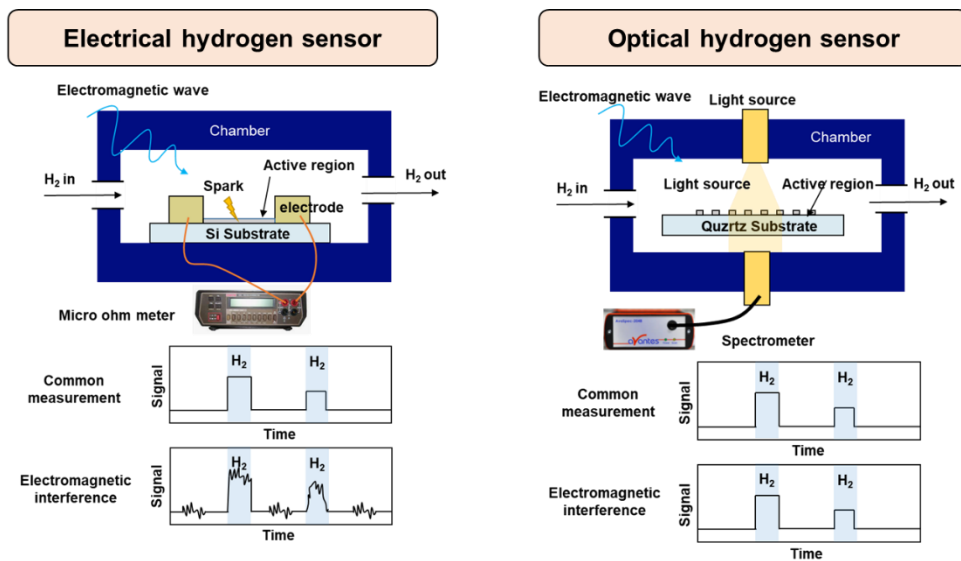


Figure 1.2 Advantages of optical hydrogen sensors compared to electrical hydrogen sensors.

1.2. History of LSPR based optical hydrogen sensor

In 2007, for the first time, C. Langhammer et al. experimentally demonstrated the feasibility of an LSPR-based hydrogen sensor by measuring the changes in the plasmonic resonance peak shift and extinction values of Pd nanodisks by hydrogen exposure [14]. In 2010, I. Zorić showed that the hydrogen concentration inside Pd nanodisks and nanorings can be measured by detecting the variation of LSPR peak and extinction value [15]. In 2012, C. Langhammer et al. conducted experiments to optimize the thickness of Pd nanorings and reported that the hysteresis was almost disappeared at a wall thickness of 20 nm. [16]. N. Strohhfeldt et al. demonstrated that the structure of CaF_2 10 nm / Pd 20 nm / Pt 3 nm improved the stability of the Pd layer and reported that the $\text{Pd}_{98}\text{Ni}_2$ composition had a faster response time than that of Pd [17]. In 2019, F. A. A. Nugroho et al. demonstrated that the response time and hydrogen selectivity of $\text{Pd}_{70}\text{Au}_{30}$ nanodisc arrays can be improved by a double protective layer of PTFE and PMMA [18].

There have also been studies on LSPR based sensors using materials other than Pd. Devika Sil et al. demonstrated for the first time the optical measurement of hydrogen using the plasmonic resonance of gold nanoparticles [19]. N. Strohhfeldt et al. demonstrated a hydrogen sensor using yttrium nanorods with a reversible phase change from YH_2 to YH_3 , which had a response time of less than 50 seconds at a hydrogen concentration of 5

vol% [20]. However, the formation of Y_2O_3 in this sensor reduces the diffusion and permeation of hydrogen and increases the response time.

Because the LSPR spectral change is sensitive and efficient for hydrogen detection, the LSPR-based hydrogen sensor has overall excellent sensor characteristics. However, since the fabrication cost of the nanoparticle arrays is high, it is a challenge to lower the manufacturing cost and increase reproducibility.

1.3. Principle of LSPR based optical hydrogen sensor

LSPR is a non-propagating SPR confined to the closed surface of a nanoparticle [21]. The collective oscillation of the free electrons within the nanoparticles is caused by the electric field of the incident light [22]. Since free electrons are confined within the nanoparticles, an enhanced surface radiation electric field is generated on the surface of the nanoparticles [23]. LSPR is excited when the frequency of incident light coincides with the natural frequency of free electrons in the material, and is expressed as:

$$\omega_{LSP} = \frac{\omega_p}{\sqrt{1 + 2\varepsilon_d}} \quad (1)$$

$$\omega_p = \sqrt{\frac{Ne^2}{m\varepsilon_d}} \quad (2)$$

where ω_{LSP} is the resonant frequency of localized surface plasmon, ω_p is the resonant frequency of plasmon, ε_d is the dielectric constant of the surrounding medium, N is the number of free electrons in a unit volume, and m is the mass of electrons. The LSPR frequency/wavelength is inherently dependent on the material, size and shape of the nanoparticle. The resonance of the LSP causes strong absorption and scattering, resulting in resonance peaks in the absorption, scattering, and extinction spectra.

The measurement system and operation principle of the LSPR-based hydrogen sensor are shown in Figure 1.3. The LSPR measurement system

consists of a gas chamber, a light source, and a spectrometer as shown in Figure 1.3(a). The optical properties of metal hydrides are different from those of metals and the LSPR spectrum shifts accordingly. By recording the change of LSPR spectrum with time, a measurement graph can be obtained as shown in Figure 1.3(d), and the detection characteristics of the LSPR sensor can be obtained by analyzing this graph.

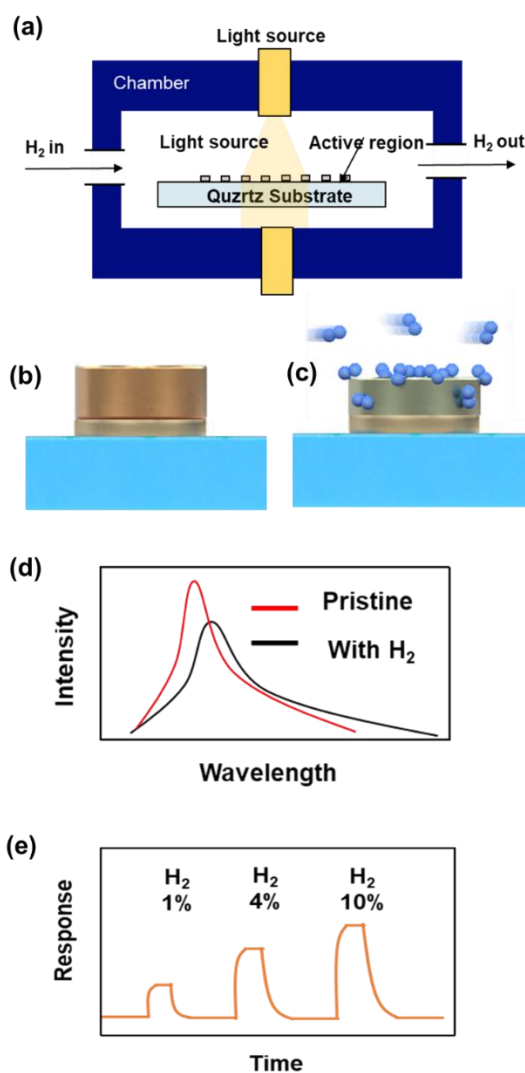


Figure 1.3 Measurement system and operation principle of LSPR-based hydrogen sensor, (a) LSPR-based sensor measurement system, (b) Pristine palladium nanoparticle, (c) Palladium nanoparticle with hydrogen, (d) Changes in the LSPR spectrum due to hydrogen absorption, (e) Measuring the time-dependent change of the LSPR spectrum.

1.4. Major materials for LSPR based optical hydrogen sensor

Palladium has high sensitivity and selectivity to hydrogen, so it is the most selected hydrogen sensing material to detect hydrogen at room temperature [24]. Palladium can absorb up to 900 times its own volume of hydrogen gas [25]. When Pd is changed to PdH_x in a hydrogen environment, two phases (α phase and β phase) are observed. The difference between the α -phase and the β phase is the amount of hydrogen containing, and the β phase contains more hydrogen than the α -phase. The lattice constant of palladium is 388.9 pm, and the lattice constants of the α -phase and the β phase of PdH_x are 389.5 pm and 402.5 pm, respectively [26]. The volume of the β phase is about 11% larger than that of the α phase [27]. This volume expansion can cause the embrittlement effect of palladium to decrease its durability. When the hydrogen content of PdH_x is less than 3%, only the α phase is observed. When the hydrogen content of PdH_x is 3% ~ 58%, the α + β phase is observed, and in the case of above 58%, only the β phase is observed [28,29]. In the concentration region with the α + β phase, a phase transition occurs from alpha to beta phase, resulting in hysteresis [15]. Hysteresis due to phase transition degrades the measurement accuracy and reproducibility of the sensor. When pure palladium is used as a sensor material, there is no way to eliminate the hysteresis effect due to the α - β phase transition.

By alloying palladium with other metals, the effects of embrittlement and hysteresis can be mitigated. In previous studies, Palladium was alloyed with Ag[30,31], Au[32-35], Ni[36,37] and Y[38] to improve structural stability and reduce hysteresis. When tuning alloy composition, sensitivity and stability are in a trade-off relationship. In PdAu alloys, the higher the Au content, the lower the hysteresis but the lower the optical contrast. There is a critical concentration to suppress hysteresis through the alloy, and for PdAu alloy, the critical concentration of Au is 17%. The PdAg alloy has a high hydrogen permeability and a fast reaction time [39]. However, the mechanical strength after hydrogenation is very low enough to cause distortion in the data [40]. PdNi alloy is an alloy that has economic advantages over other alloys. PdNi alloy has excellent durability and sensitivity but exhibits a relatively slow response time. Using the composition of the PdAuCu ternary system, a very good reaction time of 0.4 s at 5 ppm was also shown without surface treatment or promote polymer [41]. Attempting to improve the properties of sensors by ternary alloying is very challenging, but it is worth trying because it can lead to great property improvements. Generally, the best choice will be the PdAu composition.

1.5. Fabrication methods for LSPR based optical hydrogen sensor

For LSPR to occur, the size of the nanoparticles must be sufficiently smaller than the wavelength of the incident light. The LSPR is well observed in nanoparticles with diameters less than 200 nm. Methods that can be made by patterning these nanoparticles include photolithography, electron beam lithography, nanoimprint lithography, nanosphere lithography and nanotip indentation lithography.

Photolithography is a lithography method in which a pattern made on a photomask is transferred to a photosensitive polymer on a substrate using light, a developed pattern is made, and a desired structure is obtained through deposition. Photolithography allows micro-to-nano-scale patterns to be fabricated. The resolution of photolithography can be improved to hundreds of nanometers using phase-shifting masks [5,42,43]. However, there is a limit because expensive equipment and research must be supported to control patterns of hundreds of nanometers.

Electron beam lithography is a lithography method that uses an electron beam to make a pattern on a polymer sensitive to exposure of a substrate and develops it to make a nanopattern. Electron beam lithography is a very powerful method for fabricating nanometer-scale patterns [6,44]. Electron beam lithography has the highest resolution and is the most precise lithography method, but expensive equipment and maintenance must be

supported, and sufficient research must be done to make a single nanoscale pattern. In addition, there is a disadvantage that the throughput is very low, and the lithography process is greatly affected by the substrate.

Nanoimprint lithography is a lithography method that can compensate for the low throughput of electron beam lithography and maintain high resolution in nanopattern fabrication. The mold used for nanoimprint is manufactured by electron beam lithography, and the pattern of the mold can be transferred to a polymer for nanoimprint using hot-pressing or UV curing to produce a nanopattern [45]. It has been demonstrated that sub-5 nm feature sizes are possible using nanoimprint lithography [46]. Nanoimprint lithography is the most ideal method for fabricating nanoparticle patterns in terms of throughput and resolution. However, in practice, electron beam lithography can be used to manufacture a mold of a nano-size pattern, or it must be purchased through a related company. Using electron beam lithography on its own is also expensive, but even with commercial purchases, sub-100nm patterns are expensive and require additional research funding. Also, changing the mold is necessary to change the pattern. Therefore, most of the funds required for nanoimprint lithography are used to manufacture the mold.

Nanosphere lithography is the most inexpensive lithography method to make nanoparticle patterns. In nanosphere lithography, monodisperse nanospheres are patterned as a monolayer on a substrate, and patterns are fabricated using the nanospheres as a mask, and a nanopattern is produced

using this pattern [47]. Although nanosphere lithography has the advantage of high throughput, it has a limitation in resolution that it is difficult to fabricate nanoparticle patterns of 100 nm or less. If the nanospheres in the monolayer are not close-packed, the nanospheres are randomly arranged. For this reason, there is also a disadvantage of low reproducibility.

Nanotip indentation lithography is a method of making a nanoparticle array using an AFM tip. A single crystal diamond nanotip is used to make holes on the polymer for nanopatterning, and the nanoparticle array is fabricated by using this hole pattern. Nanotip indentation lithography has the advantage that the size of nanoparticles can be precisely controlled and the degree of freedom in substrate selection is high. However, it has the disadvantages of low throughput and the need for calibration at each tip.

1.6. Purpose and organization of this thesis

The purpose of this dissertation is to diversify the manufacturing method of nanoparticle array for LSPR-based hydrogen sensor, to propose a method to efficiently control the size of nanoparticles, and to improve sensitivity, response time, recovery time, and LoD (limit of detection) of hydrogen sensors.

Chapter 2 discusses the fabrication of plasmonic nanoparticle arrays through nanoimprint lithography, and the characteristics of various palladium gold alloy compositions and the change in the composition of Pd₇Au₃ according to various annealing temperatures was investigated.

Chapter 3 discusses the fabrication of plasmonic nanoparticle arrays via nanotip indentation lithography. The change of nanoparticle diameter according to process parameters in nanotip indentation lithography was investigated. Fabrication of nanoparticle arrays with diameters between 60 nm and 130 nm through nanotip indentation lithography was demonstrated. In addition, the geometric effect on the formation of palladium gold composition through nanotip indentation was investigated.

Chapter 4 discusses the optical and hydrogen sensing properties of the fabricated palladium and palladium-gold plasmonic nanoparticle arrays. Changes in LSPR spectrum according to various PdAu compositions and annealing temperatures were investigated, and changes in LSPR spectra of etched Pd nanoparticle arrays and nanoparticle arrays fabricated by nanotip

indentation were also investigated. The characteristics of the LSPR-based hydrogen sensor according to the palladium-gold composition and the annealing temperature were investigated, and the mechanism by which the characteristics appeared was explained.

Finally, the conclusion of this dissertation is presented in Chapter 5.

1.7. Bibliography

- [1] L.P. Bicelli, “Hydrogen: a clean energy source”, International journal of hydrogen energy, 11(9), (1986), 555-562.
- [2] G.A. Karim, “Hydrogen as a spark ignition engine fuel”, International Journal of Hydrogen Energy, 28(5), (2003), 569-577.
- [3] L. Andre, J. Heffel, and C. Messer, “Hydrogen fuel cell engines and related technologies”, No. FTA-CA-26-7022-01.1, United States Department of Transportation, Federal Transit Administration, (2001).
- [4] T. Hübert, L. Boon-Brett, G. Black and U. Banach, “ Hydrogen sensors—a review”, Sensors and Actuators B: Chemical, 157(2), (2011), 329-352.
- [5] T. Faure, Y. Sakamoto, Y. Toda, K. Badger, K. Seki, M. Lawliss and K. Nishikawa, “Development of a new high transmission phase shift mask technology for 10 nm logic node.”, Photomask Japan 2016: XXIII Symposium on Photomask and Next-Generation Lithography Mask Technology. SPIE, (2016), p. 998402.
- [6] K.Yamazaki and H. Namatsu, "5-nm-order electron-beam lithography for nanodevice fabrication." Japanese Journal of Applied Physics, 43.6S, (2004), 3767.
- [7] J.A. Okolie, B. R. Patra, A. Mukherjee, S. Nanda, A. K. Dalai and J. A. Kozinski, "Futuristic applications of hydrogen in energy, biorefining, aerospace, pharmaceuticals and metallurgy." International Journal of Hydrogen Energy, 46.13, (2021), 8885-8905.
- [8] L.J. Bannenberg, C. Boelsma, K. Asano, H. Schreuders and B. Dam,

- "Metal hydride based optical hydrogen sensors." *Journal of the Physical Society of Japan*, 89.5, (2020), 051003.
- [9] M. Khanuja, B. R. Mehta, P. Agar, P. K. Kulriya and D. K. Avasthi, "Hydrogen induced lattice expansion and crystallinity degradation in palladium nanoparticles: Effect of hydrogen concentration, pressure, and temperature." *Journal of Applied Physics*, 106.9, (2009), 093515.
- [10] M.A. Butler, "Micromirror optical-fiber hydrogen sensor." *Sensors and actuators B: Chemical*, 22.2, (1994), 155-163.
- [11] E. Filippo, A. Serra and D. Manno, "Poly (vinyl alcohol) capped silver nanoparticles as localized surface plasmon resonance-based hydrogen peroxide sensor." *Sensors and Actuators B: Chemical*, 138.2, (2009), 625-630.
- [12] J.O. Kvítek, J. Siegel, V. Hnatowicz and V. Švorčík, "Noble metal nanostructures influence of structure and environment on their optical properties." *Journal of Nanomaterials*, 2013, (2013).
- [13] C. Wadell, S. Syrenova and C. Langhammer, "Plasmonic hydrogen sensing with nanostructured metal hydrides." *ACS nano* 8.12, (2014), 11925-11940.
- [14] C. Langhammer, I. Zorić, B. Kasemo and B.M. Clemens, "Hydrogen storage in Pd nanodisks characterized with a novel nanoplasmonic sensing scheme." *Nano Letters*, 7.10, (2007), 3122-3127.
- [15] I. Zoric, E.M. Larsson, B. Kasemo and C. Langhammer, "Localized surface plasmons shed light on nanoscale metal hydrides." *Advanced Materials*, 22.41 (2010): 4628-4633.
- [16] C. Langhammer, E.M. Larsson, V.P. Zhdanov and I. Zoric, "Asymmetric hysteresis in nanoscopic single-metal hydrides:

- palladium nanorings." *The Journal of Physical Chemistry C*, 116.40, (2012), 21201-21207.
- [17] N. Strohfeldt, A. Tittl and H. Giessen, "Long-term stability of capped and buffered palladium-nickel thin films and nanostructures for plasmonic hydrogen sensing applications." *Optical Materials Express* 3.2, (2013), 194-204.
- [18] F.A. Nugroho, I. Darmadi, L. Cusinato, A. Susarrey-Arce, H. Schreuders, L.J. Bannenberg and C. Langhammer, "Metal-polymer hybrid nanomaterials for plasmonic ultrafast hydrogen detection." *Nature materials*, 18.5, (2019), 489-495.
- [19] D. Sil, K.D. Gilroy, A. Niaux, A. Boulesbaa, S. Neretina and E. Borguet, "Seeing is believing: Hot electron based gold nanoplasmonic optical hydrogen sensor." *ACS nano*, 8.8, (2014), 7755-7762.
- [20] N. Strohfeldt, A. Tittl, M. Schäferling, F. Neubrech, U. Kreibig, R. Griessen and H. Giessen, "Yttrium hydride nanoantennas for active plasmonics." *Nano letters*, 14.3, (2014), 1140-1147.
- [21] V. A. G. Rivera, F. A. Ferri and E. Marega Jr., "Localized surface plasmon resonances: noble metal nanoparticle interaction with rare-earth ions." *Plasmonics-Principles and Applications*, (2012), 283-312.
- [22] B.J. Wiley, S.H. Im, Z. Y. Li, , J. McLellan, A. Siekkinen and Y. Xia, "Maneuvering the surface plasmon resonance of silver nanostructures through shape-controlled synthesis." *The Journal of Physical Chemistry B*, 110.32, (2006), 15666-15675.
- [23] M.A. El-Sayed, "Some interesting properties of metals confined in time and nanometer space of different shapes." *Accounts of chemical research* 34.4, (2001), 257-264.

- [24] C.H. Wu, Z. Zhu, S. Y. Huang and R. J. Wu, "Preparation of palladium-doped mesoporous WO₃ for hydrogen gas sensors." *Journal of Alloys and Compounds*, 776, (2019), 965-973.
- [25] R. Tabassum and B.D. Gupta, "Fiber optic hydrogen gas sensor utilizing surface plasmon resonance and native defects of zinc oxide by palladium." *Journal of Optics* 18.1, (2015), 015004.
- [26] F. D. Manchester, A. San-Martin and J. M. Pitre, "The H-Pd (hydrogen-palladium) system." *Journal of phase equilibria*, 15.1, (1994), 62-83.
- [27] P. C. Aben and W. G. Burgers, "Surface structure and electrochemical potential of palladium while absorbing hydrogen in aqueous solution." *Transactions of the Faraday Society*, 58, (1962), 1989-1992.
- [28] H. Akiba, H. Kobayashi, H. Kitagawa, M. Kofu and O. Yamamuro, "Glass transition and positional ordering of hydrogen in bulk and nanocrystalline palladium." *Physical Review B*, 92.6, (2015), 064202.
- [29] H. Frieske and E. Wicke, "Magnetic susceptibility and equilibrium diagram of PdH_n." *Berichte der Bunsengesellschaft für physikalische Chemie*, 77.1, (1973), 48-52.
- [30] M. Zou, Y. Dai, X. Zhou, K. Dong and M. Yang, "Femtosecond laser ablated FBG with composite microstructure for hydrogen sensor application." *Sensors*, 16.12, (2016), 2040.
- [31] J. Dai, M. Yang, X. Yu and H. Lu, "Optical hydrogen sensor based on etched fiber Bragg grating sputtered with Pd/Ag composite film." *Optical Fiber Technology*, 19.1, (2013), 26-30.
- [32] R.J. Westerwaal, J.S.A. Rooijmans, L. Leclercq, D.G. Gheorghe, T. Radeva, L. Mooij and T. Rasing, "Nanostructured Pd–Au based fiber

- optic sensors for probing hydrogen concentrations in gas mixtures." *International Journal of Hydrogen Energy*, 38.10, (2013), 4201-4212.
- [33] F. Gu, G. Wu, and H. Zeng, "Hybrid photon–plasmon Mach–Zehnder interferometers for highly sensitive hydrogen sensing." *Nanoscale*, 7.3, (2015), 924-929.
- [34] D. Luna-Moreno and D. Monzón-Hernández, "Effect of the Pd–Au thin film thickness uniformity on the performance of an optical fiber hydrogen sensor." *Applied Surface Science*, 253.21, (2007), 8615-8619.
- [35] D. Monzón-Hernández, D. Luna-Moreno and D. Martínez-Escobar, "Fast response fiber optic hydrogen sensor based on palladium and gold nano-layers." *Sensors and Actuators B: Chemical*, 136.2, (2009), 562-566.
- [36] J. Dai, M. Yang, X. Yu, K. Cao and J. Liao, "Greatly etched fiber Bragg grating hydrogen sensor with Pd/Ni composite film as sensing material." *Sensors and Actuators B: Chemical*, 174, (2012), 253-257.
- [37] J. Dai, M. Yang, Z. Yang, Z. Li, Y. Wang, G. Wang and Z. Zhuang, "Enhanced sensitivity of fiber Bragg grating hydrogen sensor using flexible substrate." *Sensors and Actuators B: Chemical*, 196, (2014), 604-609.
- [38] Y. Liu and L.Y. Li, "Enhanced sensitivity of transmission based optical fiber hydrogen sensor with multi-layer Pd–Y alloy thin film." *Sensors and Actuators B: Chemical*, 227, (2016), 178-184.
- [39] A. G. Knapton, "Palladium alloys for hydrogen diffusion membranes: a review of high permeability materials." *Platinum Metals Review*, 21.2, (1977), 44-50.

- [40] D. Fort, J. P. G. Farr and I. R. Harris, "A comparison of palladium-silver and palladium-yttrium alloys as hydrogen separation membranes." *Journal of the Less common metals* 39.2, (1975), 293-308.
- [41] I. Darmadi, F. A. A. Nugroho, S. Kadkhodazadeh, J.B. Wagner and C. Langhammer, "Rationally designed pdaucu ternary alloy nanoparticles for intrinsically deactivation-resistant ultrafast plasmonic hydrogen sensing." *ACS sensors*, 4.5, (2019), 1424-1432.
- [42] M.D. Levenson, N. S. Viswanathan and A.S. Robert, "Improving resolution in photolithography with a phase-shifting mask." *IEEE Transactions on electron devices* 29.12, (1982), 1828-1836.
- [43] T. Ito and S. Okazaki, "Pushing the limits of lithography." *Nature*, 406.6799, (2000), 1027-1031.
- [44] K. Liu, P. Avouris, J. Bucchignano, R. Martel, S. Sun and J. Michl, "Simple fabrication scheme for sub-10 nm electrode gaps using electron-beam lithography." *Applied Physics Letters*, 80.5, (2002), 865-867.
- [45] J.J. Guo, "Nanoimprint lithography: methods and material requirements." *Advanced materials*, 19.4, (2007), 495-513.
- [46] W.D. Li, W. Wu and R. Stanley Williams, "Combined helium ion beam and nanoimprint lithography attains 4 nm half-pitch dense patterns." *Journal of Vacuum Science & Technology B, Nanotechnology and Microelectronics: Materials, Processing, Measurement, and Phenomena*, 30.6, (2012), 06F304.
- [47] P. Colson, C. Henrist and R. Cloots, "Nanosphere lithography: a powerful method for the controlled manufacturing of nanomaterials."

Journal of Nanomaterials, 2013, (2013).

Chapter 2. Fabrication of PdAu nanoparticle arrays using nanoimprint lithography

2.1. Introduction

Nanoimprint lithography (NIL) is a highly efficient lithography technique for performing high-precision, low-cost, high-throughput patterning of polymer nanostructures [1]. Nanoimprint lithography uses UV curing [2] or thermal compression [3,4] to form nanostructured patterns on resist polymers. This chapter deals only with nanoimprint using thermal compression.

The conventional optical plasmonic sensor was manufactured using nanosphere lithography method using PS nano beads [5-10]. The advantage of this method is that it can manufacture hundreds of nanometers of nanodisk inexpensively [11], but it has a disadvantage of being a random pattern and poor reproducibility.

In this chapter, the fabrication of hexagonal nanoparticle arrays using nanoimprint lithography to replace conventional nanosphere lithography with poor reproducibility was demonstrated. A 5 nm Ti buffer layer was used to improve the adhesion between the PdAu alloy and the quartz substrate, and

the PdAu alloy was used as the active material for the hydrogen sensor. The shape and composition of the fabricated nanoparticle array was observed by SEM, TEM and EDX, and the change in surface composition according to the annealing temperature was analyzed by XPS. In addition, the diffraction patterns of various PdAu compositions were analyzed by XRD.

2.2. Experimental procedures

2.2.1. Nanoparticle array fabrication procedures using nanoimprint lithography

Process flow of a nanoparticle array fabrication using nanoimprint lithography was shown in Figure 2.1. For optical hydrogen measurement, a quartz substrate (Korea Science) having a size of 2 cm x 2 cm was used. First, the quartz substrate was cleaned using acetone and IPA. The 1st polymer layer, PMGI SF3, was spin-coated on a quartz substrate at 5,000 rpm for 50 sec and the substrate was baked on a hot plate at 200°C for 5 min. After 5 minutes of natural air cooling, the 2nd polymer layer, MR-I 8010r, was spin-coated on a quartz substrate at 3,000 rpm for 30 sec and the substrate was baked on a hot plate at 100°C for 1 min. The nanopattern of nanoimprint mold (PTRN 73, Eulitha) was placed on the surface of the substrate on which the nanopatterning polymer was deposited. The mold and the substrate were thermocompressed at a temperature of 170°C and a pressure of 25 bar for 3 minutes. After lowering the temperature of the substrate and the mold to 90°C through air cooling, the substrate and the mold were separated. The 2nd polymer layer, MR-I 8010r, was etched under reactive ion etching conditions of 70 mtorr, Ar 6sccm, O₂ 10sccm, and Power 20W to expose the 1st

polymer layer. Then, the substrate was wet-etched for 2 seconds using AZ MIF 300 developer. After cleaning with DI water and drying the hot plate at 60°C, Ti/Pd/Au was deposited on the substrate using an e-beam evaporator. To lift off the deposited substrate, the substrate was washed with acetone, AZ MIF 300 developer, and IPA in that order.

An annealing process was performed as shown in Fig. 2.2 to alloy with the deposited Pd and Au. Annealing was performed at a heating rate of 5 °C/min up to 100°C and at a heating rate of 1 °C/min up to the maximum temperature. The ambient atmosphere was argon containing 4% H₂. After annealing, the furnace temperature was lowered through air cooling.

2.2.2. Material characterization

The thickness of two spin-coated polymer layers and the height of nanoparticles were observed through AFM. In addition, the morphology of nanoimprint molds and nanoparticle arrays was observed by SEM. XRD was used to analyze the crystallinity changes of various PdAu compositions and rocking curve analysis was performed for detailed analysis. XPS was used to analyze the surface composition change at various annealing temperatures.

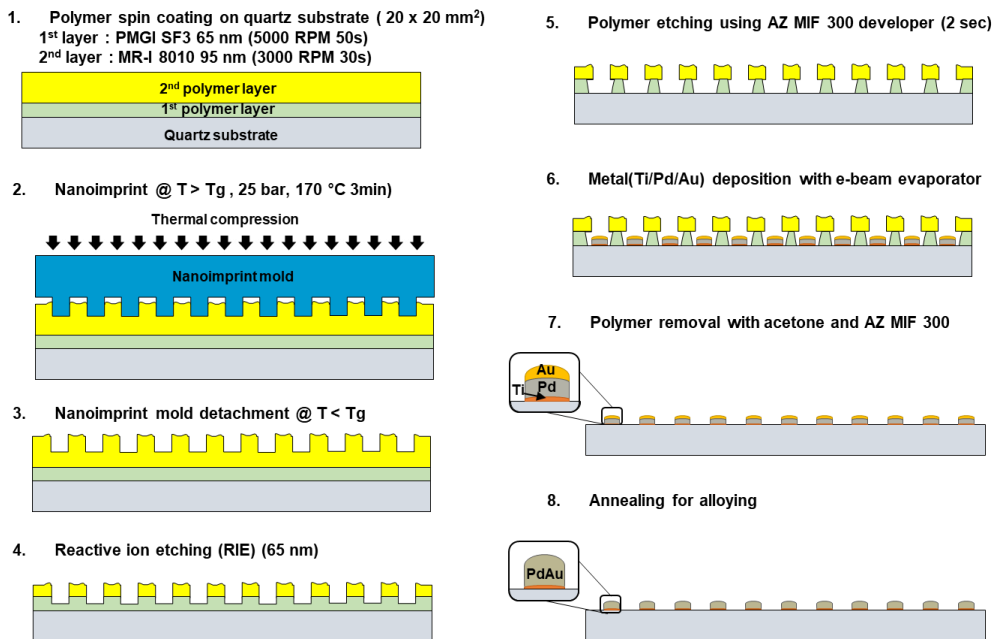


Figure 2.1 Process flow of nanoimprint lithography.

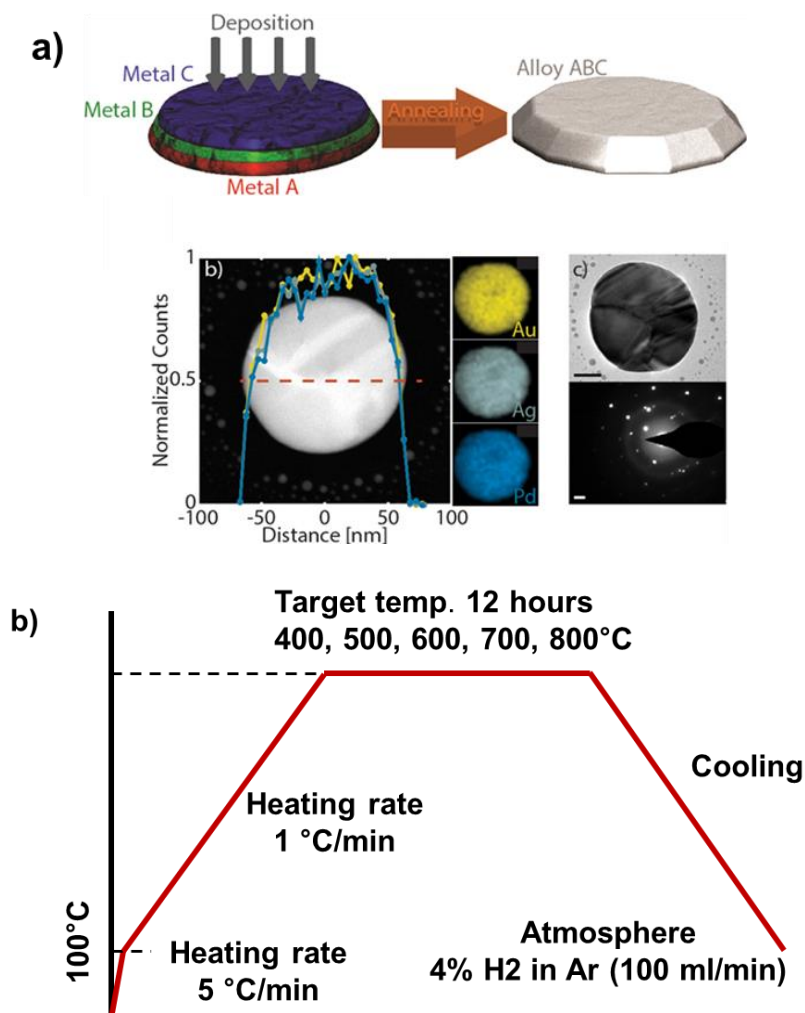


Figure 2.2 Annealing conditions for PdAu alloys, a) Schematic diagram of alloy formation through annealing of multi-layer thin film [12], b) Schematic diagram of annealing process.

2.3. Results and discussions

2.2.1. Fabrication results of PdAu NP arrays

First, the thickness analysis results of two polymer layers for nanoimprint lithography was shown in Figure 2.3. It was observed that the 1st polymer (PMGI SF3) and the 2nd polymer (MR-I 8010r) were 65 nm and 95 nm thick, respectively. The SEM image of the nanoimprint mold was shown in Figure 2.4. The nanoparticle shape of the mold was closer to an ellipse than a perfect circle. The average diameters of the long axis and short axis were 147 ± 6 nm and 122 ± 9 nm, respectively. The ratio of the short axis to the long axis was 0.83. The height of the mold pattern was 98 nm and the pitch between nanoparticles was 200 nm. The height measurement result of the pattern formed on the surface of the 2nd polymer after nanoimprinting was shown in Figure 2.5. Although the height of the mold was 98 nm, the depth of the pattern formed on the surface was measured to be 65 nm. The thermal compression process was disturbed by air trapped between the substrate and the mold [air trap]. So, the depth of nanoimprinted pattern was decreased. To expose the surface of the 1st polymer (PMGI SF3), it was necessary to etch a thickness of 30 nm or more. Thus, the sample was etched to a sufficient thickness of 65 nm. The SEM image of the nanoparticle array obtained after all subsequent processes was

shown in Figure 2.6. The average diameter of the finished nanoparticles was 161 ± 7 nm on the long axis and 148 ± 6 nm on the short axis. The ratio of the short axis to the long axis was 0.93 and it was analyzed to be closer to a circular shape than the nanoimprint mold. Through the SEM image measured at x10,000 magnification, it was found that nanoparticles were uniformly formed in a wide area. The deposition thicknesses for various PdAu compositions were listed in Table 2.1.

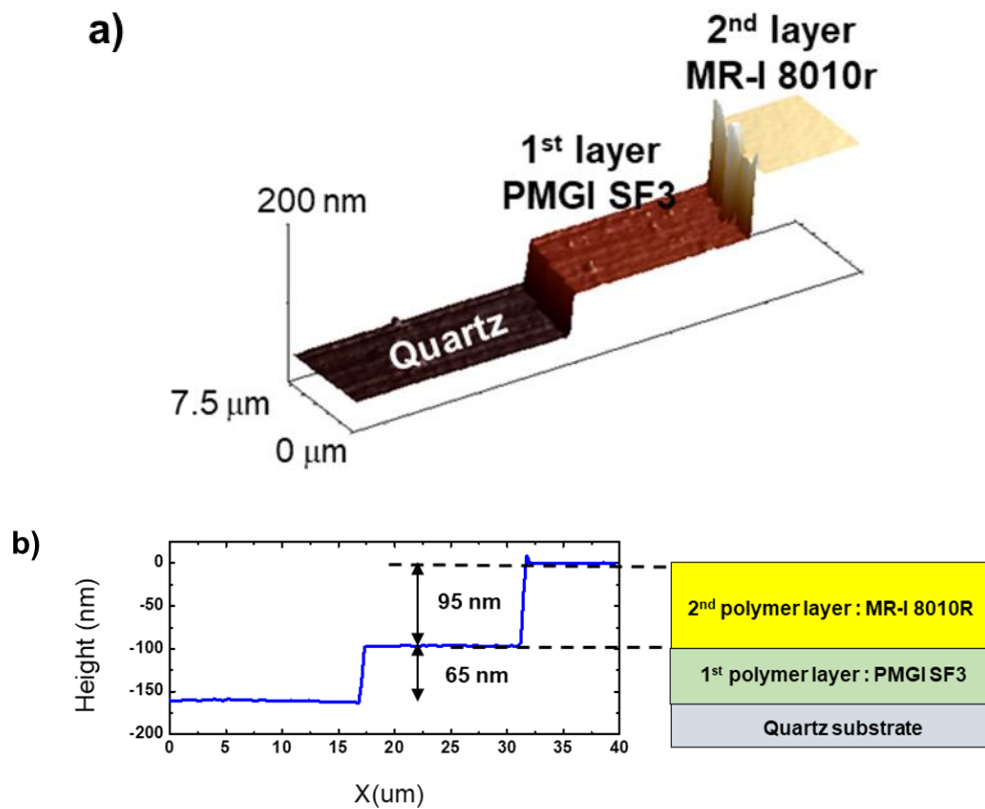


Figure 2.3 Thickness analysis result of two polymer layer fabricated by spin coating, a) 3D AFM image of the step height for two polymer layers, b) Height profiles for two polymer layers.

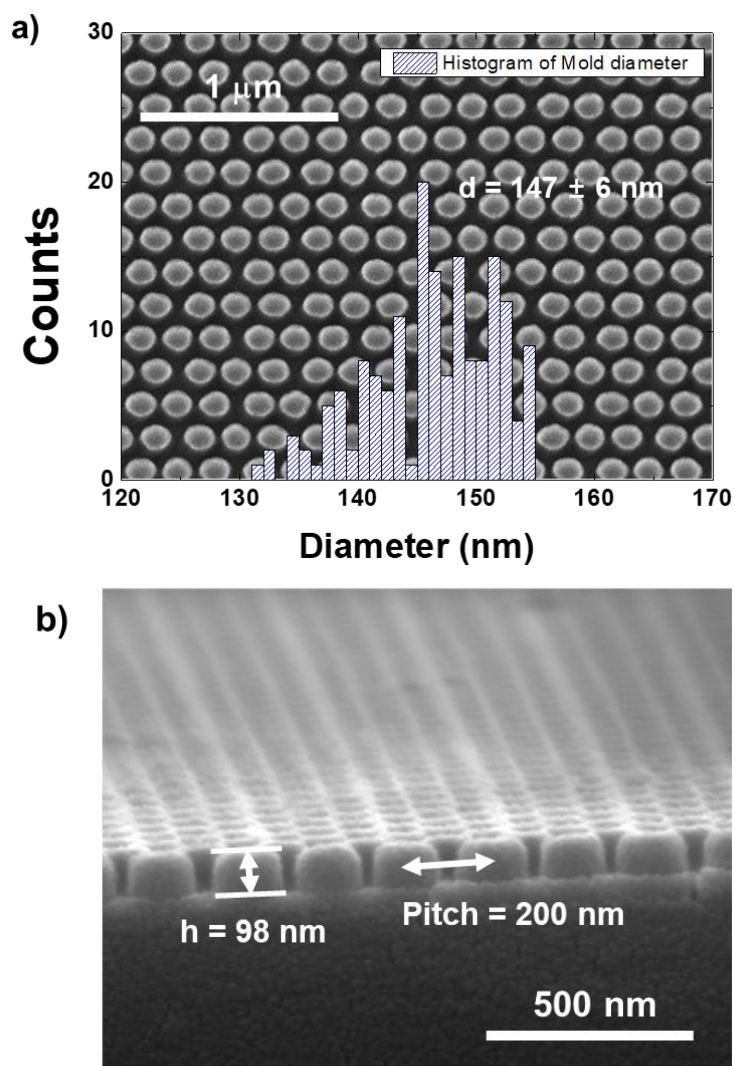


Figure 2.4 SEM image of nanoimprint mold a) top-view b) bird eye view.

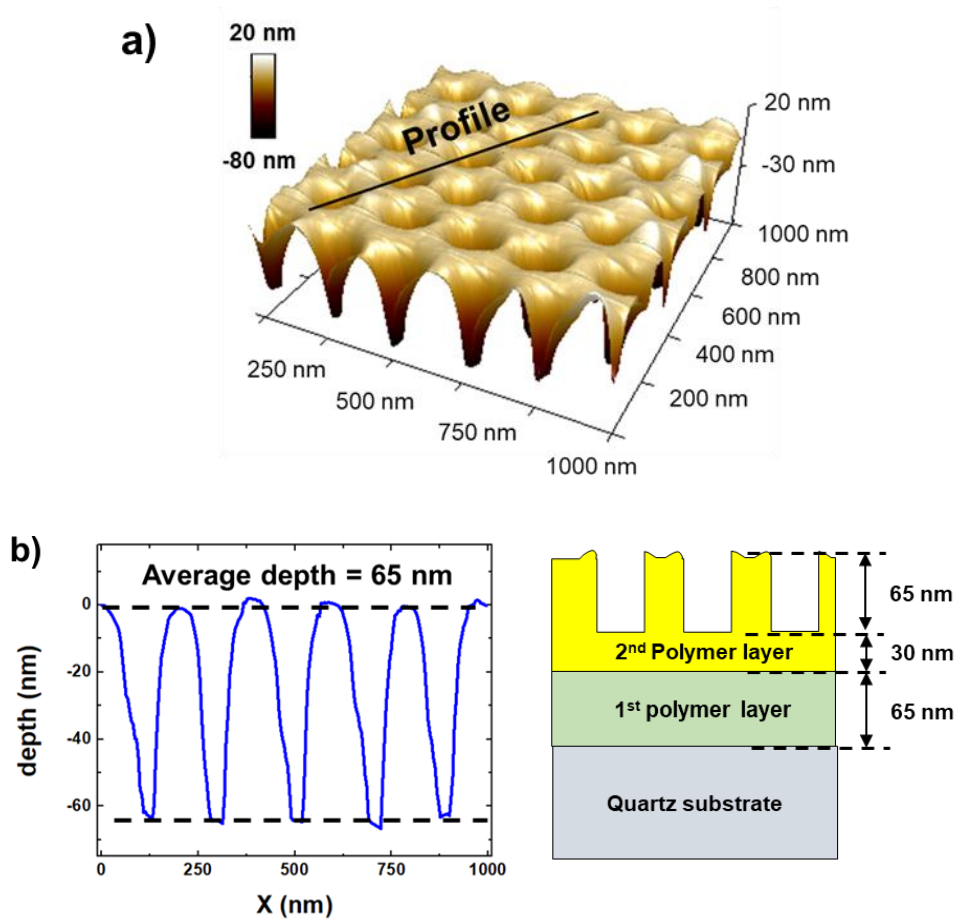


Figure 2.5 Depth profiles for nanoimprinted polymer surface a) 3D AFM image and b) depth profile result of patterned polymer layer after nanoimprint process.

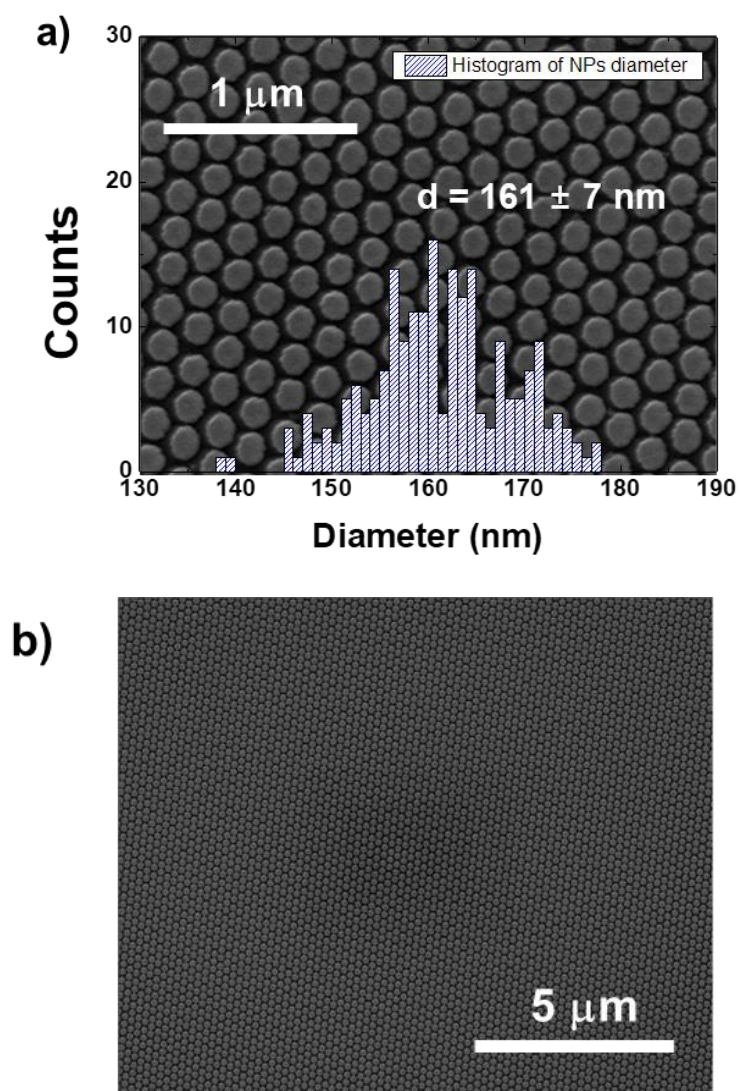


Figure 2.6 Nanoparticle arrays fabricated by nanoimprint lithography, a) SEM images with magnification x50,000, b) SEM image with magnification x10,000.

Table 2.1 Calculated deposition thickness for PdAu Compositions of various weight ratio.

| NO. | Weight ratio (wt%) | | Volume ratio (vol%) | | Calculated deposition thickness (nm) | | |
|-----|--------------------|-----|---------------------|-----|--------------------------------------|------|------|
| | Pd | Au | Pd | Au | Ti | Pd | Au |
| 1 | 100 | 0 | 100 | 0 | 5 | 25 | 0 |
| 2 | 90 | 10 | 93 | 7 | 5 | 23.4 | 1.6 |
| 3 | 80 | 20 | 86 | 14 | 5 | 21.6 | 3.4 |
| 4 | 70 | 30 | 79 | 21 | 5 | 19.7 | 5.3 |
| 5 | 60 | 40 | 70 | 30 | 5 | 17.6 | 7.4 |
| 6 | 50 | 50 | 61 | 39 | 5 | 15.3 | 9.7 |
| 7 | 40 | 60 | 51 | 49 | 5 | 12.9 | 12.1 |
| 8 | 30 | 70 | 40 | 60 | 5 | 10.1 | 14.9 |
| 9 | 20 | 80 | 28 | 72 | 5 | 7.1 | 17.9 |
| 10 | 10 | 90 | 15 | 85 | 5 | 3.7 | 21.3 |
| 11 | 0 | 100 | 0 | 100 | 5 | 0.0 | 25.0 |

2.3.2. Characterization of PdAu Nanoparticle Arrays by Composition

Figure 2.7 shows an SEM image annealed at 600 °C of particles fabricated with the composition shown in Table 2.1. The average diameters of Pd nanoparticles and Au nanoparticles were analyzed to be 164 ± 7 nm and 154 ± 8 nm, respectively. Also, the average diameter of the 9 samples in which the Au content of PdAu increased by 10% was 149 ± 7 nm, 142 ± 9 nm, 151 ± 8 nm, 145 ± 9 nm, 149 ± 8 nm, 141 ± 11 nm, 143 ± 14 nm, 143 ± 7 nm and 154 ± 8 nm, respectively. It was observed that the diameter of the sample to which Au was added was decreased compared to the Pd only composition. This appears to be because the diameter decreases as Au diffuses into Pd. It was observed that there was no difference in the morphology of the surface of nanoparticles of various compositions.

The results of XRD analysis for various PdAu compositions were shown in Figure 2.8. As a result of 2-theta analysis at 20° to 90°, 111 and 222 peaks were observed for various compositions. The detailed observation results for the 111 peaks of various PdAu compositions were shown in Figure 2.8b. The 111 plane peaks of Pd and Au were measured to be 38.178° and 40.108°, respectively. It was confirmed that these results are consistent with previous results [13]. As the Au mass ratio increased, it was observed that the 111 peak values decreased constantly, and the 2-theta values of 111 peaks were

summarized in Figure 2.8c. By comparing the 2-theta 111 peak value of any PdAu composition with the data value in Figure 2.8c, its PdAu composition can be inferred. Figure 2.8c summarizes the 111 d-spacing and lattice parameters calculated from the 2theta values of the 111 peaks.

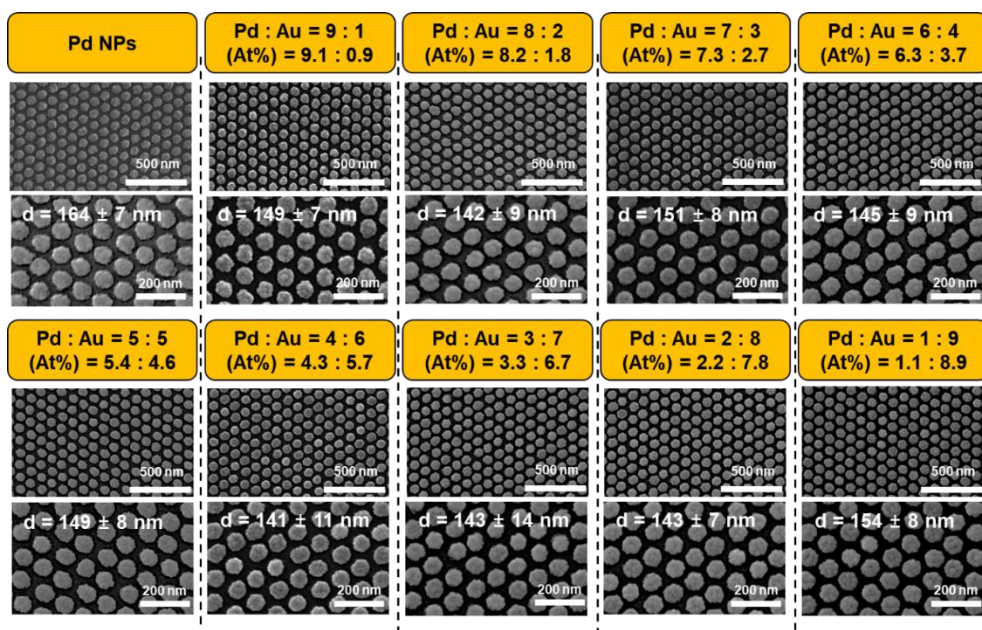


Figure 2.7 SEM images of various PdAu compositions annealed at 600 °C.

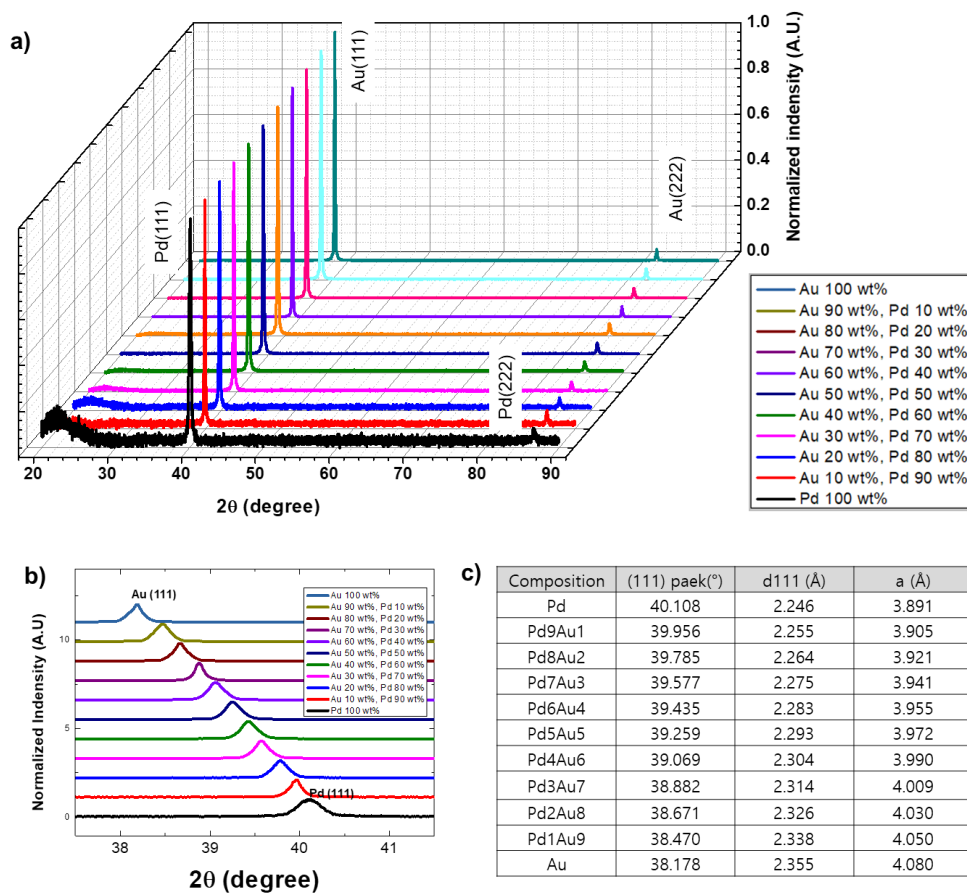


Figure 2.8 XRD results of various PdAu composition, a) 2θ results from 20° to 90°, b) 111 plane peaks of various PdAu composition, c) Table summarizing the measured 111 peak, the calculated 111 d-spacing and the calculated lattice parameter.

2.3.3. Characterization of Pd₇Au₃ nanoparticle arrays according to various annealing temperatures

The characteristics of the Pd₇Au₃ composition according to various annealing temperature were investigated. Nanoimprint lithography was used to fabricate nanoparticle arrays with a mass ratio of Pd₇Au₃. The thickness of the metal deposited by the e-beam evaporator was Ti 5 nm / Pd 19.7 nm / Au 5.3 nm. To determine the effect of annealing temperature on hydrogen measurement performance, samples annealed at 400 °C, 500 °C, 600 °C, 700 °C and 800 °C were prepared. SEM and AFM images of the Pd₇Au₃ composition annealed at various temperatures were shown in Figure 2.9. The average heights of the 400 °C, 500 °C, 600 °C, 700 °C and 800 °C samples were 28.8 nm, 31.2 nm, 32.3 nm, 41.2 nm, and 44.8 nm, respectively. There was no difference in the average height until the annealing temperature was 600 °C. When the annealing temperature exceeded 700 °C, the shape of the particles became uneven, and large grains were found. It was also observed that the particle diameter decreased while the particle height increased. It can be seen that at an annealing temperature of 700 °C, the Pd and Au elements obtained sufficient energy to change the shape of the nanoparticles.

The results of XRD analysis at various annealing temperatures were shown in Figure 2.10. As a result of 2-theta analysis at 20° to 90°, only PdAu 111 peak and PdAu 222 peak were observed. The results in which only the

111 and 222 peaks were observed in the XRD analysis of nanoparticles can be confirmed in other papers [10]. The 2-theta values of PdAu 111 and 222 peaks were analyzed at 39.9° and 86.2°, respectively. The change of the PdAu 111 peak according to the annealing temperature was shown in Figure 2.10b. In addition, to observe the orientation in the in-plane direction, rocking curves were measured for various annealing temperature samples, and the results are shown in Figure 2.10c. The calculated full-width half-maximum (FWHM) of the 2-theta and rocking curves were summarized in Figure 2.10d. Observing the results of 2-theta, the FWHM value decreases as the annealing temperature increases. This is a natural result because as atoms move more freely as the temperature rises, the arrangement is in long range order, and small grains coalesce to form large grains. On the other hand, when observing the results of the rocking curve, it was investigated that the FWHM value decreased up to 600 °C. and then increased again at 700°C. The cause of this result can be interpreted as a result that the orientation in the in-plane direction is rather decreased as the height of the nanoparticles increases.

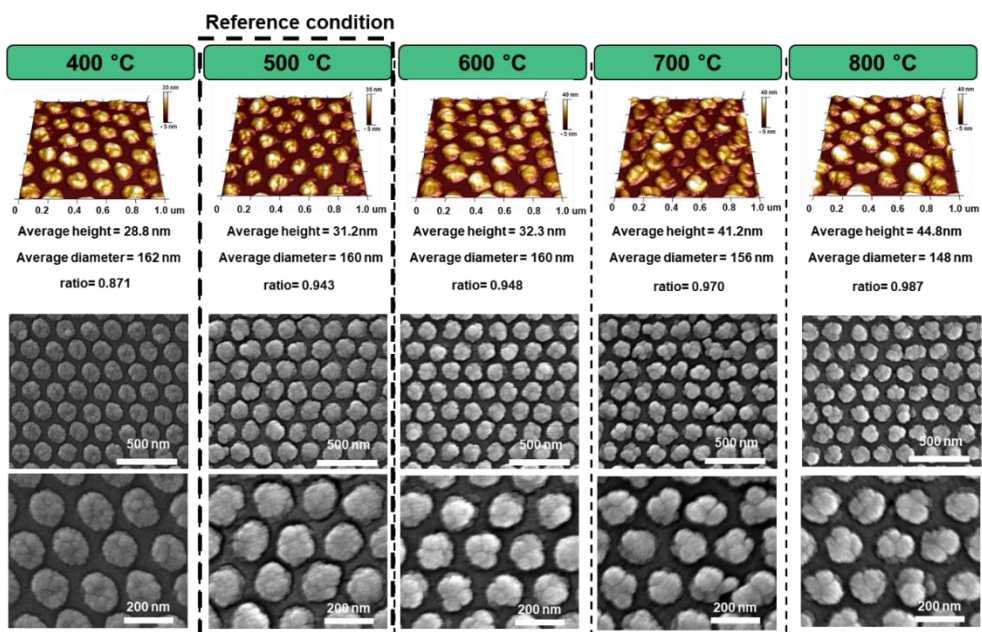


Figure 2.9 SEM and AFM images of annealed Pd₇Au₃ samples at various annealing temperatures

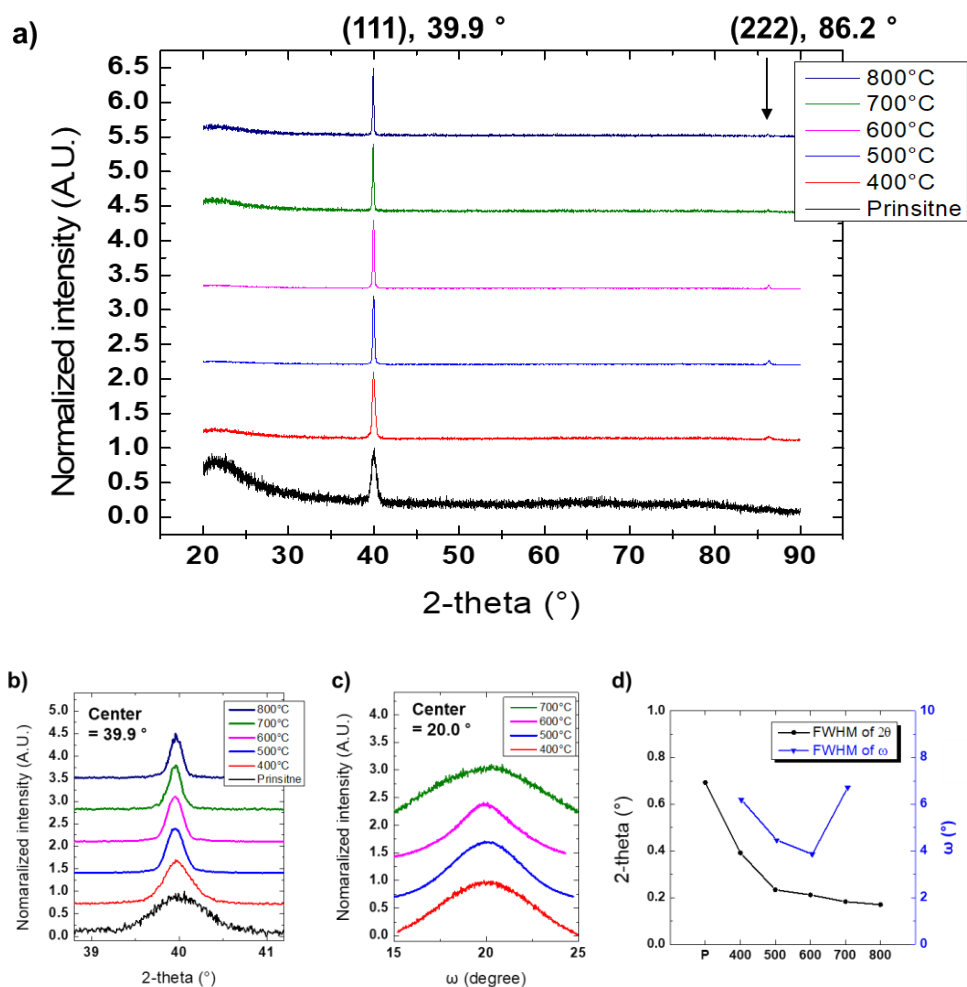


Figure 2.10 XRD results of various annealing temperature, a) 2theta results from 20° to 90°, b) XRD peaks of PdAu 111 plane, c) Rocking curve of PdAu 111 plane, d) FWHM of 2-theta and rocking curve of PdAu 111 plane

The high-resolution XPS spectrum for various annealing temperatures was shown in Figure 2.11. The photoelectron line of Au 4f consist of Au 4f_{5/2} and Au 4f_{7/2}. The Pd 3d photoelectron line was more complex than that of Au 4f. Basically, the photoelectron line of Pd 3d consisted of two peaks, Pd 3d_{3/2} and Pd 3d_{5/2}. In the presence of Pd oxidation, two additional peaks were observed: PdO 3d_{5/2} and PdO 3d_{3/2}. Also, when Pd and Au are alloyed, Pd 3d_{5/2} and Au 4d_{5/2} overlap. Therefore, the deconvoluted photoelectron lines of Pd 3d consisted of Pd 3d_{3/2}, Pd 3d_{5/2}, PdO PdO 3d_{3/2}, 3d_{5/2} and Au 4d_{5/2}.

The binding energy analyzed from the deconvoluted XPS spectra were summarized in Table 2.2. The binding energies of Pd 3d_{5/2}(334.1 eV) and Pd 3d_{3/2} (339.7 eV) were observed to be slightly decreased compared to those of Pd 3d_{5/2}(335.2 eV) and Pd 3d_{3/2} (340.5 eV) in polycrystalline bulk Pd [14]. Also, in the case of gold, the binding energies of Au 3f_{5/2}(86.3 eV) and Au 3f_{7/2} (82.6 eV) were observed to be slightly decreased compared to those of Pd Au 3f_{5/2}(87.96 eV) and Au 3f_{7/2} (84.22 eV) in bulk gold [15]. The binding energy reduction of Pd 3d peak and Au 4f peka by alloying was consistent with the results reported in previous papers [15,16]. The PdO 3d_{5/2} peak located at a binding energy of 336.3 eV was related to palladium oxide, confirming that it is a result of PdO [17] rather than PdO₂ [18]. On the other hand, it was confirmed that the other PdO 3d_{3/2} peak of 342.1 eV corresponds to PdOx whose stoichiometry is not specified [19]. Table 2.2 shows the composition of PdAu, and the ratio of oxides obtained from XPS data. The calculated atomic percentage of Pd7Au3 was 81.2 to 18.8. At annealing

temperatures of 400 °C, 500 °C, 600 °C and 700 °C, the weight composition ratio of PdAu was calculated to be 62.7: 37.3, 57.3: 42.7, 59.1: 40.9, 31.3: 68.7, respectively. It was observed that the Pd content was lower than the calculated weight composition of PdAu at all annealing temperatures. In general, when vacuum annealing a PdAu alloy, more Au is collected on the surface due to the surface segregation effect [20,21]. The surface segregation effect can be changed depending on the annealing atmosphere and temperature. Hydrogen is known to have the effect of bringing palladium to the surface during annealing of PdAu alloys [22-24]. When annealing in vacuum, the atomic composition of PdAu is 8:2 in bulk, but the composition of the surface is very different, about 3.5:6.5 [21]. However, when the heat treatment is performed in an Ar atmosphere containing 4% hydrogen, it can be confirmed that the Pd content is higher than this. This means that the annealing conditions in Ar atmosphere containing 4% H₂ led the Pd atoms to the surface. Since Au has a strong tendency to go to the surface with increasing temperature, it was confirmed that the Au content increased at an annealing temperature of 700 °C. And it was also confirmed that Pd came out to the surface under the influence of 4% of hydrogen before the annealing temperature of 600 °C. In addition, it was observed that as the annealing temperature increased, the oxidation of palladium also increased. The effect of surface composition on the hydrogen measurement will be discussed later.

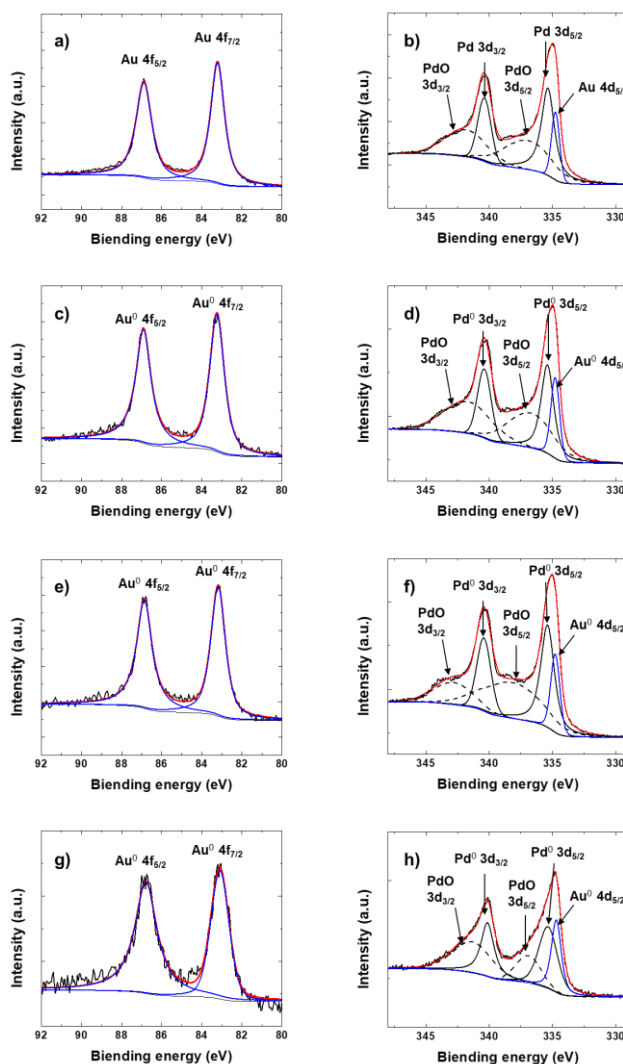


Figure 2.11 High-resolution XPS spectra for various annealing temperatures of PdAu nanoparticle arrays, a) Au 4f and b) Pd 3d spectra annealed at 400 °C, c) Au 4f and d) Pd 3d spectra annealed at 500 °C, e) Au 4f and f) Pd 3d spectra annealed at 600 °C and g) Au 4f and h) Pd 3d spectra annealed at 700 °C

Table 2.2 Binding energy, composition and oxide ratio of PdAu nanoparticle arrays analyzed by XPS results

| Annealing Temperature | Binding energy (eV) | | | | | | | Alloy composition Wt% (At%) | | Ratio |
|-----------------------|-----------------------|-----------------------------------|-----------------------|-----------------------------------|-----------------------------------|-----------------------------------|-----------------------------------|-----------------------------|------------------|-------|
| | PdO 3d _{3/2} | Pd ⁰ 3d _{3/2} | PdO 3d _{5/2} | Pd ⁰ 3d _{5/2} | Au ⁰ 4d _{5/2} | Au ⁰ 4f _{5/2} | Au ⁰ 4f _{7/2} | Pd | Au | |
| 400 | 341.3 | 339.8 | 336.5 | 334.8 | 334.2 | 86.3 | 82.6 | 62.7% (76.0%) | 37.3% (24.0%) | 0.91 |
| 500 | 341.2 | 339.7 | 336.3 | 334.8 | 334.1 | 86.2 | 82.5 | 57.3% (71.7%) | 42.7% (28.3%) | 1.08 |
| 600 | 342.1 | 339.7 | 337.5 | 334.7 | 334.1 | 86.2 | 82.5 | 59.1% (73.1%) | 40.9% (26.9%) | 1.02 |
| 700 | 340.8 | 339.7 | 336.2 | 335.0 | 334.3 | 86.4 | 82.7 | 31.3% (46.2%) | 68.7% (53.8%) | 1.60 |

The detailed analysis result of Pd₇Au₃ composition by TEM was shown in Figure 2.12. By depositing PMMA as a sacrificial layer on the surface of the nanoparticles, a sample was prepared so that TEM analysis could be performed smoothly. Several grains in the nanoparticles were identified on the TEM image, and it was observed that one nanoparticle was polycrystalline. This may be contrary to the XRD data, but in practice it can be determined that the intensity of the other plane is not sufficient to measure. In other papers [10], only 111 and 222 PdAu peaks were observed in XRD, but in EBSD analysis, it was analyzed that there were 2-3 grains in one nanoparticle. Also, the grain of nanoparticles was observed through SEAD pattern analysis. The zone axis of the analyzed SAED pattern was 101 direction, and 111 d-spacing could be obtained through this. As a result of measuring the d-spacing value of the 111 plane through high resolution TEM, it was analyzed as 2.29 Å. There was a difference of about 0.7% from 2.275 Å calculated as the 111 peak value of XRD. The composition analysis result of a single nanoparticle through EDS was shown in Figure 2.12d. Through the EDS mapping image of Ti, it can be confirmed that most of the Ti elements were located under the nanoparticles. Also, through the EDS mapping data of Pd and Au, it can be confirmed that Pd and Au were evenly distributed in the nanoparticle. It was found that, in alloying through annealing, Pd and Au were alloyed, but Ti remained as a buffer layer. The

mass ratio measured by EDS was 68: 32 for Pd: Au, which was very similar to the 70:30 mass ratio applied when depositing metals.

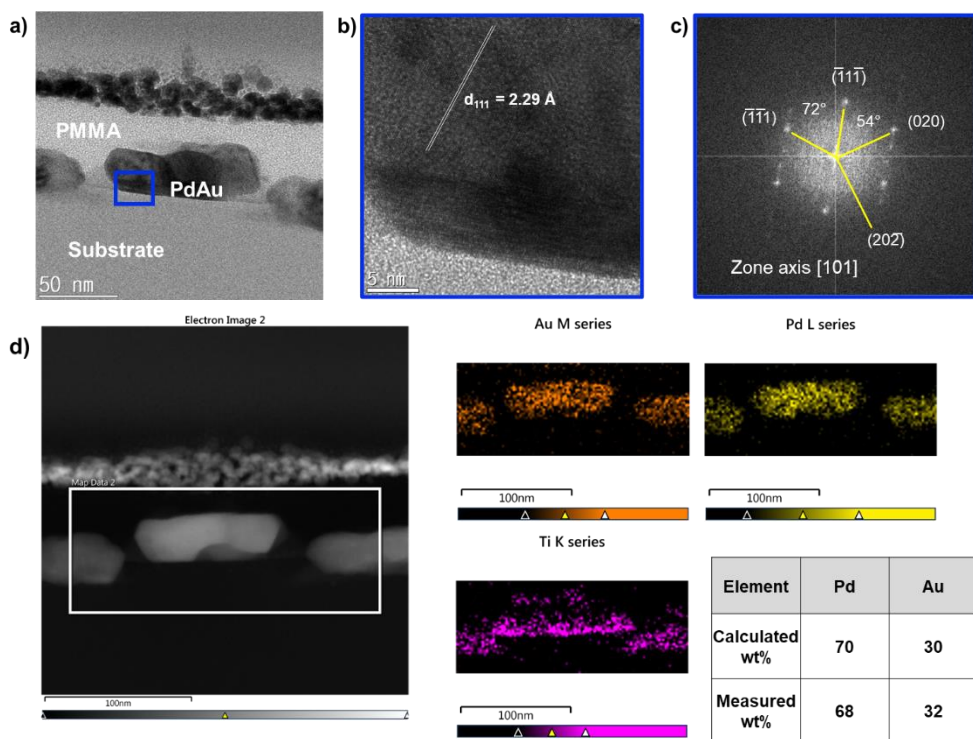


Figure 2.12 TEM analysis of annealed Pd₇Au₃ samples, a) TEM images of annealed Pd₇Au₃ samples, b) high-resolution TEM image of annealed Pd₇Au₃ sample, c) SAED pattern of annealed Pd₇Au₃ sample, d) EDX annealed Pd₇Au₃ sample

2.4. Summary

In this chapter, it was demonstrated that the fabrication of a PdAu nanoparticle arrays using nanoimprint lithography instead of the conventionally used nanosphere lithography for LSPR-based hydrogen sensor. Conventional nanosphere lithography has random and low reproducibility, whereas nanoimprint lithography enables the iterative and efficient fabrication of nanoparticle arrays. XRD data were obtained at a 10% composition interval of the fabricated PdAu nanoparticle array, and it is likely that an arbitrary PdAu composition can be inferred from this. It was confirmed that the surface composition changes according to the annealing temperature, and we will investigate how this composition change affects hydrogen measurement in Chapter 5.

2.5. Bibliography

- [1] L.J. Guo, "Nanoimprint lithography: methods and material requirements." *Advanced materials*, 19.4, (2007), 495-513.
- [2] H. Lan, and H. Liu, "UV-nanoimprint lithography: structure, materials and fabrication of flexible molds." *Journal of nanoscience and nanotechnology*, 13.5, (2013), 3145-3172.
- [3] K.Y. Yang, K.M. Yoon, S. Lim and H. Lee, "Direct indium tin oxide patterning using thermal nanoimprint lithography for highly efficient optoelectronic devices." *Journal of Vacuum Science & Technology B: Microelectronics and Nanometer Structures Processing, Measurement, and Phenomena*, 27.6, (2009), 2786-2789.
- [4] S. W. Lee, K. S. Lee, J. Ahn, J.J. Lee, M.G. Kim and Y.B. Shin, "Highly sensitive biosensing using arrays of plasmonic Au nanodisks realized by nanoimprint lithography." *ACS nano*, 5.2, (2011), 897-904.
- [5] C. Langhammer, I. Zorić, B. Kasemo and B.M. Clemens, "Hydrogen storage in Pd nanodisks characterized with a novel nanoplasmonic sensing scheme." *Nano Letters*, 7.10, (2007), 3122-3127.
- [6] C. Langhammer, V.P. Zhdanov, I. Zorić and B. Kasemo, "Size-dependent kinetics of hydriding and dehydriding of Pd nanoparticles." *Physical review letters*, 104.13, (2010), 135502.
- [7] C. Wadell, F. A. A. Nugroho, E. Lidstrom, B. Iandolo, J.B. Wagner and C. Langhammer, "Hysteresis-free nanoplasmonic Pd–Au alloy hydrogen sensors." *Nano letters*, 15.5, (2015), 3563-3570.
- [8] S. Syrenova, C. Wadell, F.A. Nugroho, T.A. Gschneidtnr, Y.A. Diaz

- Fernandez, G. Nalin and C. Langhammer, "Hydride formation thermodynamics and hysteresis in individual Pd nanocrystals with different size and shape." *Nature materials*, 14.12, (2015), 1236-1244.
- [9] F. A. A. Nugroho, I. Darmadi, V.P. Zhdanov and C. Langhammer, "Universal scaling and design rules of hydrogen-induced optical properties in Pd and Pd-Alloy nanoparticles." *ACS nano*, 12.10, (2018), 9903-9912.
- [10] F.A. Nugroho, I. Darmadi, L. Cusinato, A. Susarrey-Arce, H. Schreuders, L.J. Bannenberg and C. Langhammer, "Metal-polymer hybrid nanomaterials for plasmonic ultrafast hydrogen detection." *Nature materials*, 18.5, (2019), 489-495.
- [11] P. Colson, C. Henrist and R. Cloots, "Nanosphere lithography: a powerful method for the controlled manufacturing of nanomaterials." *Journal of Nanomaterials*, 2013, (2013).
- [12] F.A. Nugroho, B. Iandolo, J.B. Wagner and C. Langhammer, "Bottom-up nanofabrication of supported noble metal alloy nanoparticle arrays for plasmonics." *ACS nano*, 10.2 (2016), 2871-2879.
- [13] H.E. Swanson, and E. Tatge, "US Nat. Bur. Stand." Circular, 539, (1953).
- [14] M.C. Militello and S.J. Simko, "Elemental palladium by XPS." *Surface Science Spectra*, 3.4, (1994), 387-394.
- [15] X. Zhu, Q. Guo, Y. Sun, S. Chen, J.Q. Wang, M. Wu and Y. Wan, "Optimising surface d charge of AuPd nanoalloy catalysts for enhanced catalytic activity." *Nature communications*, 10.1 (2019), 1-11.

- [16] P.A.P. Nascente, S.G.C. de Castro, R. Landers and G.G. Kleiman, "X-ray photoemission and Auger energy shifts in some gold-palladium alloys." *Physical Review B*, 43.6, (1991), 4659.
- [17] M.C. Militello and S.J. Simko, "Palladium oxide (PdO) by XPS." *Surface Science Spectra*, 3.4 (1994), 395-401.
- [18] K.S. Kim, A.F. Grossmann and N. Winograd, "X-ray photoelectron spectroscopic studies of palladium oxides and the palladium-oxygen electrode." *Analytical Chemistry*, 46.2, (1974), 197-200.
- [19] W.E. Moddeman, W.C. Bowling, D.C. Carter and D.R. Grove, "XPS surface and bulk studies of heat treated palladium in the presence of hydrogen at 150° C." *Surface and Interface Analysis*, 11.6-7, (1988), 317-326.
- [20] O.M. Løvvik, "Surface segregation in palladium based alloys from density-functional calculations." *Surface Science*, 583.1, (2005), 100-106.
- [21] M. Zhao, W.G. Sloof and A.J. Böttger, "Modelling of surface segregation for palladium alloys in vacuum and gas environments." *International Journal of Hydrogen Energy*, 43.4, (2018), 2212-2223.
- [22] P. Ekborg-Tanner and P. Erhart, "Hydrogen-Driven Surface Segregation in Pd Alloys from Atomic-Scale Simulations." *The Journal of Physical Chemistry C* 125.31 (2021): 17248-17260.
- [23] T.V. de Bocarmé, M. Moors, N. Kruse, I.S. Atanasov, M. Hou, A. Cerezo and G.D. Smith, "Surface segregation of Au–Pd alloys in UHV and reactive environments: Quantification by a catalytic atom probe." *Ultramicroscopy*, 109.5, (2009), 619-624.
- [24] H. Guesmi, "Theoretical insights on the effect of reactive gas on the

chemical ordering of gold-based alloys." *Gold Bulletin*, 46.4, (2013), 213-219.

Chapter 3. Study on the fabrication of plasmonic nanoparticle arrays using nanotip indentation lithography

3.1. Introduction

The localized surface plasmon resonance of nanoparticles has different properties depending on the shape [1-4], size [5-8], and material [9,10] of the nanoparticles. The nanodisk shape of Pd alloy was generally used for LSPR based hydrogen sensor, and when the material was determined, characteristic change has been observed mainly through the various diameter of nanodisk [11-13].

Nanoimprint lithography has great advantages in terms of high throughput and low process cost but changing the diameter of nanoparticles requires the use of new nanoimprint mold. For imprint molds with nanopatterns of 200 nm or less, they should be fabricated through electron beam lithography. A considerable amount of money was required to purchase such a nano-patterned mold and additional research costs may be spent for patterns of 100 nm or less. Therefore, nanoimprint lithography is

economically very inefficient if various sizes have to be adjusted to find the optimal conditions.

When nanodisk patterns of various diameters are required, nanotip indentation lithography is a more powerful solution than any other lithography method. Nanotip indentation lithography is a lithography method that can efficiently adjust the diameter without additional cost to change the diameter while requiring as low processing cost as nanoimprint lithography. In addition, nanoindentation lithography is relatively easy to process compared to electron beam lithography and can control the diameter more accurately than nanosphere lithography.

In this chapter, the fabrication of nanoparticles of various diameters using nanotip indentation lithography was demonstrated. In nanoindentation lithography, the influence of three factors affecting the diameter of nanoparticles (nanotip, reactive ion etching process, and wet etching process) was investigated. By optimizing each process, it was demonstrated that the diameter of nanoparticles can be changed from 58.6 nm to 132.7 nm through nanotip indentation lithography. In addition, three samples were prepared for optical hydrogen measurement and the compositional characteristics of the prepared samples were analyzed through XRD analysis.

3.2. Experimental details

3.2.1. Nanoparticle array fabrication process using nanotip indentation lithography

A schematic diagram of the nanotip indentation process in nanotip indentation lithography was shown in Figure 3.1. There are five parameters that apply to the indentation process (the spring constant of the cantilever (K), the deflection sensitivity of the photodetector (S), the measured deflection, the deflection, and the applied force) [14-17]. To quantify the indentation process, it is necessary to obtain the correlation of the indentation depth according to the applied force. The indentation depth can be obtained through depth measurement of AFM, and the applied force can be obtained through the above-mentioned 4 parameters. The deflection sensitivity of the photodetector is built into the AFM unit. After aligning the light reflected through the gold mirror on the top of the cantilever to the center of the photodetector, the tip is bent during the press-fitting process to change the position of the incident light of the photodetector. At this time, measured deflection can be obtained from the changed position, and deflection can be obtained through deflection sensitivity and measured deflection. Also, the applied force can be calculated as the product of the deflection obtained and the spring constant of the cantilever. Since the indentation depth can be measured by measuring the depth profile after indentation, the indentation

process can be quantified by obtaining the applied force and the indentation depth.

Process flow of a nanoparticle array fabrication using nanotip indentation lithography was shown in Figure 3.2. First, a 2 cm x 2 cm quartz substrate (Korea Science) was cleaned using acetone and IPA. The first polymer layer, PMGI SF5 or SF3, was spin-coated on a quartz substrate, and the substrate was baked on a hot plate at 200°C for 5 min. After 5 minutes of natural air cooling, the 2nd polymer layer, MR-I 8010r, was spin-coated on a quartz substrate and the substrate was baked on a hot plate at 100°C for 1 min. A desired hole pattern was formed on the surface of the 2nd polymer through the indentation process using AFM. The AD-40-AS tip, an AFM tip used for nanotip indentation lithography, has the specifications of a sharp conductive single crystal diamond probe, $k = 40 \text{ N/m}$, Length = 225 μm , and 10 nm ROC. The appropriate depth of indentation was determined by controlling the applied force, and the coordinates were set to form a hexagonal pattern to form a pattern on the 2nd polymer surface. Thereafter, the 1st polymer layer was exposed by etching the 2nd polymer layer under reactive ion etching conditions of 70 mtorr, Ar 6sccm, O₂ 10sccm, and Power 20W. Then, the substrate was wet etched using AZ MIF 300 developer. After cleaning with DI water and drying the hot plate at 60°C, Ti/Pd/Au was deposited on the substrate using an e-beam evaporator. To lift off the deposited substrate, the substrate was washed with acetone, AZ MIF 300

developer, and IPA in that order. Afterwards, to make PdAu alloy, annealing process was performed at 600°C for 12 hours in an ambient atmosphere containing 4% hydrogen in argon.

Nanotip indentation and nanoimprint lithography have similar processes except for making hole patterns. However, while nanoimprint lithography only needs to find one optimal condition for one mold, nanotip indentation lithography requires optimization because various conditions can exist even for making one nanopattern.

3.2.2. Process optimization of nanoparticle fabrication using nanotip indentation lithography

To easily generate the desired diameter in nanotip indentation lithography, it is necessary to know how each process affects the nanoparticle diameter. There are three major processes that affect the diameter of nanoparticles. The first is the indentation process, the second is reactive ion etching and the last is the wet etching process. To find out the influence of each process, the diameter change of the nano hole pattern was observed through AFM measurement before and after the process, and how the diameter changes according to the process parameters was confirmed. In addition, changes with the condition parameters of each process, which are not directly related but can have an indirect effect, were also observed. First, the thickness of the polymer layer according to the spin coating material and

parameters were observed. Second, the power of reactive ion etching and the etching rate and surface roughness according to time were observed. Finally, the yield of nanoparticles according to the wet etching time was investigated.

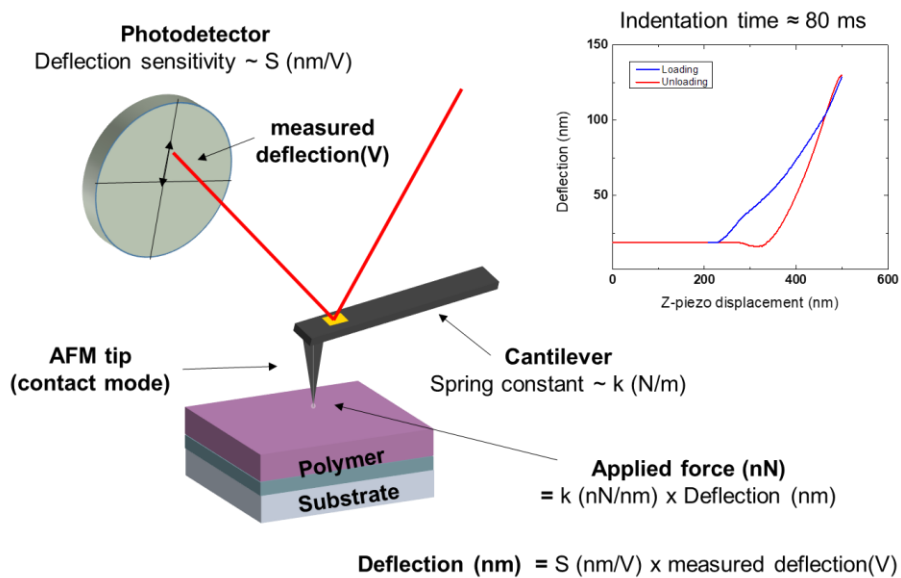
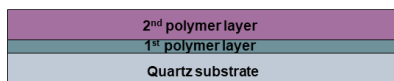
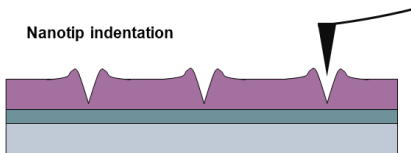


Figure 3.1 Schematic diagram of indentation process

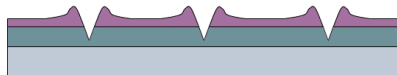
1. Polymer spin coating on quartz substrate (20 x 20 mm²)
1st layer : PMGI SF5 or SF3
2nd layer : MR-I 8020r or 8010r



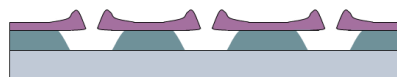
2. Nanotip indentation



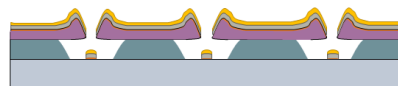
3. Reactive ion etching (RIE)



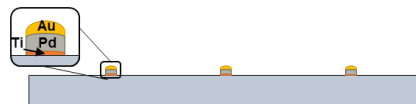
4. Polymer etching using AZ MIF 300 developer



5. Metal(Ti/Pd/Au) deposition with e-beam evaporator



6. Polymer removal with acetone and AZ MIF 300



7. Annealing for alloying



Figure 3.2 Process flow of nanotip indentation lithography

3.3. Results and discussions

3.3.1. Control parameters and controlled results of each nano indentation lithography process

First, in the spin coating process for stacking the 1st polymer layer and the 2nd polymer layer, the thickness of the polymer according to RPM and the coating material was confirmed. The RPMs used for spin coating were 2000 RPM, 3000 RPM, and 5000 RPM. The thickness according to RPM of PMGI SF3 for 1st polymer layer was 90.2 nm, 73.4 nm and 61.6 nm, respectively. The reason for controlling the thickness of the 1st polymer layer is that the thinner the 1st polymer layer should be used as the pitch decreases. The thicknesses according to RPM of MR-I 8020r for the 2nd polymer layer were 210.3 nm, 186.0 nm and 146.0 nm. In the case of 8010r, the thicknesses according to RPM were 109.0 nm, 91.0 nm, and 73.6 nm. The reason for controlling the thickness of the 2nd polymer layer is that reactive ion etching of the 2nd polymer exposes the 1st polymer layer, and the diameter of the nanoparticles changes according to the etching thickness. A smooth process can only be achieved by selecting an appropriate secondary polymer thickness in consideration of the desired diameter size.

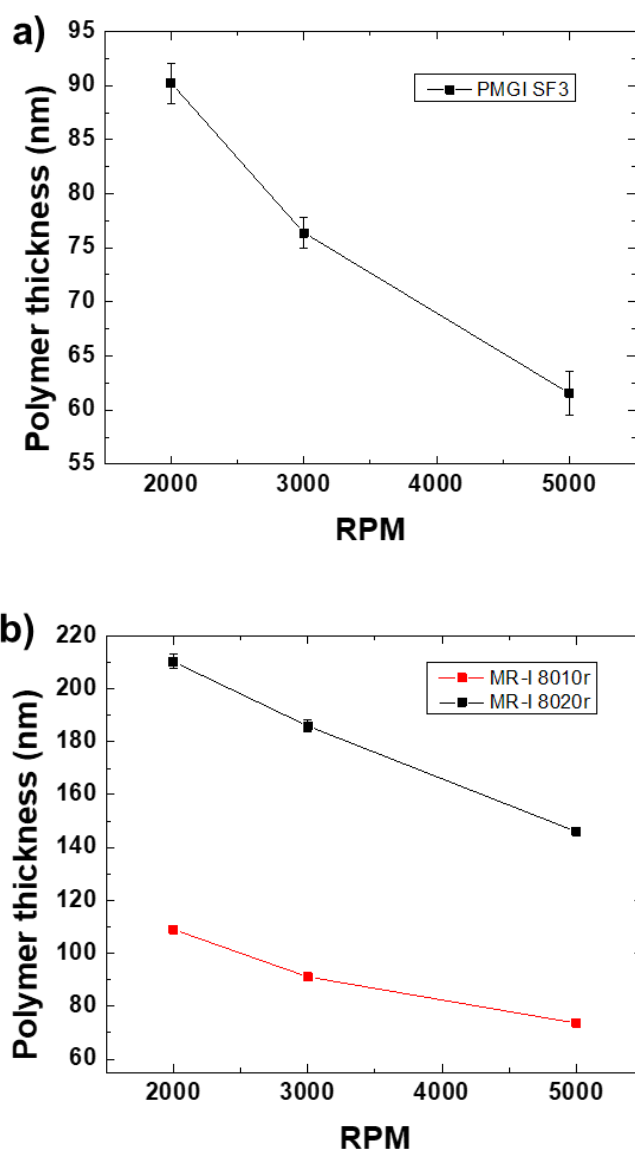


Figure 3.3 Polymer thickness measurement result according to spin coating material and RPM, a) PMGI SF3 for 1st polymer layer and b) MR-I 8010r and 8020r for 2nd polymer layer.

Second, the relationship between etch rate and surface roughness according to the RF power and etching time of reactive ion etching was confirmed. For etching, 91.0 nm of SF3 as a 1st polymer and 220 nm of MR-I 8020r as a 2nd polymer were deposited on a quartz substrate. To obtain the etch rate, in the case of RF power of 35 W, the etching depth was measured by changing the etching time to 5 sec, 10 sec, 20 sec, 50 sec and 100 sec. In the case of RF power of 20W, the etch depth was measured by changing the etching time to 10 sec, 20 sec, 40 sec, 100 sec and 120 sec. The etch rates measured at RF power of 20 W and 35 W were 1.08 nm/s and 1.97 nm/s, respectively. The effect of decreasing the etch rate as the etch time increased during the etch process was not observed. Also, the same result was obtained when the experiment was conducted by changing the 2nd polymer to MR-I 8010r. And it was confirmed that the surface roughness is affected more by the etch depth than the RF power, and the roughness according to the etch depth was shown in Figure 3.4b. Since the surface RMS roughness increases as the etching increases, it is judged that this surface roughness can affect the hole pattern. Therefore, it seems that setting the etching depth as small as possible will soften the shape of the particle edge.

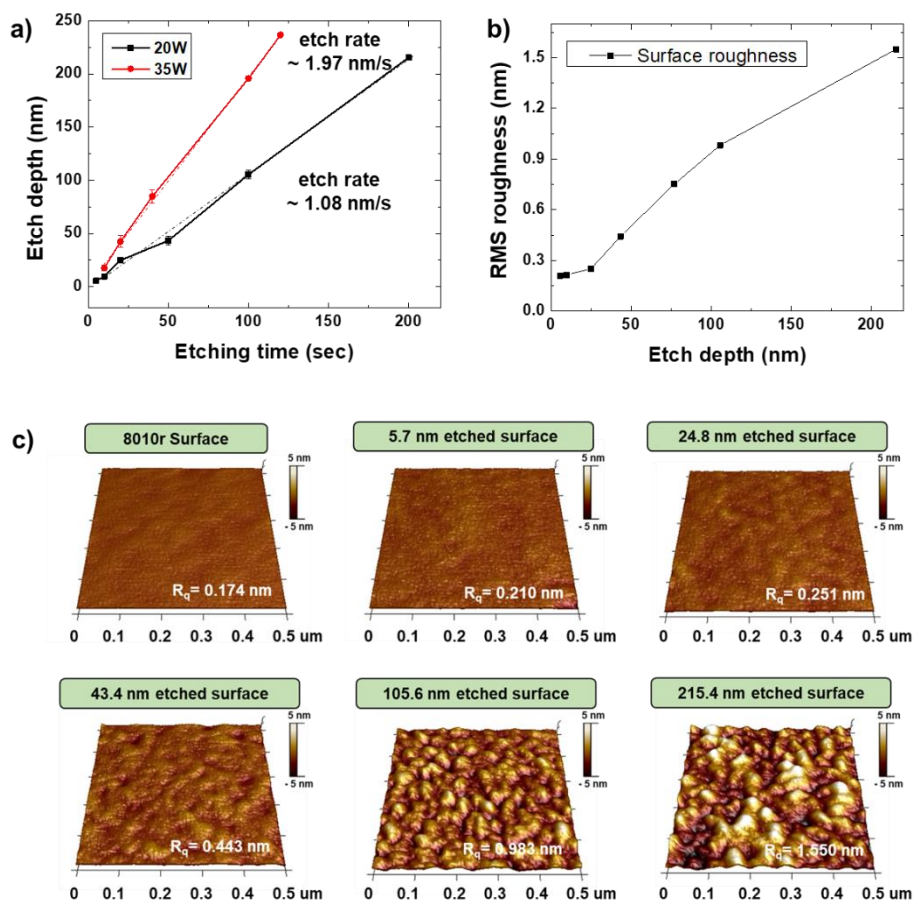


Figure 3.4 AFM measurement results of etch depth, etch rate, and surface roughness according to etching time and RF power of reactive ion etching, a) Etch depth measurement results according to RF power and etching time, b) Surface roughness measurement results according to etch depth, c) 3D AFM images of the MR-I 8020r surface for various etch depths

Third, the relationship between the yield of nanoparticles according to wet etching time was investigated. To measure the yield according to the wet etching time, PMGI SF5 with a thickness of 215 nm and MR-I 8010r with a thickness of 137 nm were deposited on quartz substrates as the 1st and 2nd polymers. After making a hole pattern by indentation of 76.6 nm, samples were prepared by reactive ion etching of 96 nm. Wet etching was performed with various etching times and the yield was checked by SEM after Ti/Au deposition.

In the case of wet etching time of 13 sec, hole patterns were observed in the dark field optical microscopy (OM) image, but the yield of nanoparticles after metal deposition was 0%. However, in the case of a wet etching time of 13 seconds, it was observed that a yield of 100% was obtained. This appears to be the result of metal peeling off because PMGI polymer of several nanometers remained after the wet etching process. Although there is a difference of 2 seconds, a yield of 100% was obtained at the wet etching time of 15 seconds, so the 0% yield of 13 seconds is evidence of the effect by the residual polymer. The yield of nanoparticles was 100% from the wet etching time of 15 sec to 28 sec, but it was observed that the yield decreased after 28 sec. And after the wet etching time of 35 sec, it can be observed that the yield of nanoparticle was 0%. The reason that the yield decreases as the wet etching time increases is that the 1st polymer is completely wet-etched, and the 2nd polymer is not supported, and the polymer pattern is collapsed. The reason why the dark field optical microscope image appears even after the

polymer pattern collapses is that even when the secondary polymer collapses and is attached to the quartz substrate, the hole pattern does not collapse, so scattered light is generated at the edge of the hole. Therefore, it is difficult to determine collapse only with dark field optical microscopy image, and actual yield must be confirmed through metal deposition. Wet etch time is also affected by the pitch of the nanoparticles. A tight wet etch time window must be established to produce a small pitch nanoparticle array.

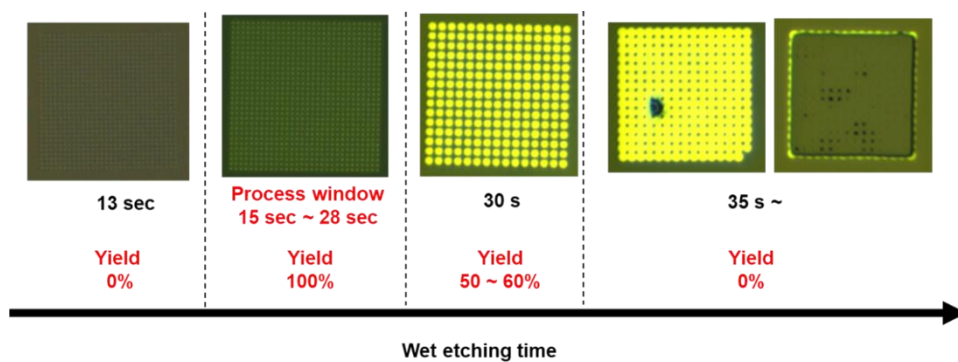


Figure 3.5 Dark field optical microscopy images at various wet etch times.

3.3.2. Factors determining the diameter of nanoparticles in nanotip indentation lithography

As mentioned above, there are three factors that directly influence the diameter of nanoparticles in nanoindentation lithography. First, the effect of the indentation process on the diameter of nanoparticles was investigated. Figure 3.6 shows the SEM image and depth profile of the AD-40-AS tip used for nanotip indentation lithography. As can be seen from the SEM images and tip specifications, the AD-40-AS tip is a very sharp tip, so it can generate nanoparticle patterns with a diameter of several tens of nanometers. Figure 3.6b shows a comparison of the depth profiles when indented with two different tips at the same depth. The two different depth profiles are almost identical. Although there is a slight difference in the surface, the part used to make the nanoparticles is about 40 nm from the deepest point, So the similar result can be achieved with other tips by adjusting the indentation conditions. For this reason, the tips should be calibrated to achieve similar results for each tip.

Figure 3.7 shows the AFM analysis results of indentation hole pattern. As can be seen from the depth profile results for various indentation depths in Figure 3.7b, the width increases with increasing indentation depth. Therefore, to make nanoparticles as small as several tens of nanometers, it is necessary to reduce the indentation depth. As a result of analyzing the indentation depth according to the applied force, the indentation depth increases in proportion

to the applied force when the polymer thickness is sufficient. However, as the polymer thickness decreases, the indentation depth decreases for the same applied force. The cause of these results can be understood as the difference in modulus between the 2nd polymer layer, MR-I 8010r and MR-I 8020r, and the 1st polymer layer, SF3. The modulus of SF3, 8010r, and 8020r were about 5 GPa [18], 3.3 GPa, and 2.5 GPa, respectively. Because the polymer layers with different modulus were attached to each other, a gradual change in modulus occurs at the interface. Since this effect occurs near 20 nm at the interface, the durability of the tip may be reduced if indentation is conducted at the interface to around 20 nm. Therefore, if indentation is required as thick as the 2nd polymer, it is recommended to change the condition as this may damage the tip.

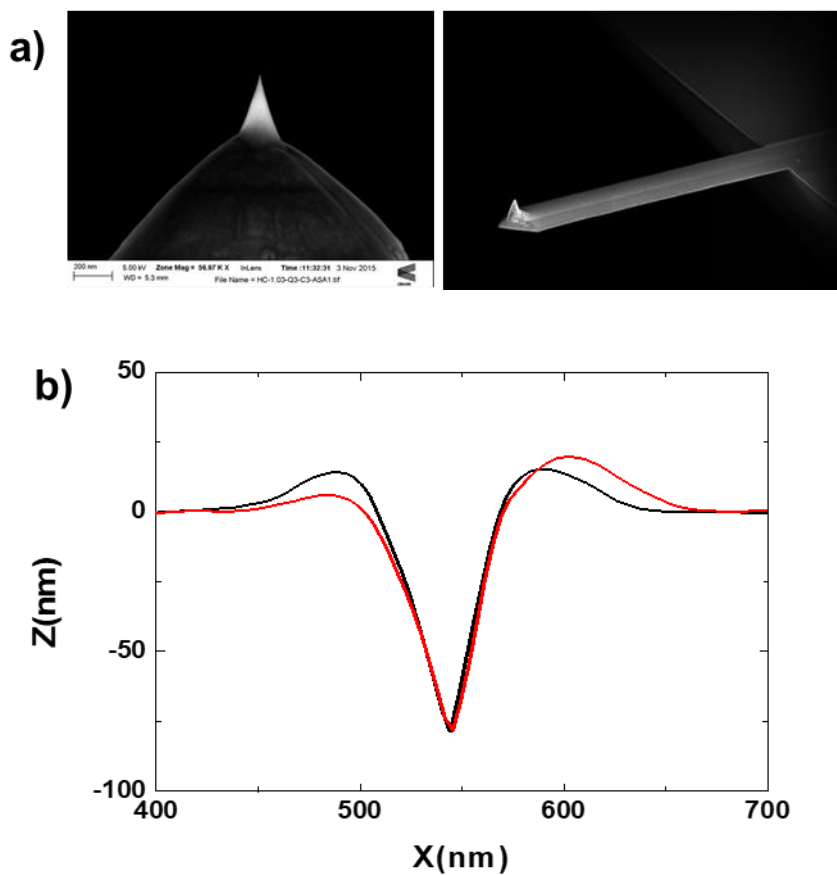


Figure 3.6 AD-40-AS AFM tip used for nanotip indentation lithography, a) SEM images, b) Depth profile of two different tips measured by AFM

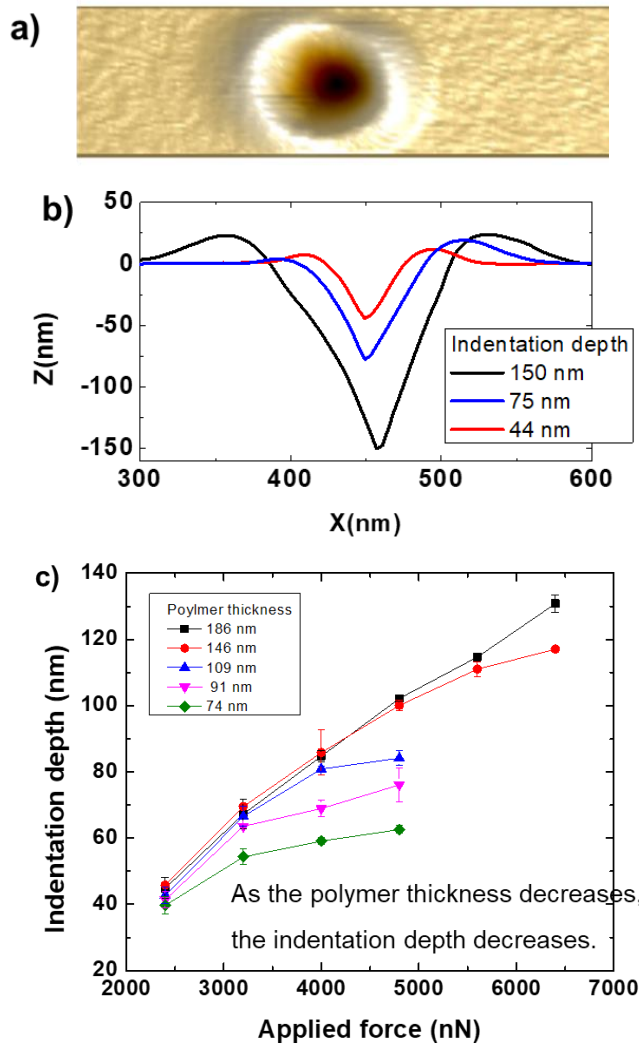


Figure 3.7 AFM analysis results of indentation hole pattern, a) 3D AFM image of single hole pattern, b) Change of depth profile according to indentation depth, c) Indentation depth analysis results according to various polymer thicknesses and applied forces

Second, the effect of reactive ion etching process on the diameter of nanoparticles was investigated. Figure 3.8 shows the analysis results for the change in opening size before and after reactive ion etching. Samples with a first polymer layer 138 nm thick and a second polymer layer 117 nm thick were prepared and nanohole patterns with an indentation depth of 114 nm were made using AFM. The depth profile result of the nanohole pattern was shown in Figure 3.8, and the opening size of 74 nm below the surface was measured to be 28.8 nm. The depth profile of the nanohole pattern after 40 nm reactive ion etching was shown in Figure 3.8b. After etching, the opening size of 74 nm below the surface were measured to be 46.1 nm. As a result of etching the 40 nm thickness of the 2nd polymer, it was observed that the aperture size increased by 17.3 nm. Figure 3.8c shows the measurement result of the increase in the opening size according to the etch depth. As the etch depth increases, the opening size also increases, but the increase in the opening size slightly decreases as the etch depth increases. As the increase in opening size ultimately directly affects the nanoparticle size, it is important to predict how much the diameter will increase due to reactive ion etching.

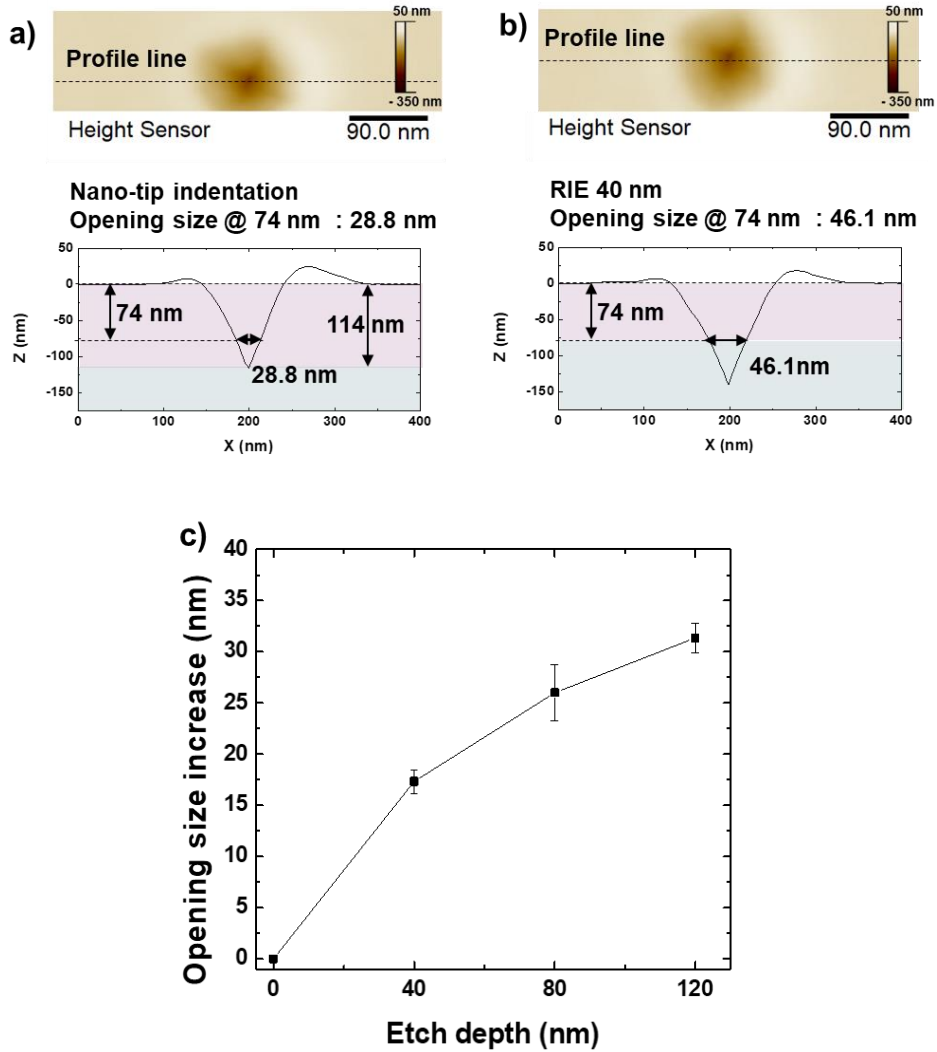


Figure 3.8 Analysis results for the change in opening size of nanohole pattern before and after reactive ion etching using atomic force microscope, a) opening size measurement result before etching, b) opening size measurement result after etching and, c) Analysis result of increase in opening size according to etching depth

Third, the effect of wet etching process on the diameter of nanoparticles was investigated. Figure 3.9 shows the analysis results for the change in opening size before and after wet etching process. Wet etching was performed using the same sample previously used for comparison of reactive ion etching effects. As a result of wet etching for 15 seconds, it was observed that the opening size of 46.1 nm increased slightly to 47.1 nm. When the wet etching time was increased to 30 s, the opening size increase was about 4.2 nm. Therefore, although the wet etching process influences the opening size, it was confirmed that the influence was significantly less than that of the previous two processes.

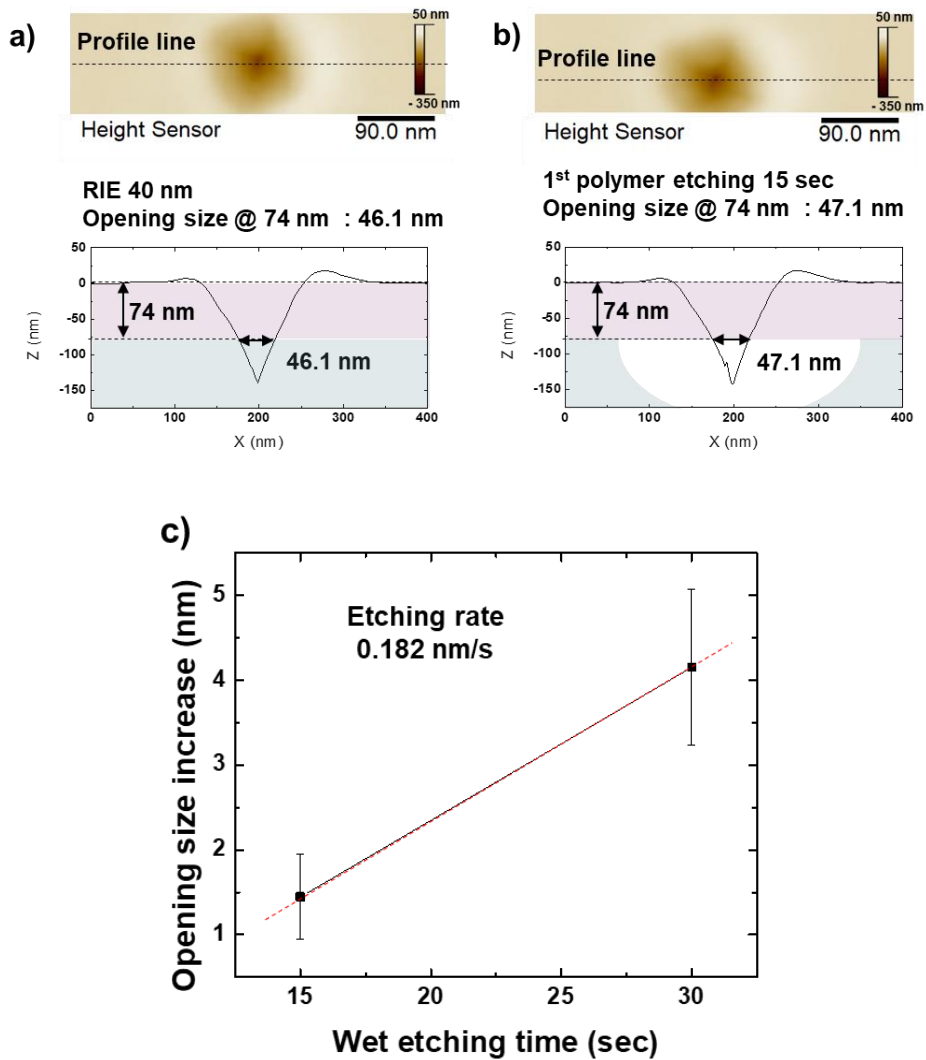


Figure 3.9 Analysis results for the change in opening size of nanohole pattern before and after wet etching using atomic force microscope, a) opening size measurement result before wet etching, b) opening size measurement result after wet etching and, c) Analysis result of increase in opening size according to wet etching time

To comprehensively view the above results, samples patterned with various indentation depths on 2nd polymers of various thicknesses were made and the diameters of the final nanoparticles were analyzed. All samples were etched so that the thickness of the secondary polymer was 30 nm to expose the primary polymer through reactive ion etching, and the wet etching time was fixed at 8 seconds. First, comparing the samples with 2nd polymer thicknesses of 149 nm and 109 nm, it can be seen that the indentation depth according to the indentation force of the two samples was similar. However, the diameter of the finally produced nanoparticles has a difference of about 20 nm. According to the above results, 40 nm reactive ion etching increased the opening size of about 17.3 nm, and it can be confirmed that almost the same result was observed. It was also observed that for the same polymer thickness, the diameter of the nanoparticles increased by about 2.5 nm when the indentation force was increased by 0.8 nN. Therefore, it was shown that the diameter of several nanometers can be controlled by adjusting the indentation force. In conclusion, it is possible to precisely control the diameter of nanoparticles through nanotip indentation lithography by comprehensively considering the above three factors.

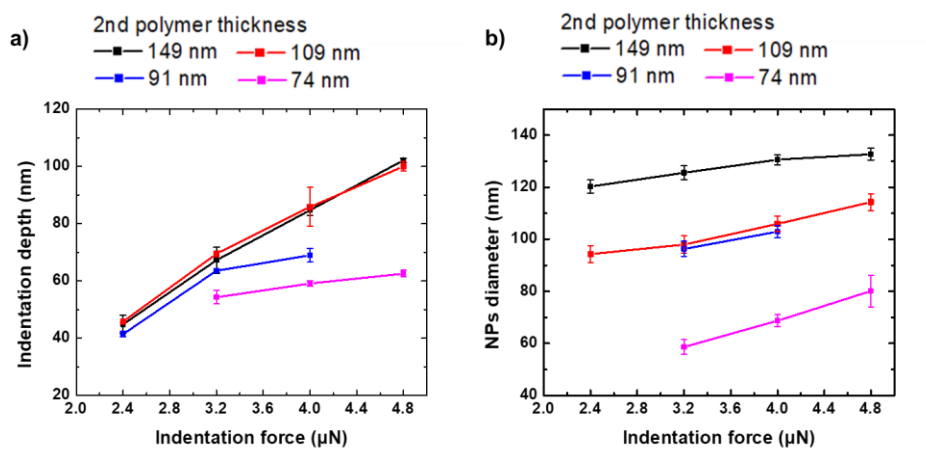


Figure 3.10 Measurement result of a) indentation depth and b) diameter according to indentation force for various thicknesses of the 2nd polymer

3.3.3. Fabrication results of nanoparticle arrays using nanotip indentation lithography

The optimized nanotip indentation lithography process recipes were summarized in Table 3.1. Figure 3.11 also shows SEM images of nanoparticles fabricated using the optimized process recipe. It has been demonstrated that nanoparticles with diameters from 58.6 nm to 132.7 nm can be effectively prepared using nanotip indentation lithography. Figure 3.12 shows the nanoparticle fabrication map for nanotip indentation lithography. Through the nanoparticle fabrication map, it is easier to determine the conditions for the fabrication of nanoparticles.

The SEM images and OM images of three large-area samples prepared for optical property measurement were shown in Figure 3.13. The first sample and the second sample had 46,085 nanoparticles in an area of 60 μm in width and 60 μm in length. The diameters of the first and second samples were 188.6 nm and 118.8 nm, respectively, and the pitch was 300 nm. Nanoparticles were prepared by depositing Ti 5 nm thick, Pd 19.7 nm thick, and Au 5.4 nm thick. The third sample had 147,755 nanoparticles in an area of 54 μm in width and 54 μm in length. The third sample has a diameter of 82.2 nm and a pitch of 150 nm. The third sample was difficult to measure due to the small particle size, which increased the deposited metal thickness. So, Ti 5 nm, Pd 27.9 nm, and Au 7.42 nm were deposited. All samples were annealed for 12 h at 600 $^{\circ}\text{C}$ in an argon atmosphere containing 4% hydrogen.

The XRD analysis results of large-area nanoparticle array samples were shown in Figure 3.14. As a result of 2theta scan from 20° to 90°, 111 plane peaks and 222 plane peaks were observed. The detailed analysis results for the 111 plane peak were shown in Figure 3.14b. In the case of the Pd7Au3 composition fabricated through nanoimprint lithography, the 111 plane peak was 39.577°, but in the case of the Pd7Au3 composition fabricated by nanotip indentation lithography, the 111 plane peaks were measured at 39.803°, 39.887° and 39.887°. This shift of the 111-plane peak means a change in composition. The composition of the sample made by nanotip indentation lithography, and the composition of the sample made by nanoimprint lithography are compared as follows. The composition corresponding to 39.803° was Pd81Au19, and the composition corresponding to 39.887° was Pd87Au13. It was observed that the gold content was lower than expected. These results imply that additional geometric considerations must be made to match the composition in nanotip indentation lithography. In nanoimprint lithography, the edge of the hole pattern is almost vertical, whereas in nanotip indentation lithography, there is a slope. This geometrical difference determines whether or not metal is deposited on the edge during metal deposition. If there is a slope, metal is deposited on the edge, resulting in blocking the hole pattern as the metal is deposited. This effect resulted in a smaller deposition of gold and a smaller composition than expected. The Θ value according to the composition obtained through calculation was as

follows: The Θ value corresponding to the composition of Pd₈₁Au₁₉ was 33°, The Θ value corresponding to the composition of Pd₈₁Au₁₉ was 26°. It was confirmed that geometrical factors have a great influence on alloy composition. To achieve the desired composition, metal deposition should be performed in consideration of these effects.

Table 3.1 The optimized process recipes for nanotip indentation lithography

| Diameter (nm) | Pitch (nm) | 1st polymer | | | 2nd polymer | | | Indentation force (μN) | Indentation depth (nm) | RIE thickness (nm) | Etching time (sec) |
|--|------------|-------------|--------------------|----------------|-------------|--------------------|----------------|------------------------|------------------------|--------------------|--------------------|
| | | Material | Spin coating (RPM) | Thickness (nm) | Material | Spin coating (RPM) | Thickness (nm) | | | | |
| 132.7 | 300 | PMGI SF3 | 2000 | 95 | MR-I 8020R | 3000 | 186 | 4.8 | 114.3 | 105 | 2~8 |
| 125.6 | 300 | PMGI SF3 | 2000 | 95 | MR-I 8020R | 3000 | 186 | 3.2 | 97.9 | 105 | 3~8 |
| 114.3 | 300 | PMGI SF3 | 2000 | 95 | MR-I 8020R | 5000 | 146 | 4.0 | 103.0 | 70 | 3~8 |
| 105.9 | 300 | PMGI SF3 | 2000 | 95 | MR-I 8020R | 5000 | 146 | 3.6 | 100.0 | 70 | 3~8 |
| 96.3 | 300 | PMGI SF3 | 2000 | 95 | MR-I 8010R | 2000 | 109 | 3.2 | 66.6 | 70 | 4~8 |
| 80.1 | 300 | PMGI SF3 | 2000 | 95 | MR-I 8010R | 3000 | 91 | 4.8 | 76.1 | 50 | 4~8 |
| 68.7 | 300 | PMGI SF3 | 2000 | 95 | MR-I 8010R | 3000 | 91 | 4.0 | 68.9 | 50 | 5~8 |
| 58.6 | 300 | PMGI SF3 | 2000 | 95 | MR-I 8010R | 3000 | 91 | 3.2 | 63.6 | 50 | 5~8 |
| Optical hydrogen measurement samples over 50 μm x 50 μm | | | | | | | | | | | |
| 188.6 | 300 | PMGI SF3 | 2000 | 95 | MR-I 8020R | 2000 | 220 | 4.8 | 89.8 | 185 | 4 |
| 118.8 | 300 | PMGI SF3 | 5000 | 75 | MR-I 8010R | 3000 | 91 | 3.2 | 53.0 | 65 | 3 |
| 82.2 | 150 | PMGI SF3 | 2000 | 95 | MR-I 8020R | 2000 | 200 | 5.6 | 92.0 | 65 | 3 |

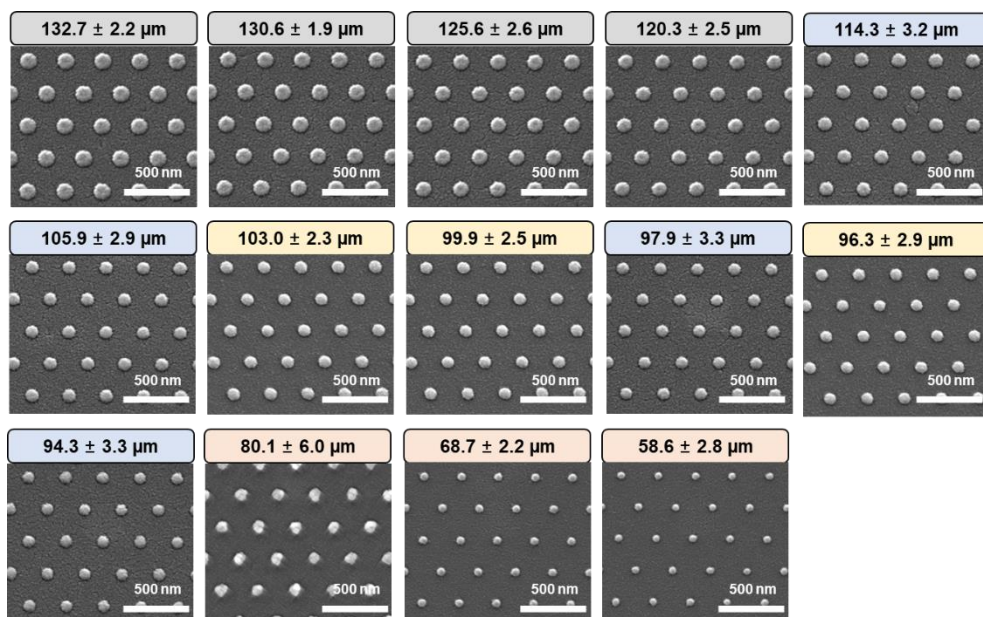


Figure 3.11 SEM images of nanoparticles of various diameters fabricated with the optimized process recipes.

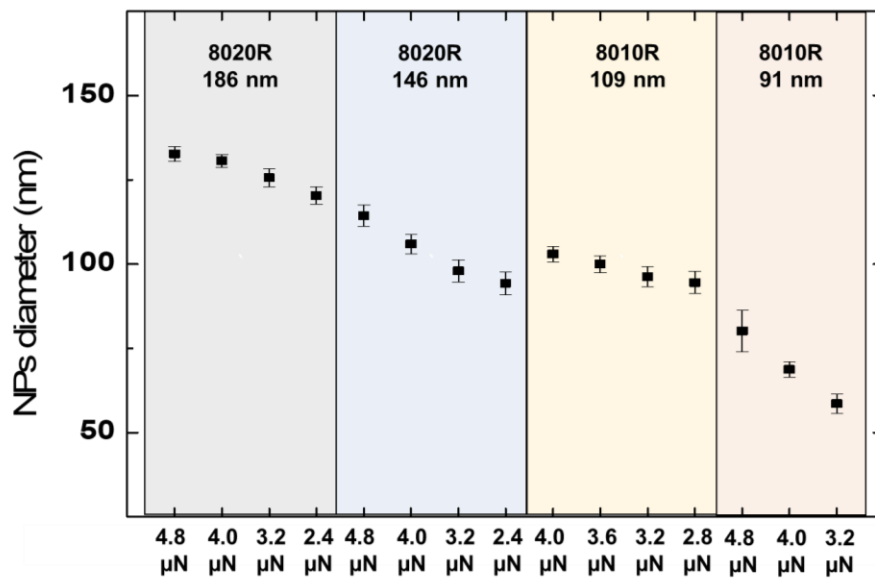


Figure 3.12 Nanoparticle fabrication map for nanotip indentation lithography

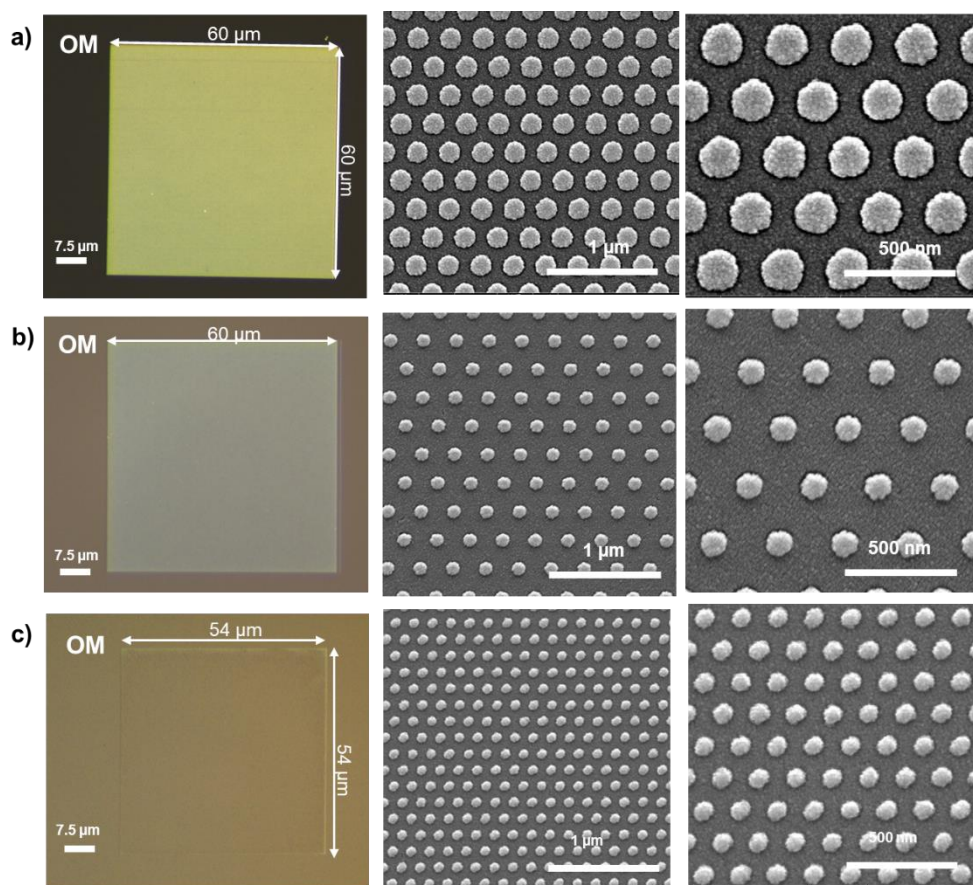


Figure 3.13 Large-area nanoparticle array made by nanotip indentation lithography for measurement of optical properties, a) array of PdAu nanoparticles with a diameter of 188.6 nm and a pitch of 300 nm, Array of PdAu nanoparticles with a diameter of 118.8 nm and a pitch of 300 nm, c) Array of PdAu nanoparticles with a diameter of 82.2 nm and a pitch of 150 nm

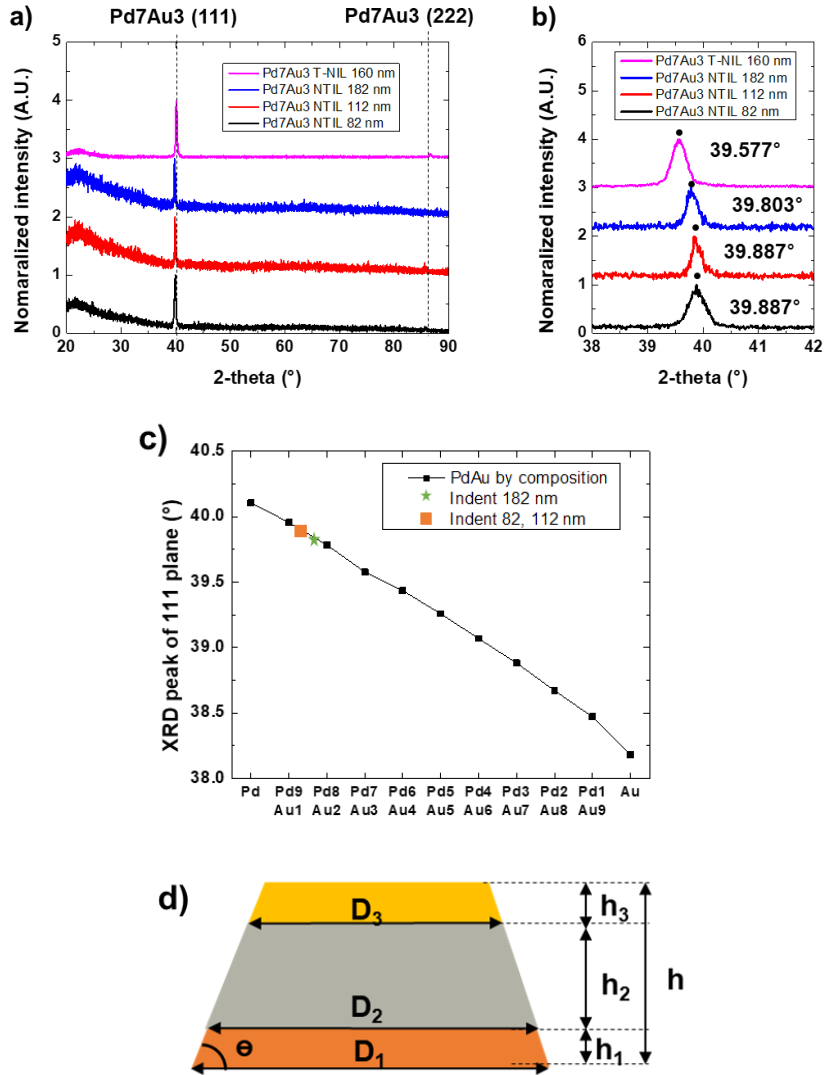


Figure 3.14 XRD measurement result of large-area nanoparticle array, a) 2Theta-theta scan results from 20° to 90°, b) Detailed analysis of 111 plane peak, c) Result of composition analysis according to the position of the 111-plane peak, d) Schematic diagram of geometric considerations

3.4. Summary

In this chapter, we demonstrated the fabrication of nanoparticle arrays using nanotip indentation lithography. By optimizing the process of nanotip indentation lithography, it was demonstrated that nanoparticles can be effectively controlled from 58 nm to 138 nm. In addition, factors that directly or indirectly affect the diameter of nanoparticles were investigated, and it was confirmed how much the diameter of nanoparticles increased by the factors. With the optimized process conditions, large-area samples of 50 μm or more could be produced, and more than 140,000 nanoparticles could be successfully produced. However, additional geometric considerations were required to match the alloy composition of the nanoparticles, and the Θ value of the sample prepared by indentation of the nanotip was measured to be about 26° to 33° .

3.5 Bibliography

- [1] C.L. Nehl and J.H. Hafner, "Shape-dependent plasmon resonances of gold nanoparticles." *Journal of Materials Chemistry*, 18.21, (2008), 2415-2419.
- [2] Z. Zhang, Z. Chen, C. Qu and L. Chen, "Highly sensitive visual detection of copper ions based on the shape-dependent LSPR spectroscopy of gold nanorods." *Langmuir*, 30.12, (2014), 3625-3630.
- [3] H.B. Jeon, P.V. Tsalu and J.H. Ha, "Shape effect on the refractive index sensitivity at localized surface plasmon resonance inflection points of single gold nanocubes with vertices." *Scientific reports*, 9.1, (2019), 1-8.
- [4] J. Kim, A. Agrawal, F. Krieg, A. Bergerud and D.J. Milliron, "The interplay of shape and crystalline anisotropies in plasmonic semiconductor nanocrystals." *Nano Letters*, 16.6, (2016), 3879-3884.
- [5] H. Baida, P. Billaud, S. Marhaba, D. Christofilos, E. Cottancin, A. Crut and L.M. Liz-Marzán, "Quantitative determination of the size dependence of surface plasmon resonance damping in single Ag@SiO₂ nanoparticles." *Nano letters*, 9.10, (2009), 3463-3469.
- [6] V. Juvé, M.F. Cardinal, A. Lombardi, A. Crut, P. Maioli, J. Pérez-Juste and F. Vallée, "Size-dependent surface plasmon resonance broadening in nonspherical nanoparticles: single gold nanorods." *Nano letters*, 13.5, (2013), 2234-2240.
- [7] J. Lermé, H. Baida, C. Bonnet, M. Broyer, E. Cottancin, A. Crut and M. Pellarin, "Size dependence of the surface plasmon resonance

- damping in metal nanospheres." *The journal of physical chemistry letters*, 1.19, (2010), 2922-2928.
- [8] T. Huang and X.H.N. Xu, "Synthesis and characterization of tunable rainbow colored colloidal silver nanoparticles using single-nanoparticle plasmonic microscopy and spectroscopy." *Journal of materials chemistry*, 20.44, (2010), 9867-9876.
- [9] X. Zhang, S. Ye, X. Zhang and L. Wu, "Optical properties of SiO₂@M (M= Au, Pd, Pt) core-shell nanoparticles: Material dependence and damping mechanisms." *Journal of Materials Chemistry C*, 3.10, (2015), 2282-2290.
- [10] G.H. Chan, J. Zhao, G.C. Schatz and R.P. Van Duyne, "Localized surface plasmon resonance spectroscopy of triangular aluminum nanoparticles." *The Journal of Physical Chemistry C*, 112.36, (2008), 13958-13963.
- [11] S. Syrenova, C. Wadell, F.A. Nugroho, T.A. Gschneidtnr, Y.A. Diaz Fernandez, G. Nalin and C. Langhammer, "Hydride formation thermodynamics and hysteresis in individual Pd nanocrystals with different size and shape." *Nature materials*, 14.12, (2015), 1236-1244.
- [12] C. Langhammer, V.P. Zhdanov, I. Zorić and B. Kasemo, "Size-dependent kinetics of hydriding and dehydriding of Pd nanoparticles." *Physical review letters*, 104.13, (2010), 135502.
- [13] X. Luo, D. Tsai, M. Gu and M. Hong, "Extraordinary optical fields in nanostructures: from sub-diffraction-limited optics to sensing and energy conversion." *Chemical Society Reviews*, 48.8, (2019), 2458-2494.
- [14] G.A Shaw, J. Kramar and J. Pratt, "SI-traceable spring constant

- calibration of microfabricated cantilevers for small force measurement." *Experimental mechanics*, 47.1, (2007), 143-151.
- [15] E.D. Langlois, G.A. Shaw, J.A. Kramar, J.R. Pratt and D.C Hurley, "Spring constant calibration of atomic force microscopy cantilevers with a piezosensor transfer standard." *Review of Scientific Instruments*, 78.9, (2007), 093705.
- [16] E.P. Wojcikiewicz, X. Zhang and V.T. Moy, "Force and compliance measurements on living cells using atomic force microscopy (AFM)." *Biological procedures online*, 6.1, (2004), 1-9.
- [17] M.R. Vanlandingham, S.H. McKnight, G.R. Palmese, J.R. Elings, X. Huang, T.A> Bogetti and J.W. Gillespie Jr, "Nanoscale indentation of polymer systems using the atomic force microscope." *The Journal of adhesion*, 64.1-4, (1997), 31-59.
- [18] I.G. Foulds, R.W. Johnstone, S.H. Tsang, M. Hamidi and M. Parameswaran, "Polydimethylglutarimide (PMGI) as a structural material for surface micromachining." *Journal of Micromechanics and Microengineering*, 18.4, (2008), 045026.

Chapter 4. Study on optical hydrogen measurement of PdAu alloy nanoparticle arrays

4.1. Introduction

In this chapter, we will discuss the optical properties and hydrogen measurement properties of PdAu nanoparticle arrays fabricated by nanoimprint lithography and nanoindentation lithography. Firstly, through the FDTD simulation, it was showing that the hexagonal pattern has better sensitivity than the random pattern. And the shift of the LSPR peak according to the various diameters of the Pd nanoparticles was predicted. As for the optical properties, the peak of localized surface plasmon resonance, transmittance, and extinction were investigated. As for the hydrogen sensing properties, response time, recovery time, sensitivity, and limit of detection (LoD) were investigated. To predict the trend of the LSPR peak shift, the LSPR peak change of Pd nanoparticles was simulated through FDTD simulation. The optical properties and hydrogen detection properties according to the PdAu alloy composition were analyzed. For the Pd₇Au₃ composition, the changes in optical properties and hydrogen sensing properties according to the annealing temperature were analyzed. The mechanics of changing properties according to the annealing temperature

were discussed. Finally, the optimal compositions of PdAu alloy were discussed.

4.2. Experimental details

4.2.1. FDTD simulation of Pd nanodisk

FDTD simulations were performed to compare the sensitivities of random and hexagonal structures and to investigate the LSPR peak changes of Pd nanoparticles. Schematic diagrams of random and hexagonal nanoparticle arrays were shown in Figure 4.1. First, the composition of nanoparticles was disk-shaped with a height of Ti 5 nm and Pd 25 nm, and the substrate was composed of quartz. The random and hexagonal structures were shown in Figure 4.1b and Figure 4.1c, respectively. The simulation size of the random structure was set to 500 nm in x-axis length, 500 nm in y-axis length, and 500 nm in z-axis length. The simulation size of the hexagonal structure was set to 346.41 nm in x-axis length, 200 nm in y-axis length, and 500 nm in z-axis length. The pitch of the hexagonal-structured nanoparticles was set to 200 nm. For the boundary conditions of the FDTD simulation, the x-axis and y-axis were set as periodic conditions, and z was set as a perfect matched layer (PML). The simulation was performed by changing the diameter of the nanoparticles from 60 nm to 140 nm at intervals of 10 nm under the above conditions. The sensitivity value was obtained by measuring

the extinction change at the same wavelength when changing to PdHx after obtaining the localized surface plasmon resonance peak value of Pd and the extinction value at this time. The n and k values of Pd measured by W.S.M. Werner et. al. were used [1]. The n and k values of PdHx measured by K.J. Palm et. al. were used [2]. To investigate the change in the LSPR peak of the hexagonal structure of Pd nanoparticles, FDTD simulations were performed by changing the diameter from 80 nm to 160 nm at intervals of 20 nm. The LSPR peak value was obtained using the extinction value at this time.

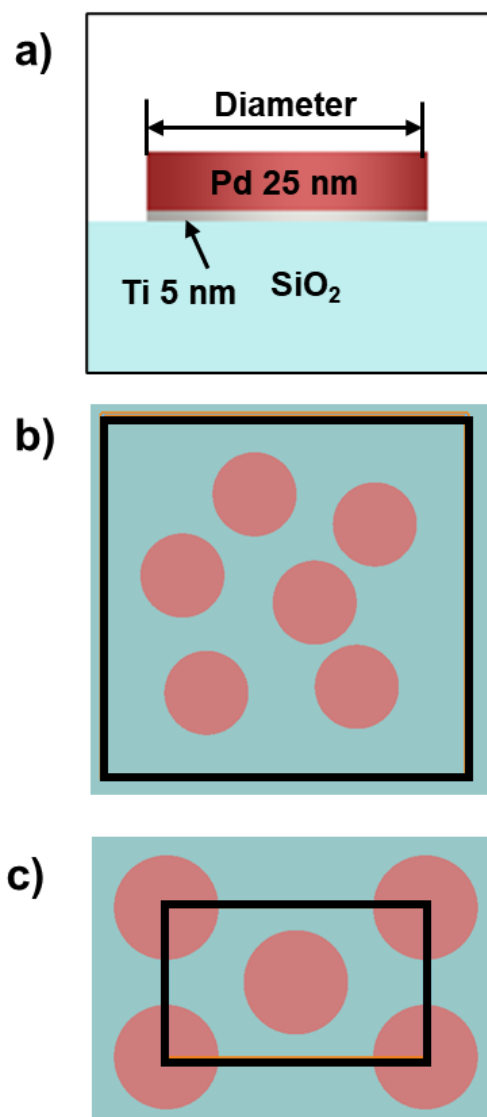


Figure 4.1 Schematic diagram of nanoparticle arrays for FDTD simulations, a) the structure of nanoparticles, b) randomly structured nanoparticle array, c) hexagonal structured nanoparticle arrays

4.2.2. Evaluation of optical properties and hydrogen sensing properties of PdAu nanoparticle arrays

The evaluation of optical properties and hydrogen sensing properties was performed in the optical hydrogen measurement system. For the optical properties, transmittance, extinction, and LSPR peak were measured and calculated. The transmittance was set to 100% for the area without particles on the substrate with nanoparticles, and the transmittance of nanoparticle array was measured when light passed through the nanoparticle area. Extinction was obtained by calculating the percentage of light that was not transmitted as light passed through the nanoparticle area. Finally, LSPR peak values were calculated through Lorentz fitting of the wavelength-dependent extinction graph [3,4].

Response time, recovery time, sensitivity, and limit of detection were measured to evaluate the hydrogen detection properties, and the measurement methods were shown in Figure 4.2. First, the response value was obtained using the transmittance in vacuum and the transmittance after hydrogen was added, and the calculation formula was as follow:

$$Response(\%) = \frac{T_{Hydrogen} - T_{Vacuum}}{T_{Vacuum}} \times 100 \quad \text{-----}(4.1)$$

When hydrogen flows in a vacuum, the response value changes to a positive value. The time it takes up to change up to 90% of the maximum

response value is called response time. The time it takes for the response to change from the maximum value to 10% of the maximum value when the response falls back to the vacuum state is called the recovery time. A schematic diagram of recovery time and response time is shown in Figure 4.2a. Sensitivity represents the slope in the hydrogen concentration versus response graph. It means how much the response value changes at the same hydrogen partial pressure, and the larger the sensitivity value, the larger the change. The lowest measurable hydrogen concentration is used as the limit of detection. A schematic diagram of sensitivity and limit of detection is shown in Figure 4.2b. And normal hydrogen measurements and LoD measurements were performed at base pressures of 6.0×10^{-2} torr and 6.0×10^{-5} torr, respectively.

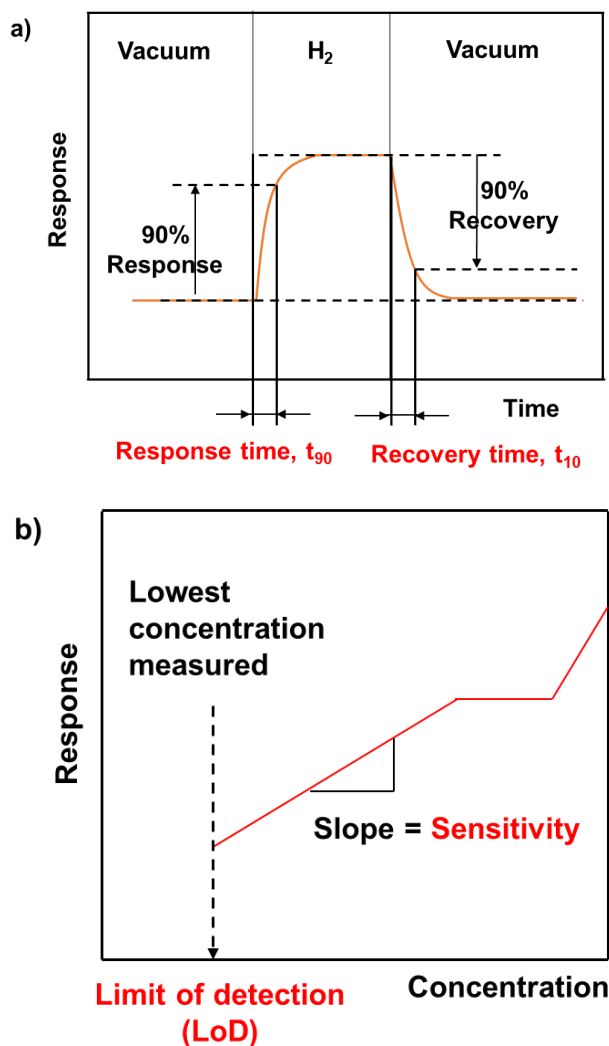


Figure 4.2 Hydrogen sensing properties measurement, a) Schematic diagram illustrating response time and recovery time, b) Schematic diagram explaining sensitivity and limit of detection

4.3. Results and discussions

4.3.1. Comparison of transmittance change between random and hexagonal structures

To explain the differences between the random and hexagonal structures, the transmittances of Pd and PdHx of each structure were compared. Figure 4.3a showed simulated transmittance values for random and hexagonal structures of 140 nm diameter particles. In the hexagonal structure, it was confirmed that the extinction occurred strongly around 400 nm wavelength due to localized surface plasmon resonance. In addition, it was investigated that the LSPR peak value shifted to blue when Pd was subjected to a phase change to PdHx. In the random structure, Pd nanoparticle array showed the lowest transmittance due to local surface plasmon resonance at 481 nm wavelength, but it was difficult to specify the peak value in PdHx.

To compare the magnitude of the change in the random and hexagonal structures, the difference between the transmittance of Pd and PdHx at the wavelength value, which is the LSPR peak of Pd nanoparticles, was compared, and the results were shown in Figure 4.3b. As a result of performing a simulation of changing the diameter of Pd nanoparticles from 60 nm to 140 nm for the same hydrogen partial pressure, a larger change was observed in the hexagonal structure. This means that the measurement is easier because a larger change is led at the same hydrogen partial pressure,

and it also means that the limit of detection can be increased. However, a limitation of these simulation results is that one random structure cannot represent all random structures. Nevertheless, the simulation results are meaningful in that there is a section where the hexagonal structure shows a larger change in transmittance even when simulated with a different random structure. Therefore, through the simulation results, it was confirmed that the hexagonal structure showed a greater difference in transmittance at the same hydrogen partial pressure, which is expected to further increase the sensitivity and limit of detection.

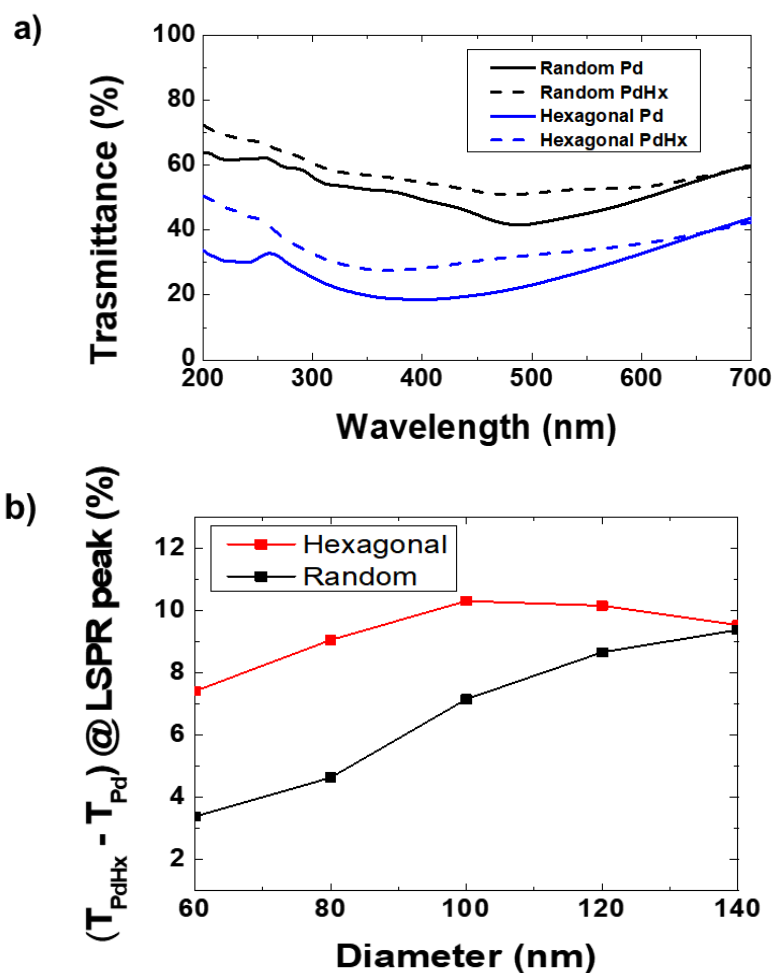


Figure 4.3 Comparison of sensitivity between random and hexagonal structures, a) Transmittance simulation results of Pd and PdHx in an array of 140 nm diameter nanoparticles with random and hexagonal structures, b) Simulation results of transmittance change according to nanoparticle diameter change

4.3.2. FDTD simulation results of the LSPR peak shift for Pd nanoparticle arrays of various diameter

FDTD simulation was performed to investigate the shift of the LSPR peak according to the change in the diameter of Pd nanoparticles. FDTD simulation results for Pd nanoparticle arrays of various diameters were shown in Figure 5.4. Since the pitch of the nanoparticles was fixed at 200 nm, it was observed that the transmittance to the incident light increases as the size of the nanoparticles increases. Conversely, in the case of extinction, it was found that the extinction value increased as the diameter of nanoparticles increased. Also, the change of the LSPR peak value was observed through the maximum value of the calculated extinction result. It was confirmed that the LSPR peak value decreased from 410.1 nm to 323.8 nm as the diameter decreased from 160 nm to 80 nm. As is generally known, it was confirmed that the blue shift occurs when the diameter of the nanoparticles decreases [5-7]. By comparing the FDTD simulation data with the actual measurement results, it is used to determine whether the change of the LSPR peak in the measurement results is due to the decrease in diameter of nanoparticles.

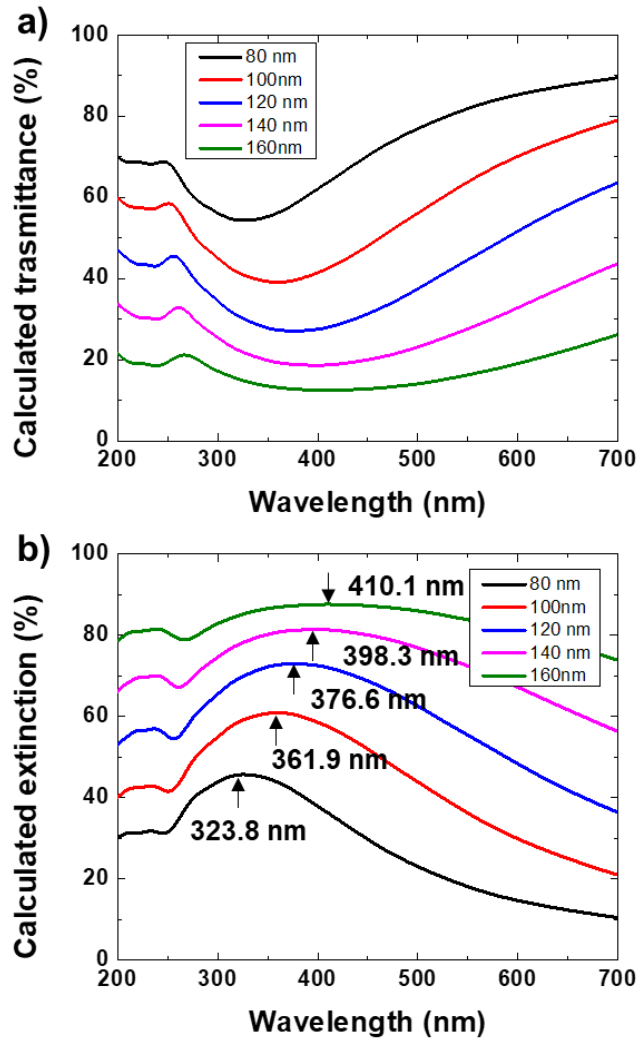


Figure 4.4 FDTD simulation results for Pd nanoparticle arrays of various diameter, a) transmittance spectra, b) extinction spectra

4.3.3. The optical properties of nanoimprinted PdAu nanoparticle arrays

The optical properties of PdAu compositions of various compositions fabricated by nanoimprint lithography were investigated. The extinction spectra and FDTD simulation results of nanoimprinted Pd and Au nanoparticle arrays was shown in Figure 4.5. In the LSPR spectrum of the nanoimprinted nanoparticle array, two peaks were observed. Peak1 found between 200 nm and 300 nm was observed only in the nanoimprinted sample, and the other peak2 was confirmed to be the LSPR peak of the nanoparticle array. Peak 1 is estimated to be a peak caused by a change in the quartz substrate due to a large pressure applied to the substrate during the nanoimprint process. Therefore, the LSPR peak dealt with in this thesis means peak2.

As shown in Figure 4.5, the LSPR peaks of the Pd and Au nanoparticle arrays with a hexagonal pattern and a diameter of 160 nm were 441.0 nm and 603.2 nm, respectively. The LSPR peaks of the 120 nm and 190 nm diameter Pd nanoparticle arrays with random structure and nanodisk shape prepared by nanosphere lithography were about 514.5 nm and 747.3 nm, respectively [8]. The LSPR peaks of the 165 nm diameter Au nanoparticle array with a square pattern and a nanodisk shape fabricated by nanoimprint lithography were about 856 nm [9]. As a result of arranging nanoparticles in a hexagonal pattern, the LSPR peak was blue shifted, and it was confirmed that the peak

was significantly sharper than that of a random structure. The FWHM values of randomized 190 nm and hexagonal 160 nm Pd nanoparticle arrays were 695 nm and 366 nm, respectively. When the LSPR peak becomes sharp, the change in the LSPR peak can be seen better, so the sensitivity of the sensor increases [10,11].

Comparing the FDTD simulation value with the actual measured value, the differences between the measured LSPR peaks and the simulated LSPR peaks for the Pd and Au nanoparticle arrays were 17.5 nm and 52.7 nm, respectively. There was a difference of about 4.0% and 8.7% with the measured LSPR peak value. Although there is a slight difference from the actual value, an approximate value is obtained through FDTD simulation. On the other hand, the difference in the extinction value had a big difference between the actual measured value and the simulated value. In the case of Pd, the actual measured extinction value was 49.8% at the LSPR peak, but the simulated extinction value was 85.6%. This was a value corresponding to 172% of the actual measured extinction value. In the case of Au, the actual measured extinction value was 84.2% at the LSPR peak, but the simulated value was 93.8%. Although the difference was smaller than that of Pd, it was a value corresponding to 111% of the actual measured value. In conclusion, it was confirmed that the LSPR peak value agrees with the simulation, but the simulated extinction value was significantly different from the actual value, especially in Pd.

The extinction spectra and LSPR peak values of PdAu alloys for various compositions were shown in Figure 4.6. The diameter, ratio, pitch and LSPR peaks for various PdAu compositions were summarized in Figure 4.7. As can be seen in Figure 4.7a of the change of the LSPR peak value according to the composition of the PdAu alloy, the LSPR peak tends to decrease until the Au content reaches 80%, and then increases rapidly after 80%. In other papers, the LSPR peak value of the alloy does not simply increase, but decreases and then increases, or increases and decreases [12]. As measured in the case of the PdAu composition, the LSPR peak value decreases and rapidly increases until the Au content reaches 80%, which is a sufficiently reasonable result.

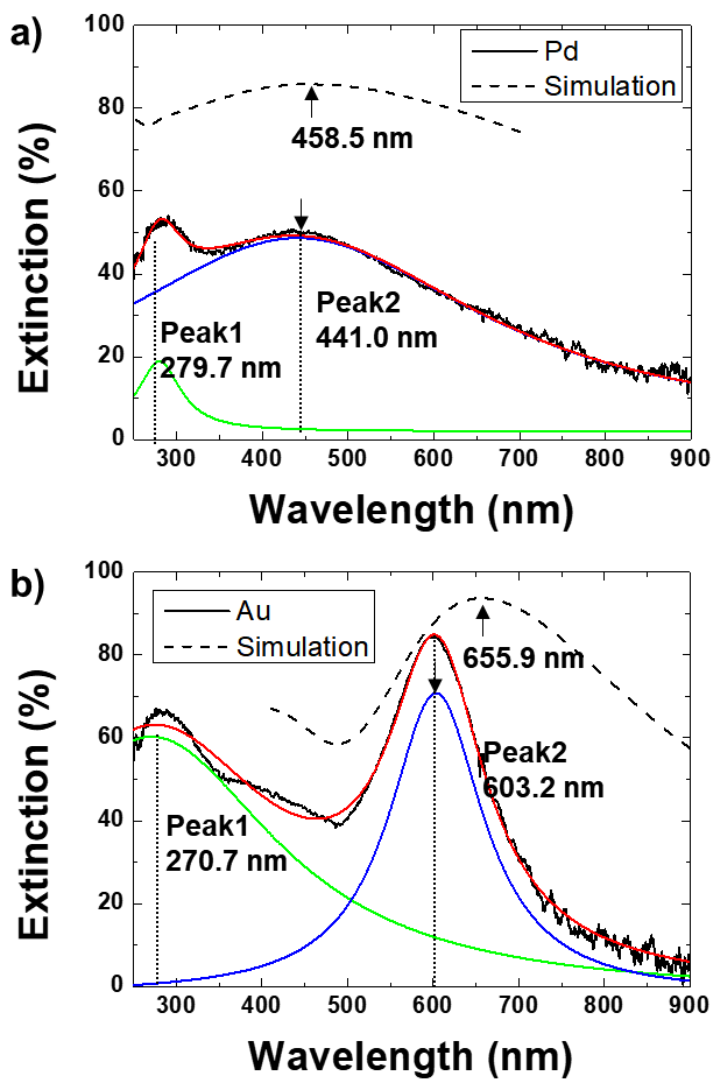


Figure 4.5 Measured extinction spectra and simulated results, a) nanoimprinted Pd nanoparticle array, b) nanoimprinted Au nanoparticle array

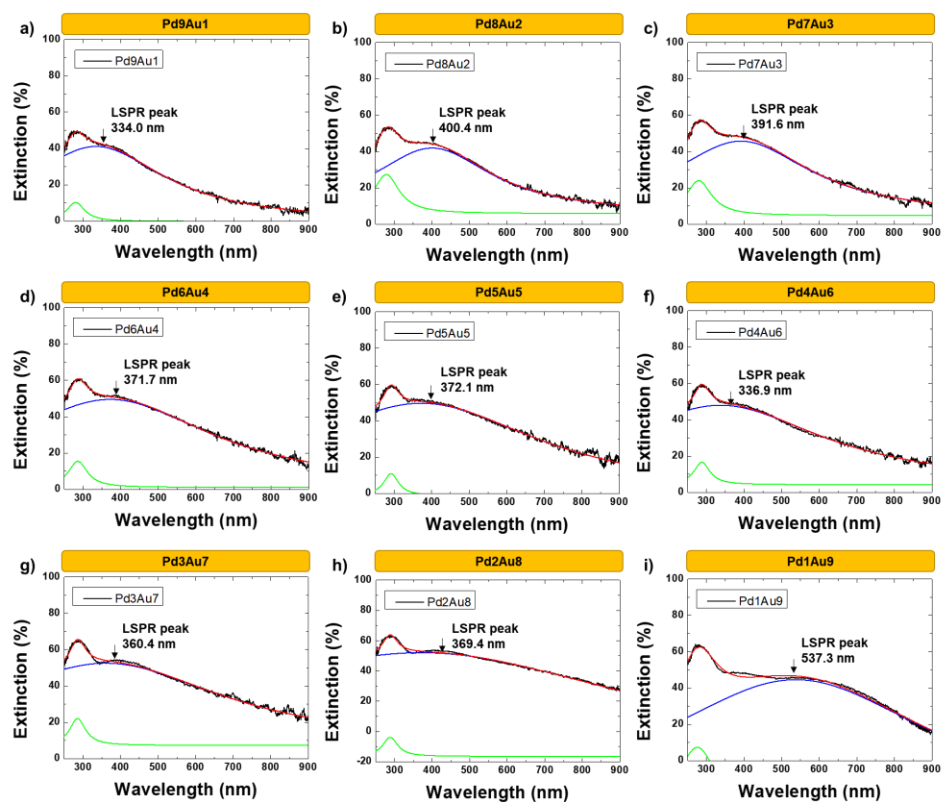
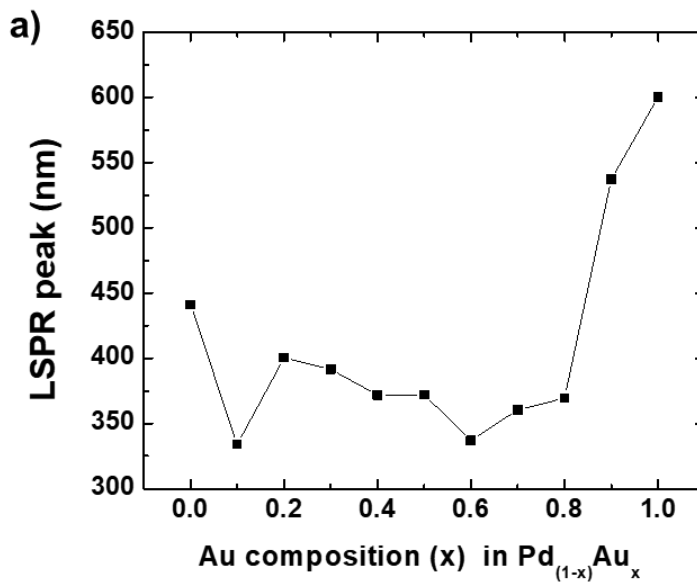


Figure 4.6 Measured extinction spectra of nanoimprinted PdAu nanoparticle arrays, a) Pd9Au1, b) Pd8Au2, c) Pd7Au3, d) Pd6Au4, e) Pd5Au5, f) Pd4Au6, g) Pd3Au7, h) Pd2Au8, i) Pd1Au9



b)

| Composition | Diameter (nm) | | Ratio | Pitch (nm) | LSPR peak (nm) |
|-------------|---------------|------------|-------|------------|----------------|
| | Major axis | Minor axis | | | |
| Pd | 161.5 | 141.1 | 0.873 | 200 | 441.0 |
| Pd9Au1 | 149.0 | 133.4 | 0.895 | | 334.0 |
| Pd8Au2 | 142.2 | 130.2 | 0.916 | | 400.4 |
| Pd7Au3 | 151.3 | 134.2 | 0.887 | | 391.6 |
| Pd6Au4 | 145.4 | 130.9 | 0.900 | | 371.7 |
| Pd5Au5 | 148.8 | 132.6 | 0.892 | | 372.1 |
| Pd4Au6 | 141.6 | 130.9 | 0.924 | | 336.9 |
| Pd3Au7 | 143.1 | 132.7 | 0.928 | | 360.4 |
| Pd2Au8 | 142.8 | 132.6 | 0.928 | | 369.4 |
| Pd1Au9 | 139.4 | 138.7 | 0.995 | | 537.3 |
| Au | 154.0 | 146.6 | 0.952 | | 600.3 |

Figure 4.7 a) Change of LSPR peak according to Au composition of PdAu alloys, b) Summary of diameter, ratio, pitch, LSPR peak for various PdAu composition

The optical properties of the Pd₇Au₃ compositions annealed at various temperatures were investigated. The measured extinction spectrum and transmittance spectrum of Pd₇Au₃ nanoparticle arrays annealed at 400 °C, 500 °C, 600 °C and 700 °C were shown in Figure 4.8. The transmittance changes according to the phase transition from PdAu to PdAuHx. Measuring these changes at various hydrogen concentrations enables optical hydrogen measurements, which will be discussed later.

The change in the LSPR peak obtained from the measured extinction data in Figure 4.8 was shown in Figure 4.9a. The LSPR peak value tends to decrease slightly as the annealing temperature increases, as the surface tension decreases and affinity to the substrate improves [13]. The change in the LSPR peak that occurs when changing from 400 °C to 500 °C is for this reason. Also, a change from 400° to 500° is understood as a short-range order crystal change. At an annealing temperature of 500°C, since the atoms on the surface of the nanoparticles are not large enough to move, they are slightly changed by diffusion, resulting in a small change in LSPR.

The reason why the LSPR peak was blue shifted significantly as the annealing temperature is changed from 500 °C to 600 °C is the high crystallinity and the effect of residual stress reduction. An annealing temperature of 600 °C provides sufficient energy to coalesce small particles into large particles and has the highest crystallinity index in the in-plane direction in the XRD data. On the other hand, the 700 °C annealed sample had the smallest FWHM value of 2theta, but it was confirmed that the

orientation in the in-plane direction was lowered. An annealing temperature of 600 °C appears to lower the residual stress in the crystals, as this is sufficient energy to move atoms on the surface of the nanoparticles. For these two reasons, the value of the LSPR peak at 600 °C changed significantly. Also, the reason the LSPR peak was redshifted at 700 °C was due to a sharp increase in the surface Au content. This is because as the annealing temperature increased, the tendency of Au atoms to go to the surface became stronger than the effect of 4% hydrogen [14-16]. Also, as shown in the FDTD simulation result in Figure 4.9c, the high Au content on the surface redshifts the LSPR peak.

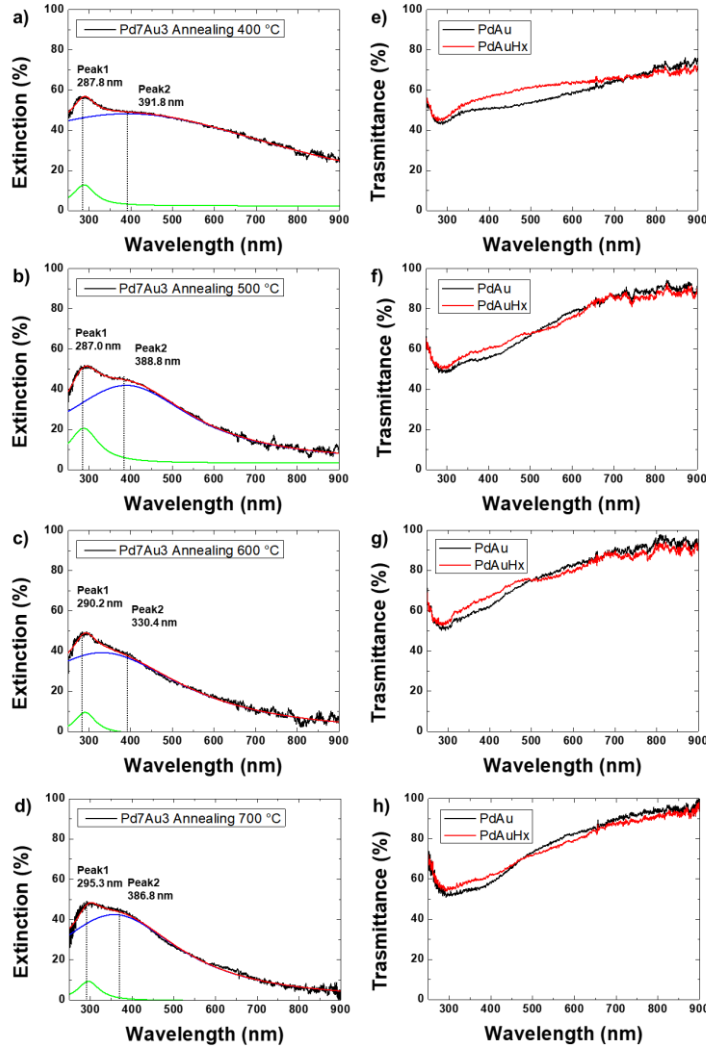


Figure 4.8 Measured extinction and transmission spectra of Pd₇Au₃ nanoparticle arrays for various annealing temperatures, a) extinction and e) transmittance of the sample annealed at 400 °C, b) extinction and f) transmittance of the sample annealed at 500 °C, c) extinction and g) transmittance of the sample annealed at 600 °C, d) extinction and h) transmittance of the sample annealed at 700 °C

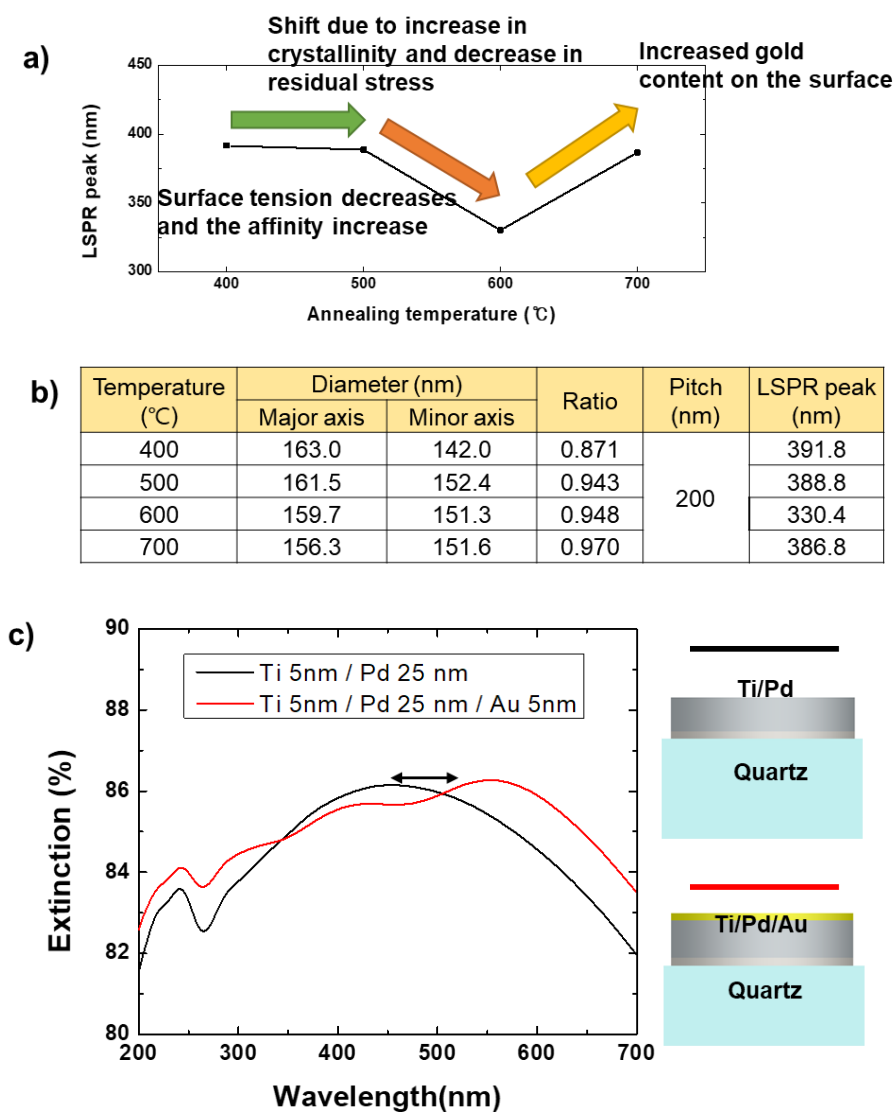


Figure 4.9 a) Change of LSPR peak according to annealing temperature, b) Summary of diameter, ratio, pitch, LSPR peak of Pd7Au3 composition for various annealing temperature, c) FDTD simulation results with and without Au 5 nm added to the surface

4.3.4. The optical properties of PdAu nanoparticle arrays fabricated by nanotip indentation lithography

The optical properties of the PdAu nanoparticle arrays fabricated by nanotip indentation lithography were investigated. Extinction spectrum was used to calculate the LSPR peak value according to the nanoparticle diameter. The LSPR peak of the sample having a diameter of 182 nm and a pitch of 300 nm was calculated to be 444.6 nm, the LSPR peak of the sample having a diameter of 118.2 nm and a pitch of 300 nm was calculated to be 336.7 nm, and finally, the LSPR peak of the sample having a diameter of 82.2 nm and a pitch of 150 nm was calculated to be 307.7 nm. Changes in LSPR peak values are graphically summarized in Figure 4.11a. When compared with the results simulated with an array of Pd nanoparticles, there was a difference in absolute values, but it was confirmed that the amount of decrease in the LSPR peak value due to the decrease in nanoparticles showed a similar trend. This means that only the size reduction acted on the reduction of the LSPR peak. When the optical properties of nanoparticles are changed, the trend is different from the FDTD simulation results, so the size reduction of nanoparticles through nanotip indentation successfully reduced the size of nanoparticles without changing the physical properties. The absolute transmittance intensity of the nanoparticle array fabricated by nanotip indentation lithography was smaller because the particle area was smaller than that of nanoimprint lithography. However, it was confirmed that optical

hydrogen measurement was possible with an intensity sufficient to observe the change in transmittance when the phase transition from PdAu to PdAuH_x was performed.

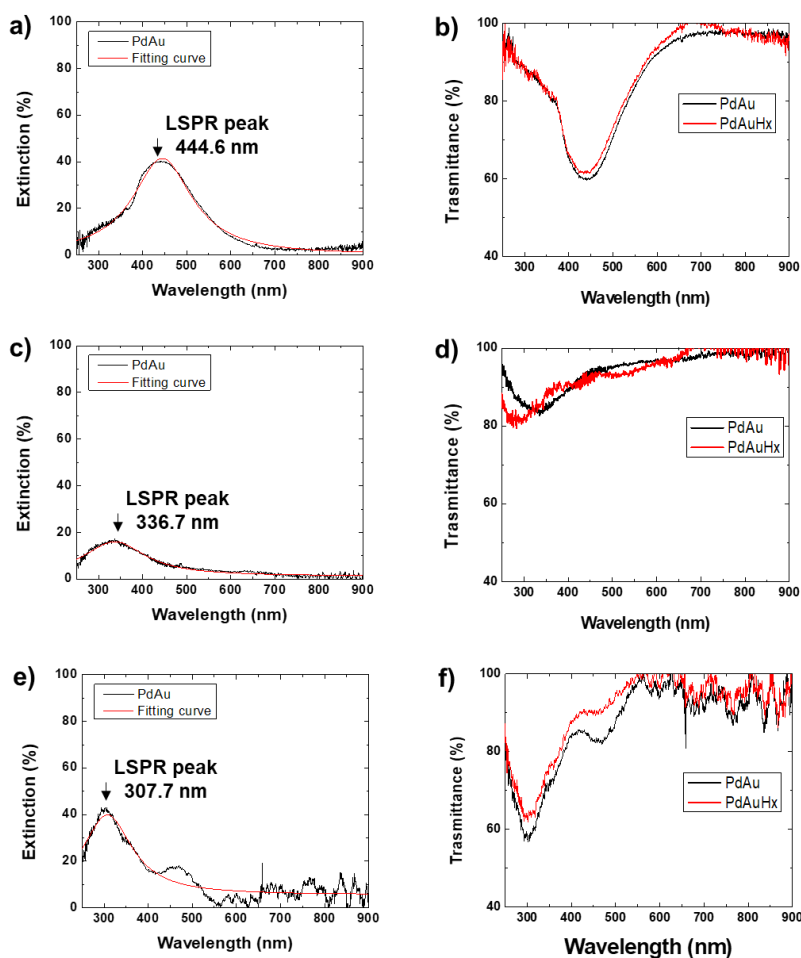
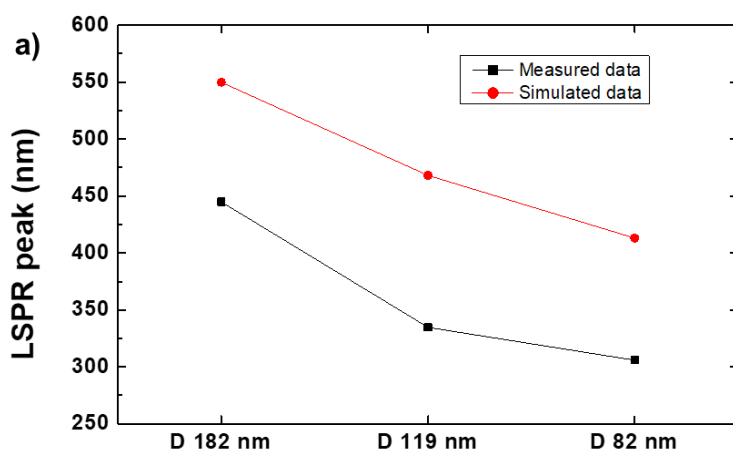


Figure 4.10 Measured extinction and transmission spectra of PdAu nanoparticle arrays fabricated by nanotip indentation lithography, a) extinction and b) transmittance of the nanoparticle array with a diameter of 182 nm and a pitch of 300 nm, c) extinction and d) transmittance of the nanoparticle array with a diameter of 118.2 nm and a pitch of 300 nm. e) extinction and f) transmittance of the nanoparticle array with a diameter of 82.2 nm and a pitch of 150 nm.



b)

| Diameter (nm) | Pitch (nm) | LSPR peak (nm) | LSPR peak (nm) The result of simulation of the material with Pd |
|---------------|------------|----------------|--|
| 182 | 300 | 444.7 | 549.7 |
| 118.8 | 300 | 334.7 | 468.0 |
| 82.2 | 150 | 305.7 | 413.0 |

Figure 4.11 a) LSPR peak change according to the change in the diameter of nanoparticles, b) Summary of diameter, pitch, measured LSPR peak and simulated LSPR peak

4.3.5. The evaluation of optical hydrogen sensing properties for various condition of PdAu nanoparticle array

Figure 4.12 shows the results of evaluating the hydrogen sensing properties according to the annealing temperature of Pd₇Au₃ fabricated using nanoimprint lithography. By analyzing this result, it was possible to obtain response data according to the hydrogen partial pressure of the samples annealed at various temperatures. The results were shown in Figure 4.13. In general, it is an α -phase dominant region at low hydrogen pressure and β -phase dominant region at high hydrogen pressure [17,18]. Between these two regions, an $\alpha+\beta$ phase region may exist depending on the conditions [19]. However, in the case of the $\alpha+\beta$ phase region, the phase transition cannot be predicted, so there is a disadvantage that the reliability of the sensor is lowered in this characteristic section [20].

In the samples at annealing temperatures of 400 °C, 500 °C, and 600 °C, it can be clearly seen that the response characteristics according to the hydrogen partial pressure are divided into an α -phase dominant region and a β -phase dominant region. The result that the hysteresis seen in Pd disappears in this Pd₇Au₃ composition can also be found in other papers [21,22]. On the other hand, the $\alpha+\beta$ phase region was also observed in the sample annealed at 700°C. The reason why the $\alpha+\beta$ phase region was rediscovered at 700°C is that the crystallographic properties of Pd₇Au₃ nanoparticles were changed due to high-temperature heat treatment. The increase in the percentage of Au

on the surface locally lowered the Pd content in the nanoparticles, and the $\alpha+\beta$ phase region was regenerated by the locally changed PdAu content.

Comparing the magnitude of response according to the annealing temperature, the responses of 100% hydrogen concentration were 7.01%, 1.38%, 1.32% and 5.96% at annealing temperatures of 400°C, 500°C, 600°C and 700°C. The 400°C and 700°C samples showed a large response, while the 500°C and 600°C samples were relatively small. The sensitivity of the sample annealed at 400°C was 0.53 %/torr in the α -phase region and 5.15 %/torr in the β -phase region. The sensitivity of the sample annealed at 500°C was 0.42 %/torr in the α -phase region and 0.14 %/torr in the β -phase region. The sensitivity of the sample annealed at 600°C was 0.35 %/torr in the α -phase region and 0.14 %/torr in the β -phase region. The smaller the response magnitude, the smaller the difference in sensitivity between the α -phase region and the β -phase region.

Figure 4.14 shows the analysis results of response time and recovery time according to hydrogen pressure. The results of comparing the response time and recovery time at a hydrogen concentration of 4% are as follows. The sample annealed at 400°C was measured to have a response time of 114.6 sec and a recovery time of 156.6 sec. The sample annealed at 500°C was measured to have a response time of 56.2 sec and a recovery time of 87.0 sec. The sample annealed at 600°C was measured to have a response time of 31.9 sec and a recovery time of 54.0 sec. The sample annealed at 700°C was measured to have a response time of 286.6 sec and a recovery time of 141.0

sec. It was observed that response time and recovery time showed good characteristics in the order of the samples annealed at 600°C, 500°C, 400°C and 700°C.

As a result of analyzing the hydrogen measurement properties according to the annealing temperature, it was confirmed that annealing at 600°C showed the best characteristics. The reason why the annealing temperature of 600°C was able to show the best characteristics is as follows. The highest temperature was the annealing temperature, preventing Au from going to the surface under the influence of 4% hydrogen. Also, the crystallinity index on the XRD was the best. This is because the temperature of 600°C provided enough energy to move the atoms on the surface, so that the atoms could be arranged in a long-range order, and the residual stress was lowered.

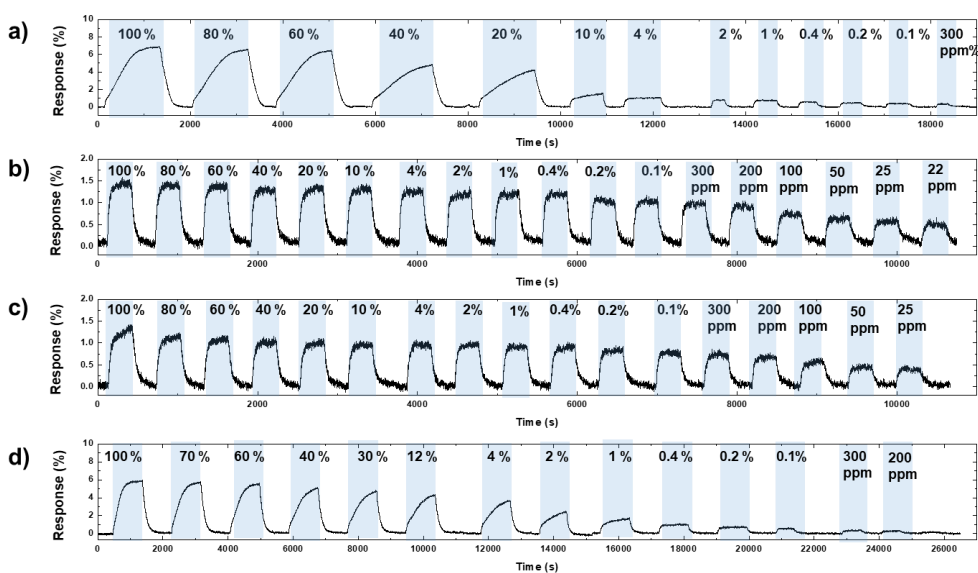


Figure 4.12 Optical hydrogen measurement results according to various hydrogen contents, a) Nanoimprinted Pd₇Au₃ nanoparticle array annealed at 400 °C, b) Nanoimprinted Pd₇Au₃ nanoparticle array annealed at 500 °C, c) Nanoimprinted Pd₇Au₃ nanoparticle array annealed at 600 °C, d) Nanoimprinted Pd₇Au₃ nanoparticle array annealed at 700 °C.

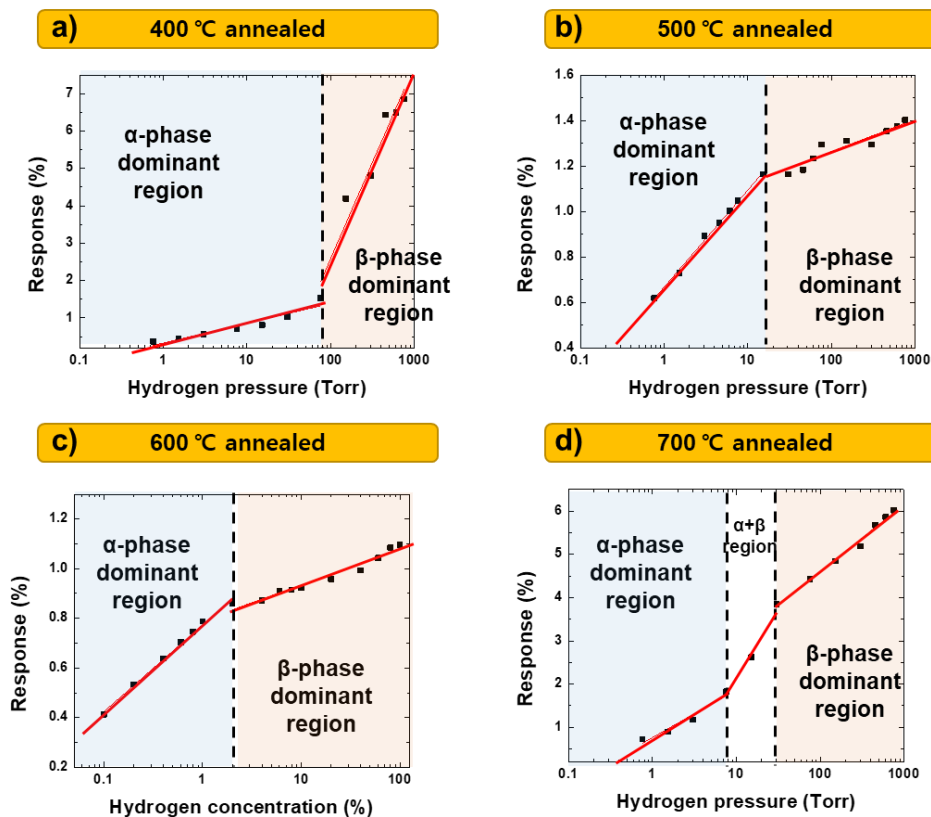


Figure 4.13 Analysis result of response change according to hydrogen partial pressure, a) Nanoimprinted Pd7Au3 nanoparticle array annealed at 400 °C, b) Nanoimprinted Pd7Au3 nanoparticle array annealed at 500 °C, c) Nanoimprinted Pd7Au3 nanoparticle array annealed at 600 °C, d) Nanoimprinted Pd7Au3 nanoparticle array annealed at 700 °C.

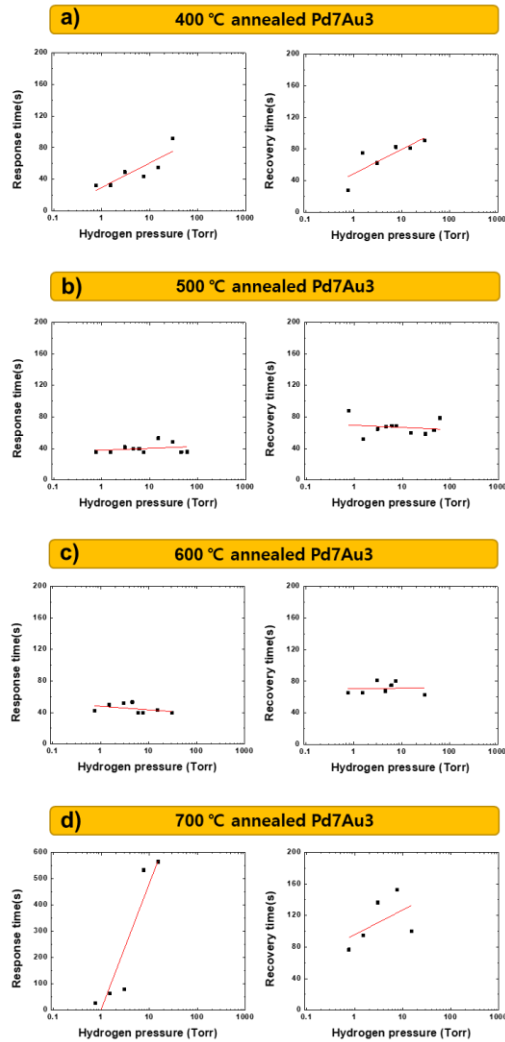


Figure 4.14 Analysis result of response time and recovery time according to hydrogen pressure, a) Nanoimprinted Pd7Au3 nanoparticle array annealed at 400 °C, b) Nanoimprinted Pd7Au3 nanoparticle array annealed at 500 °C, c) Nanoimprinted Pd7Au3 nanoparticle array annealed at 600 °C, d) Nanoimprinted Pd7Au3 nanoparticle array annealed at 700 °C.

Next, hydrogen measurement properties for various PdAu compositions were investigated. Figure 4.15 shows the results of evaluating the hydrogen sensing properties according to various composition of PdAu nanoparticle array fabricated by nanoimprint lithography. The PdAu nanoparticle array used for the measurements was annealed at 600°C. From the data in Figure 4.15, the analysis result of the response change according to the hydrogen partial pressure was shown in Figure 4.16. The $\alpha+\beta$ region appears in the PdAu alloy until the Au content is 10%. Two regions, α -region and β -phase were observed when the Au content in the PdAu alloy was more than 20%. As the Au content increased, it was observed that the difference in sensitivity between the two regions decreased. However, it was observed that the difference increased again in the sample with Au content of more than 40%. In addition, when the Au content in the PdAu alloy was 50% or more, it became difficult to measure hydrogen. As a result of evaluating the sensing characteristics for various hydrogen concentrations, it was determined that the Pd7Au3 composition was most suitable.

As a result of analyzing the response time and recovery time according to the composition, it was found that the response time and recovery time of the Pd nanoparticle array and the Pd7Au3 nanoparticle array were the fastest. Figure 4.17 shows the results of analyzing the response time and recovery time for Pd and Pd7Au3 nanoparticle arrays. The response time of the Pd composition was faster than that of the Pd7Au3 composition, whereas the

recovery time of the Pd₇Au₃ composition was faster than that of Pd composition.

The LoD measurement results of the Pd₇Au₃ composition was shown in Figure 4.18. It was possible to measure up to 144 ppb, and no reaction was observed at hydrogen concentrations lower than that. Because LoD measurement was performed in vacuum, it shows better properties than nitrogen atmosphere. Even with that in mind, 144 ppb was a very good LoD property. It was confirmed that the Pd nanoparticle array can also measure up to 144 ppb. The reason for showing such good LoD characteristics seems to be because the nanoparticles are arranged in a hexagonal structure. Through FDTD simulation, when nanoparticles are ordered in a hexagonal pattern, it is confirmed that a larger response value is shown at the same hydrogen pressure than a random structure, and as a result, good LoD characteristics are shown.

To find a composition more suitable for hydrogen measurement among the Pd nanoparticle array and the Pd₇Au₃ nanoparticle array, various comparisons were conducted. Figure 4.19 shows the comparative analysis results of the hydrogen measurement properties for the Pd nanoparticle array and the Pd₇Au₃ nanoparticle array. First, the magnitude of response at 100% hydrogen concentration was 0.79% for Pd nanoparticles and 1.32% for Pd₇Au₃ nanoparticles. The sensitivities of the α -phase and β -phase regions were 0.242 %/torr and 0.416 %/torr for the Pd composition, and 0.350 %/torr and 0.142 %/torr for the Pd₇Au₃ composition. The Pd composition and the

Pd7Au3 composition showed different characteristics in the β -phase region. The Pd composition increased the sensitivity in the β -phase, but the Pd7Au3 composition decreased the sensitivity. However, considering the difference in sensitivity, the Pd7Au3 composition is more advantageous because the difference in sensitivity is smaller in the Pd7Au3 composition. In addition, although the $\alpha+\beta$ region disappeared from the Pd7Au3 composition, the $\alpha+\beta$ region still exists in Pd, indicating that the Pd7Au3 composition is more advantageous in terms of measurement range. At the hydrogen partial pressure of 4%, the response time and recovery time of the Pd composition were 29.5 sec and 64.1 sec, and the Pd7Au3 composition was 31.9 sec and 54.0 sec. The response time of the Pd7Au3 composition was 8% slower than that of the Pd composition, but the response time was 18% faster than that of the Pd composition. Also, LoD was measured to be 144 ppb for both compositions. Overall, the composition of Pd7Au3 does not exist in the $\alpha+\beta$ region, and it can be judged that it is more suitable for a hydrogen sensor by showing higher response, appropriate sensitivity, and decent response time.

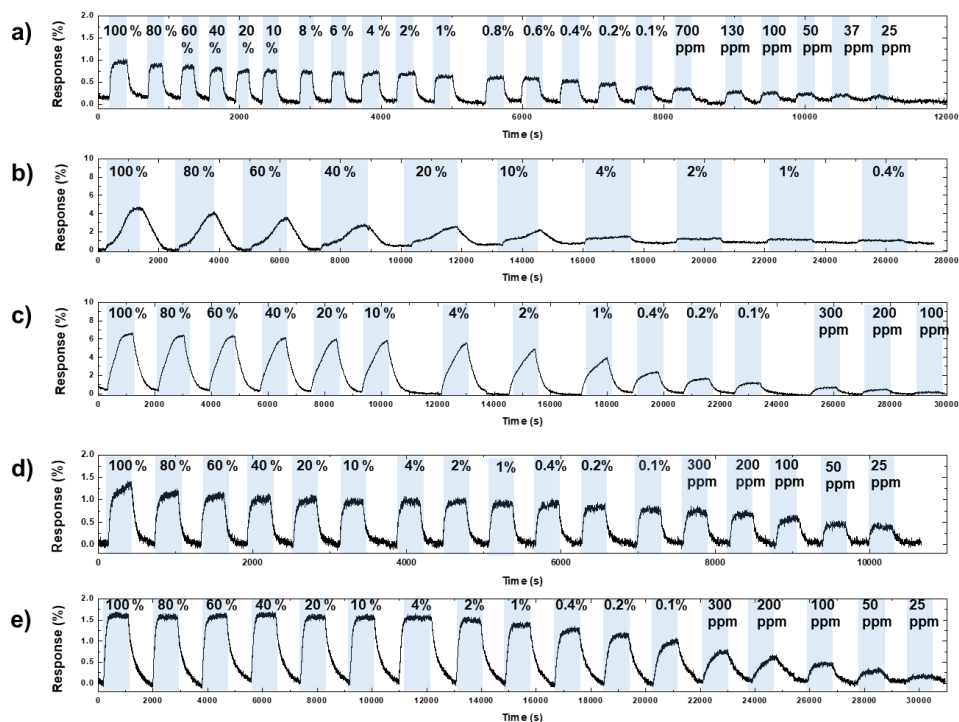


Figure 4.15 Optical hydrogen measurement results according to various hydrogen contents, a) Nanoimprinted Pd nanoparticle array, b) Nanoimprinted Pd₉Au₁ nanoparticle array, c) Nanoimprinted Pd₈Au₂ nanoparticle array, d) Nanoimprinted Pd₇Au₃ nanoparticle array, e) Nanoimprinted Pd₆Au₄ nanoparticle array

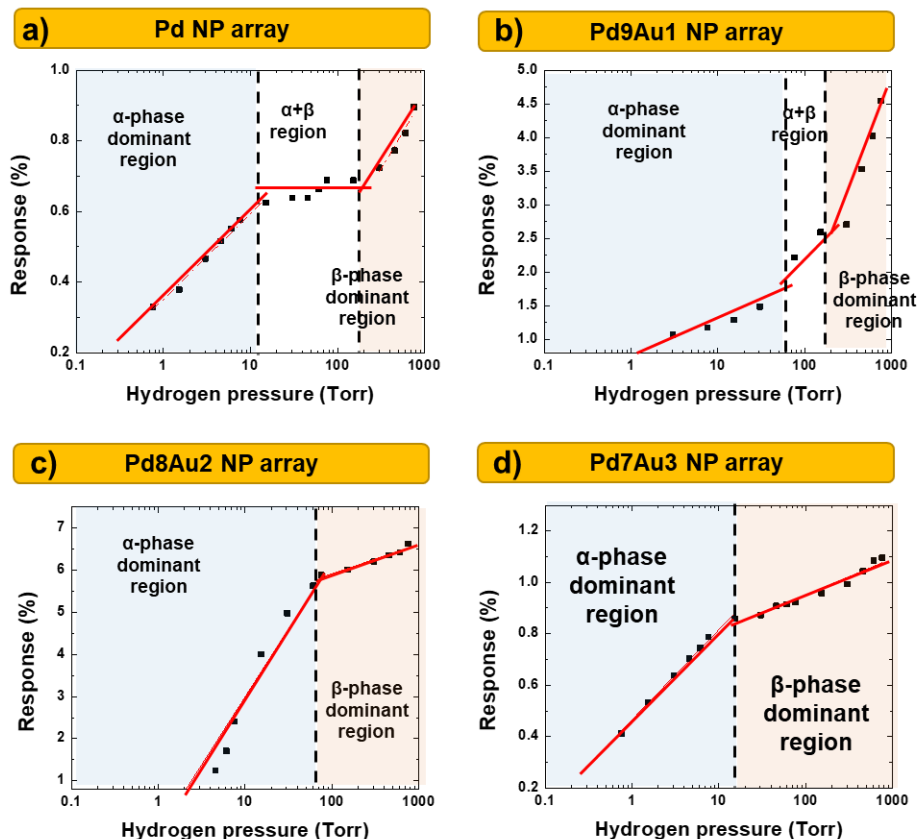


Figure 4.16 Analysis result of response change according to hydrogen partial pressure, a) Nanoimprinted Pd nanoparticle array, b) Nanoimprinted Pd9Au1 nanoparticle array, c) Nanoimprinted Pd8Au2 nanoparticle array, d) Nanoimprinted Pd7Au3 nanoparticle array

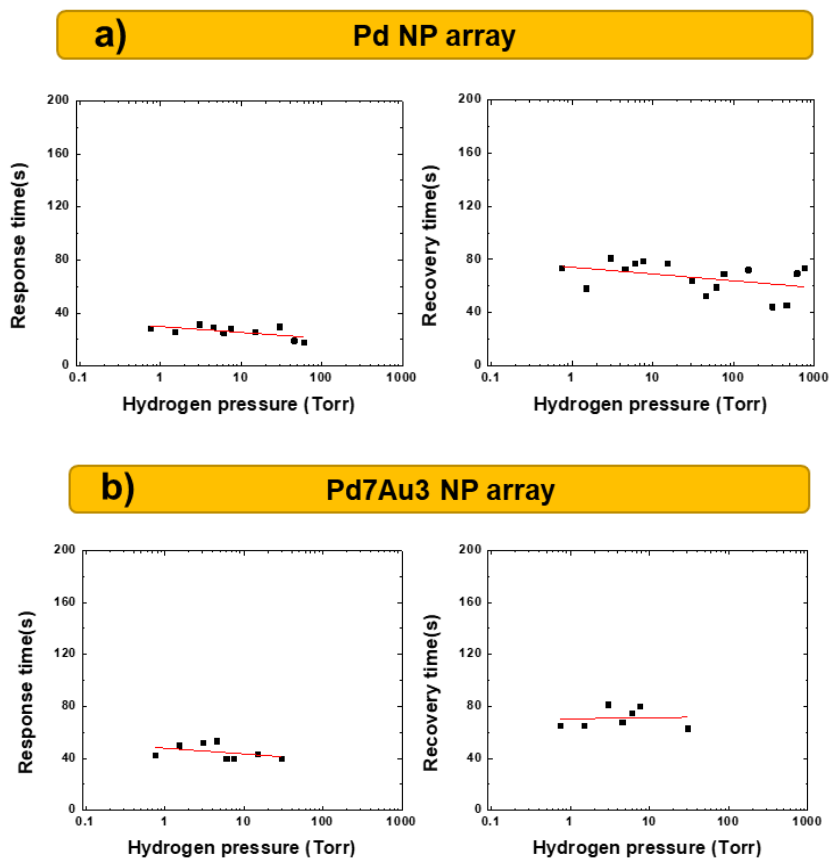


Figure 4.17 Analysis result of response time and recovery time according to hydrogen pressure, a) Nanoimprinted Pd nanoparticle array and b) Nanoimprinted Pd7Au3 nanoparticle array

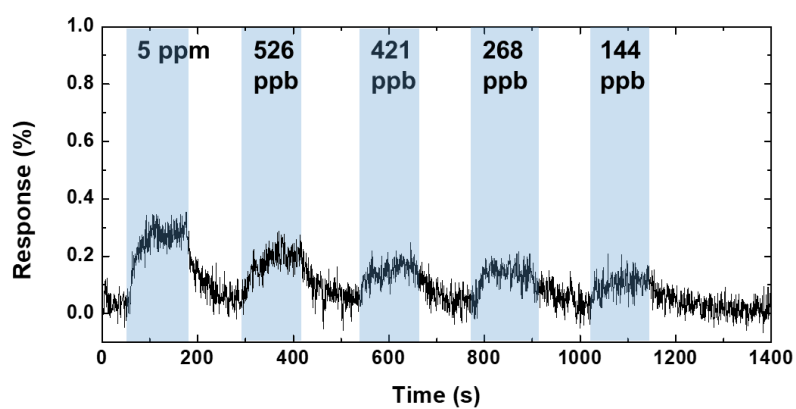


Figure 4.18 LoD measurement results for Pd₇Au₃ Nanoparticle Arrays

Table 4.1 Comparison of hydrogen sensing properties for Pd nanoparticle array and Pd₇Au₃ nanoparticle array

| classification | Response (%) @ 760 torr | Sensitivity (%/Torr) | | Presense of $\alpha + \beta$ region | 4% H ₂ | | LoD (ppb) |
|---------------------------------|----------------------------|-----------------------------|----------------------------|--|----------------------|----------------------|--------------|
| | | α -phase dominant | β -phase dominant | | response time (s) | recovery time (s) | |
| Pd | 0.79 | 0.242 | 0.416 | O | 29.5 | 64.1 | 114 |
| Pd ₇ Au ₃ | 1.32 | 0.350 | 0.142 | X | 31.9 | 54.0 | 114 |

4.4. Summary

In this chapter, the optical properties and hydrogen measurement properties of PdAu nanoparticle arrays fabricated by nanoimprint lithography and nanoindentation lithography were discussed. The composition of PdAu fabricated by nanoimprint lithography and changes in optical properties according to annealing temperature were investigated. It was observed that the LSPR peak changes depending on the crystallinity and surface composition. Nanoparticles of various diameters fabricated by nanotip indentation have no difference in tendency when compared with the FDTD data. Therefore, although nanoparticles of different diameters were made, it was confirmed that there was no difference in optical properties, and that there was only a difference according to the change in diameter. As a result of evaluating the hydrogen measurement performance of the prepared PdAu nanoparticle array, the Pd₇Au₃ composition was the best. The reason why the Pd₇Au₃ composition showed excellent hydrogen measurement characteristics is that it received the effect of high-temperature heat treatment most effectively because it was the highest heat treatment temperature that could prevent Au from going to the surface in a 4% hydrogen atmosphere.

4.5 Bibliography

- [1] W.S.M. Werner, K. Glantschnig and C. Ambrosch-Draxl, "Optical constants and inelastic electron-scattering data for 17 elemental metals." *Journal of Physical and Chemical Reference Data*, 38.4, (2009), 1013-1092.
- [2] K.J. Palm, J.B. Murray, T.C. Narayan and J.N. Munday, "Dynamic optical properties of metal hydrides." *Acs Photonics*, 5.11, (2018), 4677-4686.
- [3] H.B. Jeon, P.V. Tsalu and J.W. Ha, "Shape effect on the refractive index sensitivity at localized surface plasmon resonance inflection points of single gold nanocubes with vertices." *Scientific reports*, 9.1, (2019), 1-8.
- [4] C. Wadell, F.A.A. Nugroho, E. Lidstrom, B. Iandolo, J.B. Wagner and C. Langhammer, "Hysteresis-free nanoplasmonic Pd–Au alloy hydrogen sensors." *Nano letters*, 15.5, (2015), 3563-3570.
- [5] S. Raza, N. Stenger, S. Kadkhodazadeh, S.V. Fischer, N. Kotesha, A.P. Jauho and N.A. Mortensen, "Blueshift of the surface plasmon resonance in silver nanoparticles studied with EELS." *Nanophotonics*, 2.2, (2013), 131-138.
- [6] B. Ajitha, Y.A.K. Reddy and P.S. Reddy, "Green synthesis and characterization of silver nanoparticles using Lantana camara leaf extract." *Materials science and engineering: C*, 49, (2015), 373-381.
- [7] M.R. Bindhu and M. Umadevi, "Antibacterial and catalytic activities of green synthesized silver nanoparticles." *Spectrochimica acta part A*:

- molecular and biomolecular spectroscopy, 135, (2015), 373-378.
- [8] C. Langhammer, Z. Yuan, I. Zorić and B. Kasemo, "Plasmonic properties of supported Pt and Pd nanostructures." *Nano letters*, 6.4, (2006), 833-838.
 - [9] Gl. Barbillon, F. Hamouda, S. Held, P. Gogol and B. Bartenlian, "Gold nanoparticles by soft UV nanoimprint lithography coupled to a lift-off process for plasmonic sensing of antibodies." *Microelectronic Engineering*, 87.5-8, (2010), 1001-1004.
 - [10] Y. Cheng, H. Zhang, X.S. Mao and R. Gong, "Dual-band plasmonic perfect absorber based on all-metal nanostructure for refractive index sensing application." *Materials Letters*, 219, (2018), 123-126.
 - [11] X. Qi and J. Bi, "Plasmonic sensors relying on nanoparticle arrays created by a template-directed dewetting process." *Optics Communications*, 453, (2019), 124328.
 - [12] A. Bansal, J.S. Sekhon and S.S. Verma, "Scattering efficiency and LSPR tunability of bimetallic Ag, Au, and Cu nanoparticles." *Plasmonics*, 9.1, (2014), 143-150.
 - [13] K. Jia, J.L. Bijeon, P.M. Adam and R.E. Ionescu, "Large scale fabrication of gold nano-structured substrates via high temperature annealing and their direct use for the LSPR detection of atrazine." *Plasmonics*, 8.1, (2013), 143-151.
 - [14] O.M. Løvvik, "Surface segregation in palladium based alloys from density-functional calculations." *Surface Science*, 583.1, (2005), 100-106.
 - [15] M. Zhao, W.G. Sloof and A.J. Böttger, "Modelling of surface

- segregation for palladium alloys in vacuum and gas environments." *International Journal of Hydrogen Energy*, 43.4, (2018), 2212-2223.
- [16] P. Ekborg-Tanner and P. Erhart, "Hydrogen-Driven Surface Segregation in Pd Alloys from Atomic-Scale Simulations." *The Journal of Physical Chemistry C* 125.31 (2021): 17248-17260.
- [17] F. D. Manchester, A. San-Martin and J. M. Pitre, "The H-Pd (hydrogen-palladium) system." *Journal of phase equilibria*, 15.1, (1994), 62-83.
- [18] F.A. Lewis, "The palladium-hydrogen system: Structures near phase transition and critical points." *International journal of hydrogen energy*, 20.7, (1995), 587-592.
- [19] N.A. Scholtus and W.K. Hall, "Hysteresis in the Palladium—Hydrogen System." *The Journal of Chemical Physics*, 39.4, (1963), 868-870.
- [20] S. Dekura, H. Kobayashi, K. Kusada and H. Kitagawa, "Hydrogen in Palladium and Storage Properties of Related Nanomaterials: Size, Shape, Alloying, and Metal-Organic Framework Coating Effects." *ChemPhysChem*, 20.10, (2019), 1158-1176..
- [21] F.A.A. Nugroho, R. Eklund, S. Nilsson and C. Langhammer, "A fiber-optic nanoplasmonic hydrogen sensor via pattern-transfer of nanofabricated PdAu alloy nanostructures." *Nanoscale*, 10.44, (2018), 20533-20539.
- [22] F.A. Nugroho, I. Darmadi, L. Cusinato, A. Susarrey-Arce, H. Schreuders, L.J. Bannenberg and C. Langhammer, "Metal–polymer hybrid nanomaterials for plasmonic ultrafast hydrogen detection." *Nature materials* 18.5, (2019), 489-495.

Chapter 5. Conclusion

In this study, the method of making plasmonic nanoparticle arrays was diversified and a method of efficiently controlling the diameter of the nanoparticle array was proposed. In addition, the hydrogen measurement performance of the prepared palladium gold nanoparticle arrays were investigated, and the mechanism was analyzed.

First, we demonstrated the fabrication of nanoparticles using high-throughput and high-resolution nanoimprint lithography to replace nanosphere lithography, which has low reproducibility and is very difficult to pattern. By optimizing the nanoimprint process, nanoparticles with a diameter of 160 nm and a pitch of 200 nm could be efficiently fabricated. Using nanoimprint lithography, which is easy to repeat manufacturing, the properties according to the composition and annealing temperature of the PdAu alloy were analyzed. The crystallographic properties according to the composition were summarized through XRD analysis, and the properties according to the annealing temperature were quantified through XRD and XPS.

Second, nanotip indentation lithography was proposed as a method for effectively and precisely fabricating nanoparticle arrays. Factors that directly or indirectly affect the nanoparticle diameter were investigated for efficient and sophisticated nanoparticle fabrication, and the change in

diameter according to the factors was confirmed. Through this study, we showed that nanoparticles with a diameter of 58 nm to 138 nm can be effectively fabricated using nanotip indentation lithography. In addition, it was demonstrated that 147,700 particles of 82 nm in diameter were fabricated in the 54 μm x 54 μm m area and can be used as a hydrogen sensor.

Finally, the optical properties and hydrogen measurement performance of the fabricated palladium gold nanoparticle array were evaluated. Through FDTD simulation, it was possible to effectively predict the change in the LSPR peak of nanoparticles. Through the difference between the simulation result and the actual measured value, it was confirmed whether the change in the LSPR peak was due to the particle diameter or whether the optical properties were changed. The change of the LSPR peak was traced according to the composition of the PdAu alloy, and the cause of the change of the LSPR peak according to the annealing temperature in the same composition was investigated. In addition, as a result of investigating the hydrogen measurement performance according to the composition of the PdAu alloy and the annealing temperature, it was confirmed that the Pd₇Au₃ composition and the annealing temperature of 600 °C were the optimal conditions.

국문 초록

기후 변화라는 전지구적 위기에 맞서 탄소 중립의 필요성이 증가하고 있다. 수소는 탄소중립을 실현하기 위한 자원으로 각광받고 있다. 또한 수소의 높은 에너지 밀도는 에너지 자원으로써 가치가 높다. 그러나 수소는 넓은 가연범위와 낮은 점화에너지 그리고 빠른 화염속도를 가지고 있기 때문에, 수소 누출은 대규모 폭발로 이어질 수 있다. 수소의 상용화를 위해 수소 누출을 빠르게 감지할 센서가 반드시 갖추어져야 한다.

팔라듐은 수소에 대한 높은 감도와 선택도로 인해 가장 각광받는 수소 감지 재료이다. 그러나 팔라듐은 히스테리 시스로 인해 수소 측정 영역이 제한있고, 팔라듐 내의 수소함량이 높아지면 취화 효과로 인해 기계적 안정성이 떨어지는 단점이 있다. 이러한 단점을 해결하기 위해 다양한 연구가 진행되고 있으며, 다른 금속과의 합금화도 그 중 하나이다.

수소측정 방법 중 대표적인 두가지 방법은 전기적 측정 방법과 광학적 측정 방법이다. 전기적 측정 방법은 일반적인 측정 방법으로 센서 제작이 쉽다는 장점이 있지만, 전자파 간섭(EMI)에 의한 영향과 스파크에 의한 잠재적 폭발 가능성이라는 단점이 가지고 있다. 반면 광학적 측정 방법은 전자파에 영향을 받지 않고 측정 방식에 폭발 가능성이 없으며, 매우 작은 활성 물질 영역에서도 센서로 작동할 수 있기 때문에 작게 센서를 만들 수 있다는 장점이 있다.

이러한 광학적 수소센서 중에서도 국소화 된 표면 플라즈몬 공명을 이용한 수소 센서는 높은 민감도와 빠른 응답속도로 각광받는 고성능 수소 센서이다. 이러한 국소화된 표면 플라즈몬 공명을 이용하기 위해서는 나노 입자의 배열을 제작해야 하는데, 나노 입자의 배열을 제작하는 방법으로는 전자빔 리소그래피와 나노구 리소그래피가 있다. 전자빔 리소그래피는 높은 공정 난이도와 비싼 공정 비용 때문에 쉽게 적용하기 힘든 제작 방법이다. 반면, 나노구 리소그래피는 낮은 공정 비용과 손쉬운 제작으로 가장 많이 사용되었지만, 재연성이 떨어지고 구조화된 나노 입자의 배열을 만드는데 한계가 있었다.

본 연구에서는 국소화된 표면 플라즈몬 공명 기반의 수소 측정용 나노 입자의 배열을 효율적으로 제작하는 방법과 제작된 나노 입자 배열의 광학적 특성 및 수소 측정 특성에 대해 연구하였다. 먼저 나노임프린트 리소그래피를 이용한 육각형 구조의 나노입자를 제작하는 방법을 시연하였다. 최적화된 공정을 통해 200 nm 피치의 육각형 구조를 갖는 160 nm 직경의 나노 입자 배열을 효과적으로 제작하는 것을 보였었으며, 나노임프린트 리소그래피를 이용하여 국소화된 표면 플라즈몬 공명 기반의 수소 센서에 적합한 팔라듐-골드 조성을 파악하기 위해 다양한 조성의 팔라듐-골드 나노 입자 배열을 제작하고 이의 결정학적 특성과 표면 조성 등을 분석하였다. 열처리에 의한 합금화 과정에서 열처리 온도에 의해 팔라듐-골드 나노 입자의 표면 조성이 달라지는 것을 관찰하였고, 600 °C 에서 열처리하였하는 것이 최적의 열처리 조건임을 확인하였다.

그러나 나노임프린트 리소그래피는 나노 입자의 직경 혹은 패턴을 바꾸기 위해서는 나노임프린트 몰드를 바꾸야 한다는 단점 있었고, 이러한 단점을 극복하고자 나노팁 인텐테이션 리소그래피를 통한 나노 입자 배열 제작을 제안하였다. 나노팁 인텐테이션 리소그래피를 통한 나노 입자 제작은 이전까지는 SERS 용 나노 입자 제작 등 매우 제한적으로 사용되어져 왔지만, 본 연구를 통해서 가로 60 μm , 세로 60 μm 의 대면적 영역에 나노 입자 배열을 형성할 수 있다는 것을 보였기 때문에 그 쓰임새가 다양화될 것으로 기대된다. 본 연구에서는 나노팁 인텐테이션 리소그래피 공정에서 나노 입자 직경에 영향을 주는 3 가지 요소들에 대해 자세히 조사하였고, 이를 통해 수 나노미터 간격으로 입자를 조절하여 나노 입자의 직경을 56 nm 에서 132 nm 까지 효율적으로 조절하는 것을 보였다. 또한 입자의 크기 별로 최적화된 공정 조건을 논문에 수록하였다.

마지막으로 나노임프린트 리소그래피와 나노팁 인텐테이션 리소그래피를 통해 제작된 팔라듐-골드 나노 입자 배열의 광학적 특성과 수소 측정 성능에 관해 조사하였으며, 다양한 조건의 팔라듐-골드 나노 입자 배열의 국소화된 표면 플라즈몬 공명 피크의 이동을 측정하였고, 그 원인에 대해 서술하였다. 또한 열처리 온도에 따라 국소화된 표면 플라즈몬 공명 피크가 변화하는 이전에 보고된 피크의 이동보다 큰 이동이 관찰되었고, 이러한 이동에 이유에 대해 서술하였다. 다양한 팔라듐-골드 조성의 수소 측정 특성을 분석하였으며, Pd7Au3 조성이 가장 적합한 조성임을

확인하였고, 600 °C 에서 합금화 하였을 때 수소 측정 특성이 향상되는 원인에 대해서 분석하여 서술하였다.

본 연구를 통해, 나노팁 인텐테이션 리소그래피를 이용한 나노입자 제작 방법이 다양한 분야에 사용되어지기를 기대하며, 나노입자의 표면 조성 제어를 통해 수소 센서의 성능을 향상시키는 기술이 발전해 현재의 수소 센서보다 더 나은 수소 센서가 개발되기를 기대한다.

주요어:

나노임프린트 리소그래피, 나노팁 인텐테이션 리소그래피, 국소화된 표면 플라즈몬 공명 기반의 수소 센서, 표면 분리 효과, 팔라듐-골드 합금

학번: 2014-21490
